universität wien

MASTERARBEIT

Titel der Masterarbeit

Molecular Line Spectroscopy and Extinction Mapping in the Pipe Nebula Molecular Cloud

Verfasser

Elisabeth Künzl Bakk. rer. nat.

angestrebter akademischer Grad

Master of Science (MSc)

Wien, 2014

Studienkennzahl lt. Studienblatt:	A 066 861
Studienrichtung lt. Studienblatt:	Astronomie
Betreuer:	Dr. Jan Forbrich

Contents

1 Introduction

1.1 Preface

Molecular clouds (MCs) are the nurseries of stars. Inside them a clumpy structure becomes visible consisting of several cores where the molecular material is concentrated to higher column densities. In such cores stars are born which will afterwards disperse their surrounding parent cloud and become visible in the optical. Despite the high optical opacity molecular cloud structure can be revealed by infrared dust extinction measurements and molecular line transitions in the radio range. The observed parameters enable us to derive gas masses, kinematics and molecular composition of the cloud cores and give insight in the conditions prevailing stellar birth. The main aim of this master thesis was to investigate such conditions by studying a nearby dark molecular cloud which is known for its extremely low star formation activity. Therefore the Pipe Nebula is an ideal test laboratory for studying chemical and kinematical conditions before star formation has set in. The first chapter gives an overview about the properties of interstellar matter (*ISM*) and molecular clouds. The process of star formation will be described in short ending with a summary of our present day knowledge of the Pipe nebula following the actual literature. In chapter two basic observational facts are given which consider both physical and theoretical aspects of molecular line observations. Chapter three gives an overview about the spectral data sample including observation and reduction methods as well as a presentation of all measured molecular species. In chapter four the analyzing process is described in detail leading over to a presentation of the obtained results in chapter five. A final summary is given in chapter 6. Complete sets of the molecular emission and extinction maps can be found in the appendix.

1.2 Interstellar Matter

The galaxy is composed of stars and the interstellar matter (ISM) between them. These two components stand in close relationship to each other as stars were born out of dense conglomerations of ISM and will return a certain amount of their material to the ISM. The latter happens through stellar winds and in later evolutionary stages when stars blast away their outer shells. While we can observe stars with optical telescopes the ISM reveals itself in the radio and near infrared range in emission and absorption spectra. However, young stars which are still embedded in their dark parent molecular cloud can only be observed at infrared and sub-mm wavelengths.

After current models interstellar matter consists to 99 % of gas particles and to 1 percent of carbon-silicate dust grains with diameters ranging between 0.1μm and 1μm.

The most abundant element in the gas component is atomic hydrogen H, followed by Helium, Oxygen, Carbon, Nitrogen, ...

The gas phase ISM can now be destinguished into three main phases differing by their temperature and density parameters. All three of them are strongly correlated (Ostricker et. al, 2009):

1. The hot component of the ISM fills much of the volume in interstellar space. Hot coronal gas is ejected by supernovae remnants (SNR's) and evaporates all ambient clouds as well as warm gas. As the supernova expands the outer shock wave will sweep up all interstellar material which forms an outer shell around the evolving low density region.

   Warm ionized gas is heated by young O or B stars which ionize their ambience by high UV radiation. The surrounding medium reaches temperatures up to 8000 K and densities of $10^{-4}\mathrm{cm}^{-3}$. Such regions are also called H II regions according to the hydrogen existing only in its ionized form.

2. The neutral gas component is found in interstellar cloud associations. The *warm neutral component* is associated with diffuse cloud material which is exposed to the interstellar radiation field (*ISRF*), while the *cold neutral component* is found in higher density regions at greater optical depths. Densities and typical temperature values range between $10^2 - 10^3\mathrm{cm}^{-3}$ and 20 to 50 K.

3. The cold molecular gas makes up the third phase of the ISM. This component is bounded into giant molecular clouds (GMCs) and molecular clouds (MCs). GMCs typical extend over 50 - 100 pc and have masses of $10^5 - 10^6\ M_\odot$; molecular clouds are some tens of parsecs in size and show masses of $10^4\ M_\odot$. GMCs are the birth places of high- and low mass stars whereas in MCs essentially low-mass star formation takes place.

Through different heating and cooling processes there exists a consequent exchange between the three different phases. On large scales no thermodynamical equilibrium is possible. Important processes driving the phase transformations are:

1. Heating by stellar UV radiation, X-rays or Cosmic rays

2. Cooling by line emission (neutral gas) and radiative decay (ionized gas)

Together the three phases and their exchange processes build up a cosmic cycle of star formation and stellar death. As an SNR destroys all ambient clouds of diffuse and dense matter it acts as a limiting factor for the denser phases of the ISM. While the SNR

Figure 1.1: A star forming region in the Carina Nebula; The upper panel shows the optical image while the IR image below reveals the interior stars. Credit:NASA

evolves into a cavity a shell of swept up interstellar material is formed around it. After sufficient cooling of the SNR the outer shell will break up into small clouds which then can form molecular cloud assembles again. In this way it happens that the super nova rate of the last generation of stars sets an upper limit on the formation rate of the next generations of stars (Ostricker et. al, 2009).

1.3 Molecular Clouds and the Phases of Star Formation

Molecular clouds are found mostly in the galactic plane where the galactic gravitational potential favours their formation. According to the galaxy's density profile molecular gas accumulates preferably in the spiral arms and the center of the galaxy (Dobbs, Bonnel, Pringle 2006). To start star formation molecular clouds need to undergo a gravitational collapse and to fragment into smaller clumps with cores of higher density. How this actually happens is a topic of actual research. The presence of supersonic motions in dark clouds has been known since the first molecular-line studies revealed non-Gaussian line profiles and velocity differences across the cloud of the order of 1 kms^{-1} or more (Bergin & Tafalla, 2007); the sound speed for gas of 10 K is 0.2 km s^{-1}. One commonly used approach is that super nova shock fronts can induce

turbulence and large scale instabilities which lead to the collapse and fragmentation of a cloud.

The free fall time (t_{ff}) of a molecular cloud describes how long it would take the cloud to collapse under its own gravitational attraction when all possible opposing forces are neglected. If we consider a spherical cloud of mass M and radius R the gravitational potential U of the sphere is given as

$$U = -\frac{3}{5}\frac{GM^2}{R} \tag{1.1}$$

As can be shown by Newtons 2nd Law a test particle at a radius $r = R$ would feel an acceleration toward the center according to $-\frac{GM}{r^2}$. Integrating this over r and setting the boundary conditions to $r = R$ and $t = 0$ an expression of the free fall time can be derived:

$$t_{ff} = \frac{1}{4}\sqrt{\frac{3\pi}{2G\rho}} \tag{1.2}$$

Wilson et al., 2009 describes observational differences between the calculated free fall time of a typical molecular cloud ($t_{ff} = 5 \times 10^7 yr$) and the observed star formation rates. There are ≥ 500 clouds of sufficient mass so the average star formation rate must be $500 \times 10^2 \ M_\odot \ yr^{-1}$. Indeed the real observed star formation rate is only a small fraction of that. Thus there must be some supporting mechanism against gravitational collapse which could either be turbulence or magnetic fields. However, supersonic turbulence has a rapid decay time so the support may be provided by magnetic fields (Wilson et al, 2009).

The concept of **ambipolar diffusion** emphasizes the role of magnetic fields in the cloud fragmentation process (Bergin & Tafalla, 2007). The magnetic field is expected to be firmly linked to the gas and magnetic pressure supports together with thermal pressure against gravity. Therefore the critical mass (M_{crit}) for which the gravitational collapse would happen is expected to become larger. Furthermore in a magnetized cloud M_{crit} stays constant under contraction. In the cloud ions and neutral particles are partly linked together by collisions. Thus as the cloud is contracting gravitational forces draw the neutrals toward the clouds center. Due to collisional binding the ions too are forced toward the center and a gradient in the magnetic field evolves. The electrical field of the cloud (which stands normal to the magnetic field) counteracts the drift of the magnetic field lines such, that while the particles drift toward the center the magnetic field lines drift in the other direction therefore thinning out the magnetic field strength. In a region around the gravitational center the magnetic flux stays constant relative to the ion-plasma. So the critical mass stays constant while the real mass grows slowly due

to the attraction of neutrals. If the thermal pressure is sufficiently low gravitational collapse can now happen. Derived ambipolar diffusion timescales match the observed timescales of star formation much better.

It is believed that by ambipolar diffusion the clouds fragment into gravitationally bound sub-structures, so called cores. The cloud collapse is isothermal which means that with rising density the Jeans Mass (M_J) of the cloud is falling. The Jeans Mass is defined as the maximum mass which can be balanced against gravity and can be most simply approximated by use of the virial theorem. In virial equilibrium two times the kinetic energy (V) equals the potential energy (U) of the system such that

$$2\ V = U \tag{1.3}$$

This can be rewritten with the U as the gravitational potential of the cloud (see equation 1.1) and V as the kinetic (thermal) energy of the atoms (N) which make up the cloud:

$$3NkT = \frac{3}{5}\ \frac{GM^2}{R} \tag{1.4}$$

If $\frac{3}{5}\frac{GM^2}{R}$ grows bigger than $3NkT$ gravity wins and the cloud starts to collapse. By substituting the number of particles by the mass of the cloud divided per particle mass ($N = \frac{M}{m}$) and assuming a constant density ρ the instability criterion can be rewritten as

$$M > (\frac{5kT}{Gm})^{\frac{3}{2}}\ \ (\frac{3}{4\pi\rho})^{\frac{1}{2}} \tag{1.5}$$

Whole molecular clouds typically can not overcome their Jeans Mass instability criterion but after fragmentation smaller pieces of the cloud can start to collapse on their own. These structures are on the scales of 0.1pc and have masses approaching the Jeans instability criterium. If pressure conditions of the ambient medium are appropriate the cores collapse in free fall times of some 100.000 yr. During this process the density increases and therefore also opacity. At certain density values the gas and dust become optically thick so the energy produced by collapse gets completely absorbed. The central region begins to heat up and contraction pauses (Low & Klessen, 2004). When temperatures of $T \approx 2000$ K are reached the H_2 molecule starts to dissociate, absorbing energy. The core begins to contract again where the released gravitational energy goes into the dissociation of H_2. As long as H_2 molecules are present the temperature rises only slowly. When all molecules are dissociated a sharp rise in temperature occurs producing pressure gradients which again halt the collapse. Now a hydrostatic state is reached again with the resulting object called a **protostar** (Low & Klessen, 2004).

1.3.1 Phases of Star Formation & Young Stellar Objects

On observational basics the star formation process can be devided into four phases (Lada et al., 1987). In the *Class 0 phase* the contraction of the core and formation of a protostar happens (see above). The formation further proceeds into

1. *Class I phase*

   The protostar grows in mass by the accretion of infalling gas and dust from the outer parts of the core. Luminosity is mainly produced by accretion. Material of high angular momentum first enters a disk around the star and than gets transported inwards by viscous processes. The disk has a radius of 50 to 1000 AU and gets thinner toward the center. Due to mass accretion the protostar develops a mostly neutral bipolar wind. In this phase the objects are called *Herbig-Haro Objects* referring to the first astronomers investigating these objects, George Herbig and Guilermo Haro. The bipolar outflows shove away the surrounding molecular gas and the star becomes visible. Until this happens the (proto)star is only visible at IR and submm wavelengths. The whole process takes a time of $1 - 4 \times 10^5 yr$. Massive stars with $M \geq 2\ M_\odot$ enter the main sequence already during the accretion phase.

2. *Class II phase*

   In the class II phase of its evolution the star has dispersed the surrounding medium. Only a disk remains around the star contributing to an IR excess in the spectral energy distribution of the system which is dominated by the stellar Planck spectrum at visible wavelengths. In this stage planetesimals and planets form in the disk while the star tends to massive outflows and winds cleaning up the disk of remaining debris. The Class II phase lasts for $1 - 3 \times 10^6\ yr$.

3. *Class III phase*

   These stars are called post-T-Tauri stars or zero age main sequence (ZAMS) stars. They have ignited nuclear fusion and can be found in the HRD slightly above the main sequence ($\Delta \leq 3$mag).

After exploring the basics of star formation the next section will accommodate the molecular cloud investigated in the this study and outline its general characteristics following the actual literature.

1.4 Our Present Day Knowledge of the Pipe Nebula

Since the first published study of the Pipe Nebula by Onishi et al. in 1999 the number of papers regarding this region consequently increased. The Pipe Nebula is a near-by dark molecular cloud, located approximately 130 pc from earth (Lombardi et al., 2006). The main component is a 15 pc long filament (*stem*) centered at $l = 0,\ b = 5$ which merges at approximately $l = 0$ with the *bowl*, an irregularly shaped gas structure at the southern end. To the northwest the Pipe ends into its only star forming region *Barnard 59* $(B59)$. The Pipe Nebula extends northwards into a region of widely dispersed smaller clouds - including the Barnard objects 68, 72, and 74 - called *the smoke* (Muench 2007). From the smoke an extinction bridge spreads to the west seemingly connecting the Pipe with the molecular cloud complex of Rho Ophiuchus. Due to its very low star formation efficiency of 0.06 % (Forbrich et al. 2009) the Pipe Nebula was discovered as ideal laboratory to test conditions preceding stellar birth.

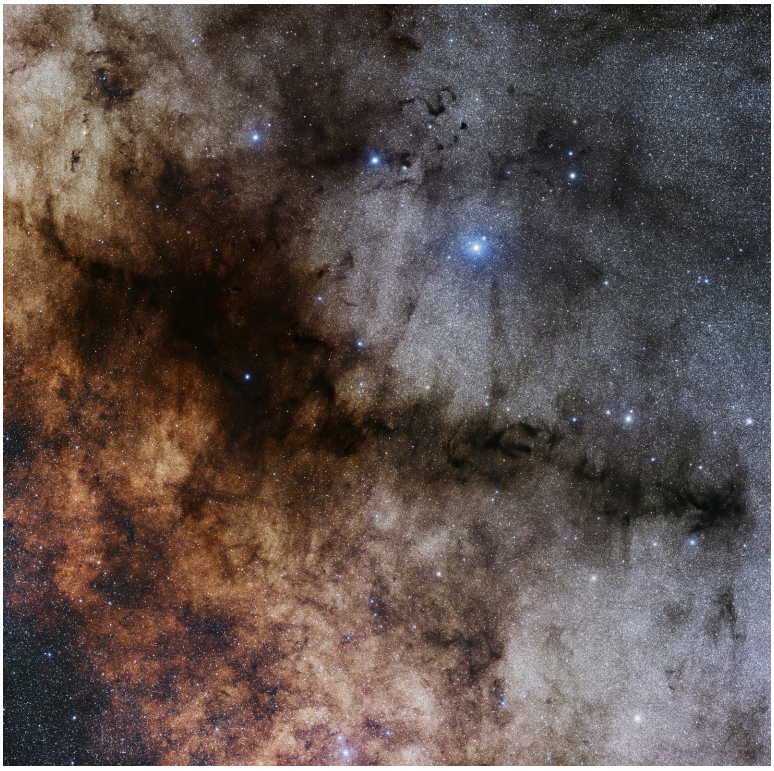

Figure 1.2: Optical image of the Pipe Nebula Molecular Cloud; Credit: from www.cfa.harvard.edu

First observations were single dish observations of molecular line transitions of CO Isotopologues. Onishi et al. identified 14 cores of increased molecular density with masses around 30 $M_{\odot}$. In 2006 Marco Lombardi, Joao Alves and Charlie Lada produced a high resolution extinction map of the Pipe Nebula region using 4.5 million stars of the Two Micron All Sky Survey (2MASS). They identified 159 dense molecular cores inside the Pipe with typical masses of 0.5 to 2 $M_{\odot}$ and densities of around 4 g cm^{-3} (Lombardi et al., 2006).

A study of the kinematic properties by Muench et al. 2007 revealed three different regions throughout the cloud, differing in their kinematical structure. Each region was named alluding to the morphology of a smoking pipe: namely as stem, bowl, and smoke.

Throughout the cloud a range of $v_{LSR} \approx 3 - 7$ km s^{-1} was observed. The corresponding distribution function shows two maxima at 3.48 km s^{-1} and 4.95 km s^{-1}. The primary component centered at $v_{LSR} \approx 3.5$ km s^{-1} consists of a 15 pc long filamentary structure running down the Pipe's stem and twisting around one side of the bowl. So it becomes somewhat redshifted relative to the stem but shifts back to 3.5 km s^{-1} at $l > 1.5°$. The 5 km s^{-1} component is concentrated in a coherent feature within the bowl and forms the half of an apparent ring. It parallels the slightly redshifted portion of the main component, forming the so called *Molecular Ring* (Muench et al. 2007). Figure 1.3 illustrates the global kinematic structure of the Pipe consisting of two primary velocity components indicated by the red (5 km s^{-1}) and white contours (3.5 km s^{-1}).

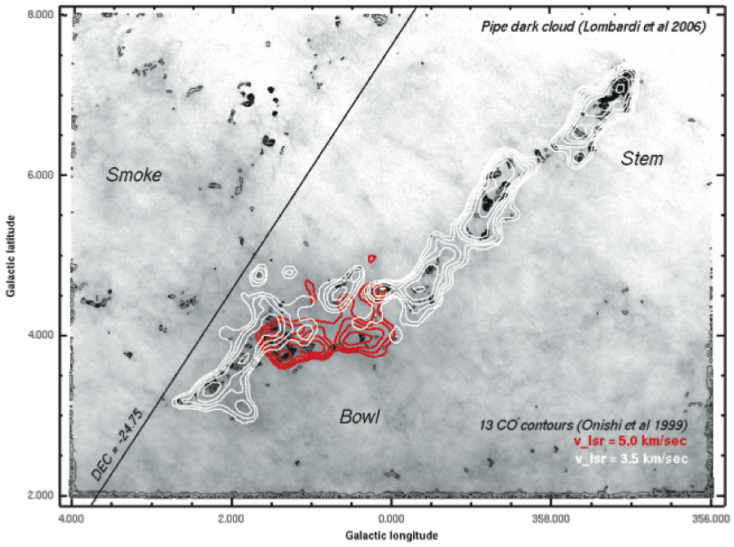

Figure 1.3: Extinction map of Lombardi et al., (2006) over plotted with smoothed ^{13}CO channel map of the two primary velocity components at 3.5 km s^{-1} (*white contour*) and 5.0 km s^{-1} (*red contour*) by Muench et al., (2007).

In 2008 an optical polarimetric survey by F.O. Alves further divided the Pipes main body into three substructures referring to their polarization properties. By tracing the diffuse gas component they found a large-scale magnetic field mostly perpendicular to the clouds main axis, which exerts a pressure of $\approx 10^6$ K km s^{-3} (Frau et al. 2010). The dashed lines in figure 1.4 indicate the different regions. The red lines are proportional to the scale in the upper left hand corner and represent the mean polarization vectors. Note that magnetic field properties inside high column density extinction cores can defer from the derived values in Alves et al., 2008 as the study was based on the diffuse gas components only.

The region of B59 at the northwestern end of the Pipe possesses the lowest polarization values of 1 - 2 % and the highest polarization angle dispersion of $>$ 25 °. In the stem, the main filamentary structure, the mean polarization increases to max. 5 % while the polarization angle dispersion is decreasing to $\sim$ 3 °- 12 °. The bowl, appearing as an irregular shaped gas accumulation on the south-eastern end, shows the highest mean polarization values up to 15 % and the lowest polarization angle dispersion lying below 5 °(Alves et al. 2008).

From this Alves estimated the magnetic field strength of the diffuse gas component to be 17 μ *G* in B59, 30 μ *G* in the stem, and 65 μ *G* in the bowl. Alves followed that most probably the three regions represent different evolutionary stages. While

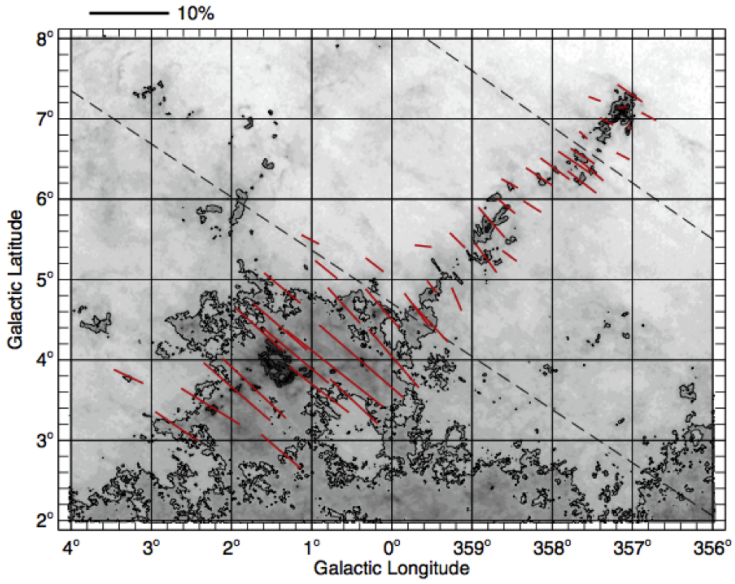

Figure 1.4: Mean polarization vectors (red) over plotted on the dust extinction map of Lombardi et al., 2006. The dashed lines define the celestial meridians defined by $\alpha = 17^h\ 14^m\ 30^s.00$ and $17^h\ 27^m\ 40^s.00$ (Alves et al., 2008).

the weak magnetic field in B59 allowed star formation to appear, the stem seems to be in the stage of ambipolar diffusion as it is contracting in the direction of the field lines, which is indicated by the perpendicular alignment between the magnetic field and the main axis of the stem. When compared to the other parts of the cloud the high polarization degree of the bowl combined with the low dispersion indicates that the magnetic field plays a major role in regulating the collapse of the cloud material. The bowl is most probably in a primordial evolutionary state where fragmentation is just starting (Alves et al. 2008).

2 Molecular Line Observations

The present chapter summarizes basics concerning the physics behind molecular emission as well as observational methods. In the course of this rotational transition properties and possibilities of observation and calibration techniques are discussed.

2.1 Molecular Cloud Structure

The major constituent of molecular clouds is molecular hydrogen (H_2) which is not observable at the temperatures prevailing in such dense environments. Because of its geometry the H_2 molecule possesses no permanent dipole moment and is thus best detected via its first quadrupole line at 500 K which lies significantly above the typical temperatures of molecular clouds ranging between 10 and 20 K (Bergin & Tafalla, 2007). But instead of observing H_2 directly the molecular line emission of species excited due to collisions with the numerous H_2 molecules can be measured. Such molecules are called *tracer* molecules. Very common tracer molecules are the isotopologues of carbon monoxide (CO) as it is the second most abundant molecule after H_2 in the ISM and scales to H_2 as $\frac{H_2}{CO} \sim 10^4$ (Wilson & Rood, 1994). Due to its low excitation temperature in the order of around ~ 10 K and it's low critical density CO is an excellent tracer for H_2 in molecular clouds. In the interstellar radiation field (ISRF) the CO molecule easily becomes dissociated by the UV-radiation of young stars but inside a dense molecular cloud the H_2 molecules shield CO against the ISRF. In the outer regions of the cloud the molecular gas remains mainly in its ionized form with the carbon as CII or C^+ and the hydrogen as HI. Hydrogen can not recombine to H_2 until visual depths of $A_v \sim 0.5$ mag are reached. Due to different self shielding properties carbon monoxide requires much greater depths to recombine. At extinction values of approximately $A_v \sim 1$ mag the interstellar radiation field is blocked sufficiently and C^+ can recombine to C. Carbon monoxide (CO) finally starts to dominate at $A_v \sim 2$ *mag* (Bolatto et al., 2013).

The different self shielding properties can affect the calculated total molecular gas masses as a significant amount of H_2 mass can be missed in the outer regions of a cloud. Wolfire et al. 2010 presents molecular cloud models which take these effects into account. Referring to the photodissociation regions at greater radii such models are called *PDR* models. Figure 2.1, taken from Wolfire et al. 2010, examples the molecular cloud structure like it is explained in the text.

Wolfire et al., 2010 exemplified how the emission of low rotational transitions of the carbon monoxide molecule can be used to derive CO gas masses and furthermore

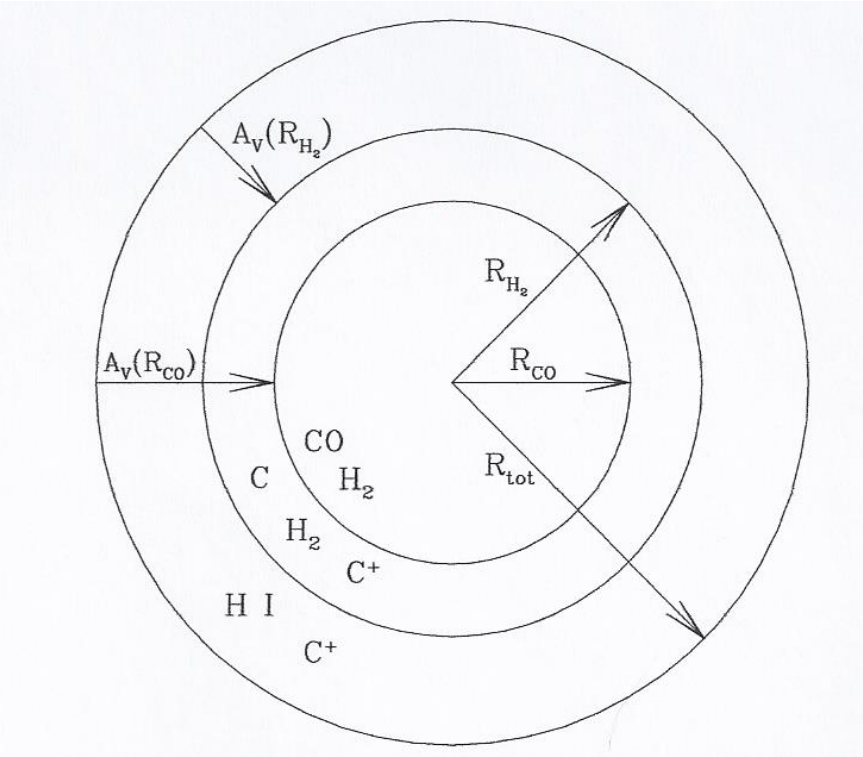

Figure 2.1: Molecular Cloud Structure (Wolfire et al. 2010).

the overall molecular gas mass by applying a scaling factor to the assumed H_2 mass of a molecular cloud.

Lombardi,Alves and Lada (2006) pointed out that if ^{12}CO is used as a mass tracer up to 65% of H_2 mass will be missed. This is caused to equal amounts by the missed H_2 gas in the outer cloud regions at low A_v and by masses at higher column densities where ^{12}CO emission has already saturated. This means that at higher column densities ^{12}CO has grown such in mass that the emission has got optically thick and a deeper look into the cloud is hindered. Fortunately we can use rarer isotopologues of CO as $^{13}C^{16}O$ and $^{12}C^{18}O$ to estimate molecular cloud masses. As they are much less abundant than ^{12}CO their emission saturates at higher optical depths and more central cloud structure is revealed. This becomes visible in the different morphologies of $^{12}C^{16}O$,$^{13}C^{16}O$, and $^{12}C^{18}O$ emission maps like illustrated in figures 2.2 to 2.4.

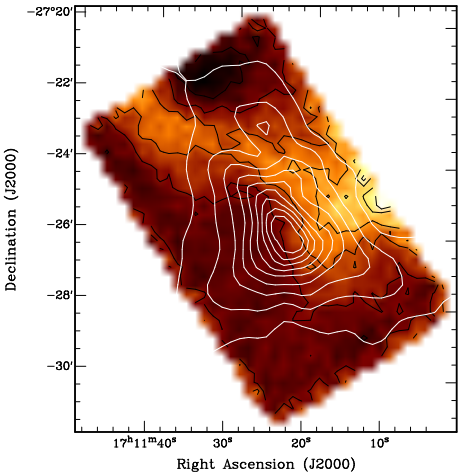

Figure 2.2: ^{12}CO integrated intensity map in B59; contour levels from $10 - 85$ % in steps of 15 % with 100 % $= 26$ K

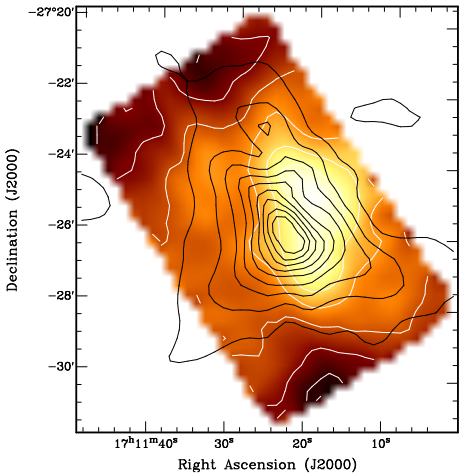

Figure 2.3: ^{13}CO integrated intensity map in B59 contour levels from $10 - 85$ % in steps of 15 % with 100 % $= 10$ K

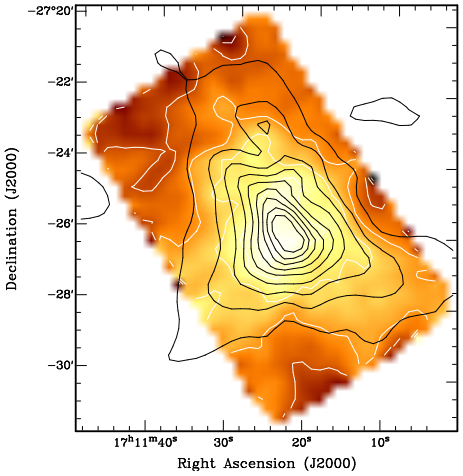

Figure 2.4: C^{18}O integrated intensity map in B59 contour levels from $10 - 85$ % in steps of 15 % with 100 % $= 3.25$ K

2.2 Molecular Transitions and Spectral Lines

The Schrödinger equation of molecules is more complex compared to atoms as molecules have one more degree of freedom and are therefore able to vibrate and rotate. The resulting transitions can be divided into three different categories:

1. Electronical transitions are visible in the optical and UV range of the spectrum and emit energies of a few eV
2. Vibrational transitions having energies of 0.1 eV arise in the IR
3. Rotational transitions with typical energies of $\sim 10^{-3}$ eV are emitting at radio wavelengths

Following the Born-Oppenheimer approximation which treats the nuclear and electronic motions inside a molecule separately, the total energy of a molecular transition is the sum of its rotational, vibrational and electronic transition energies. Pure rotational transitions are only found in very cold regimes for example at temperatures prevailing in molecular clouds. Unfortunately molecular clouds consist mostly of H_2 which has no permanent dipole moment as it is a symmetric and neutral molecule. H_2 can therefore not be rotationally excited and is not visible before its first quadrupole transition at 500 K. However, due to collisions with the numerous H_2 molecules other species which obtain a permanent electric dipole moment can be excited. The most abundant molecule in the ISM after H_2 is carbon monoxide. The CO molecule consists of one oxygen and one carbon atom connected by a triple bond. The two atoms don't share the electrons of their bonding equally as oxygen has a higher positive charge in its nucleus and attracts the electrons stronger than the carbon atom. This results in an asymmetric charge distribution with oxygen carrying a partial negative charge (δ^+). The electric dipole moment of carbon monoxide is 0.112 Db (*Debye*).

The two atoms in the CO molecule can be compared with the two masses in fig. 2.5 rotating around their center of mass. The angular momentum L stands perpendicular to the connecting line between the nuclei r_e and is quantized to integer multiples of $\hbar$. The atoms with masses m_A and m_B and radii r_A and r_B rotate at the *angular velocity* ω. For diatomic molecules we can use the approximation of a rigid rotator. At higher transitions the equilibrium distance between the two nuclei r_e will be stretched by centrifugal forces resulting in slightly lower line frequencies than would be predicted for these energies.

The moment of inertia of a point mass in distance r around a rotation axis is defined as

$$I = mr^2 \tag{2.1}$$

The angular moment is the product of the angular velocity and the moment of inertia (compare to $p = mv$):

$$L = I\omega \tag{2.2}$$

With

$$m_A r_A^2 = m_B r_B^2 \qquad \text{and} \qquad r_e = r_A + r_B \tag{2.3}$$

this can be written as

$$L = (m_A r_A^2 + m_B r_B^2)\omega = (\frac{m_A m_B}{m_A + m_B}) r_e^2 \omega \tag{2.4}$$

with $(\frac{m_A m_B}{m_A + m_B})$ as the reduced mass.

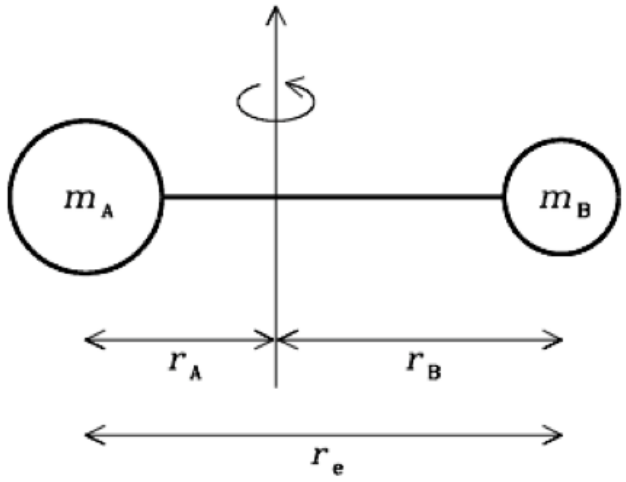

Figure 2.5: Rotating Molecules (http://www.cv.nrao.edu/course/astr534/MolecularSpectra.html)

The rotational energy E_{rot} in this system is defined as

$$E_{rot} = \frac{1}{2}\ I\ \omega^2 = \frac{L^2}{2\ I} \tag{2.5}$$

As the angular momentum L is quantized also the rotational energy has to be. J is the quantum number of angular momentum and the Eigenvalues of L result in

$\hbar^2 J\ (J+1)$ from which follows

$$E_{rot} = \frac{\hbar^2}{2\ I}\ J\ (J+1) \quad J = 0, 1, 2, 3, ... \tag{2.6}$$

In the literature the term $\frac{\hbar^2}{2\ I}$ is often represented by the rotational constant B. With this the rotational energy can be also written as

$$E_{rot} = B\ J\ (J+1) \quad \text{and} \quad \Delta E_{rot}(1 \to 0) = 2\ B \tag{2.7}$$

$$\Delta J = +1(emission) \tag{2.8}$$

$$\Delta J = -1(absorption) \tag{2.9}$$

The quantization of angular momentum and rotational energy causes line radiation to be emitted at discrete frequencies. The transition between two energy states can be described by the Einstein coefficients which give the probability of spontaneous de-excitation (A_{lu}), absorption (B_{ul}), and stimulated emission (B_{lu}).

If a molecule, for example carbon monoxide, suffers enough collisions with H_2 molecules that the number of upward transitions equals the spontaneous decay, the molecule becomes thermalized and we expect the upper level population to follow a Boltzmann distribution. The density referring to such conditions is called *critical density* n_{crit} and is defined as

$$n_{crit} = \frac{A_{ul}}{\sigma v} \tag{2.10}$$

with σ as the collisional cross section and v as the average velocity of the system. Typical values for sigma lie at $\sim\ 10^{-15}\text{cm}^2$. The velocity can be calculated via the concept of kinetic temperature founded in *The Kinetic Gas Theory*:

Under the conditions of a constant particle number and constant total energy of the system the underlying theoretical assumptions can be described as follows: A large number of molecules of infinitesimal mass, separated by large path lengths and following Newton's Laws of Motion is moving randomly within a terminated volume with a constant distribution of speeds. The molecules undergo elastic collision with each other and with the walls but apart from that exert no forces on each other.

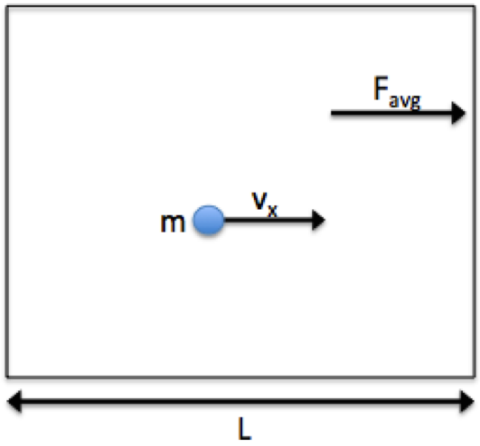

Figure 2.6: Kinetic gas pressure and exerted average force on a container wall

The average force on the container wall can be expressed as:

$$F_{ave} = \frac{mN\overline{v_x^2}}{L} \tag{2.11}$$

(with N as the total number of particles and m the particle mass)

Assuming random motions in all three directions in space

$$\overline{v^2} = \overline{v_x^2} + \overline{v_y^2} + \overline{v_z^2} = 3\overline{v_x^2} \tag{2.12}$$

the exerted pressure on the walls can be expressed as:

$$P = \frac{F_{ave}}{L} = \frac{mN\overline{v^2}}{3LA} = \frac{mN\overline{v^2}}{3V} = \frac{N}{3V}m\overline{v^2} \tag{2.13}$$

(with L representing the box length and A the surface of the box)

In terms of average molecular kinetic energy this becomes:

$$P = \frac{2}{3}\ \frac{N}{V}\ \overline{\left[\frac{1}{2}\ mv^2\right]} \tag{2.14}$$

A comparison to the ideal gas law allows to establish a relationship between pressure, volume and temperature and leads to a concept of kinetic temperature.

$$PV = nRT \quad \Leftrightarrow \quad PV = \frac{2}{3}\ N\ \overline{\left[\frac{1}{2}\ mv^2\right]} \tag{2.15}$$

$$\Rightarrow \qquad T = \frac{2}{3}\ \frac{N}{nR}\ \overline{\left[\frac{1}{2}\ mv^2\right]}\ =\ \frac{2}{3}\ \frac{1}{k}\ \overline{\left[\frac{1}{2}\ mv^2\right]} \tag{2.16}$$

$$\Rightarrow \qquad \overline{\left[\frac{1}{2}\ mv^2\right]} = \frac{3}{2}\ kT \tag{2.17}$$

$$\Rightarrow \qquad v = \sqrt{\frac{3kT}{m}} \tag{2.18}$$

k is equal to the ideal gas constant divided by Avogadro's number: $k = \frac{R}{N_A}$.

With this the critical density for a given gas temperature can be calculated via equation (2.10). If the volume density in the medium lies above the critical density of a molecular transition the excitation temperature corresponds approximately to the kinetic temperature of the gas. When probing molecular transitions of different critical densities it is possible to trace different gas components. For example the critical density of CO lies at $\sim\ 10^3$ cm s^{-3} whereas that of N_2H^+ lies at $\sim\ 10^6$ cm^{-3}. So CO can be used as a tracer of the diffuse material enveloping molecular cloud cores while N_2H^+ applies to the more central and denser parts. This behavior will be discussed in detail in chapter 3 where molecular emission maps are presented which illustrate the different emission properties of the investigated molecules. Table 2.1 summarizes the molecular line parameters of the species concerned in the text. Frau et al. divided the molecular species into *early-* and *late type* molecules referring to their different emission properties. Species with low critical densities such as CO are expected to be present very early when the core is just starting to gravitate. With time as the core evolves to higher densities other molecular species like nitrogen bearing and deuteriated molecules develop. Early-type molecules are expected to deplete much earlier from the gas phase, meaning their freezing out onto dust grains, whereas late-type molecules stay unaffected by depletion up to densities of 10^6 cm^{-3} (see e.g. Tafalla et al., 2002; Bergin & Tafalla 2007; Aikawa et al., 2008).

Molecule	Frequency $[GHz]$	A_{ul} $[s^{-1}]$	n_{crit} cm^{-3}
^{12}CO	115.27120	7.203×10^{-8}	2.047×10^{3}
HCN	88.63160	2.407×10^{-5}	6.842×10^{5}
HNC	90.66356	2.690×10^{-5}	7.646×10^{5}
HCO^+	89.18853	4.251×10^{-5}	1.208×10^{6}
N_2H^+	93.17161	3.896×10^{-5}	1.107×10^{6}

Table 2.1: Frequencies, Einstein A coefficients and critical densities for $T = 10$ K of the investigated molecular species

P. Frau is only one author among others who tries to link a chemical clock to the ages of stellar cores in order to derive their evolutionary state by their chemical composition. Several authors investigated chemical profiles of molecular cores in order to link them to time-dependent chemistry models. Relevant studies can be found for example in Kontinen et al., (2000), Tafalla et al., (2004), Aikawa et al., (2003) or Morata et al. (2003, 2005).

2.3 Radio Antennas

Radio antennas can work as transmitters as well as receivers; in the following only the receiving case is considered. A radio receiver consists of electric conducting material such as metal sheet, metal screen or wire grill. The received electro-magnetic waves induct a current into the antenna. The most commonly used antennas are of parabolic form because with this shape a high directivity can be reached, which means that the radio waves can be reflected in a narrow beam to the subreflector. The position of the subreflector depends on the telescope type and can be either before or behind the prime focus (Cassegrain or Gregorian systems, respectively).

As can be easily seen in figure 2.7 the strength of the radio waves depends on the angular direction. A radiation pattern shows the distribution of the antennas gain in different directions. The main beam is defined as the solid angle where the antenna receives a power of $P(\theta, \phi) = 1$. The directivity of a telescope is defined as the ratio of radiation intensity per unit solid angle in a particular direction and the averaged radiation over all directions. An antenna's directivity is just another expression of its maximum gain. By the ratio of the main beam solid angle to the antennas angle the main beam efficiency (μ_{MB}) can be derived, a measurement of how well the power pattern is concentrated in the main beam. Figure 2.7 shows a typical power pattern of a radio telescope and demonstrates the different directions of main beam and side lobes.

The angular extent of the main beam is named the Half Power Beam Width (HPBW).

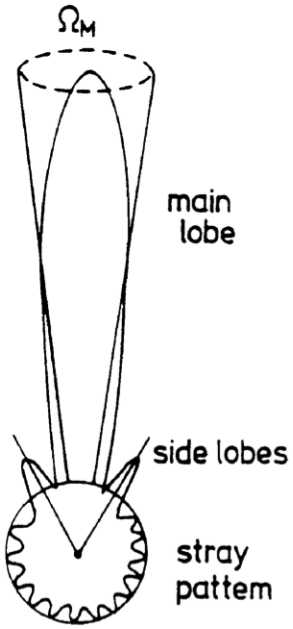

Figure 2.7: Main Beam and near and far side lobe pattern (Wilson et al., 2009, chapter 7)

It is defined as the angle between two points of the main beam where the normalized power pattern falls to the half of the maximum, and is also sometimes referred to as Full Width to Half Power (FWHP).

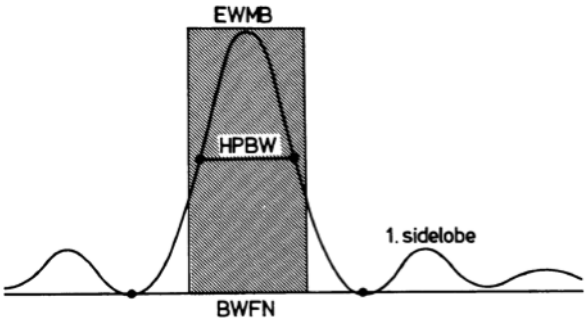

Figure 2.8: Sketch of half power beam width; EWMB is the equivalent width of the (*full*) HPBW and BWFN denotes the beam between first nulls indicated by the two dots. (Wilson et al., 2009, chapter 7)

Before being finally transmitted to the receiver the electromagnetic wave is inducted into the feed horn, most often a horn antenna. Coaxial cables attached at the feed horn transmit the signal to the Front End where it is converted for further processing.

An important parameter is the *noise temperature* of the antenna. While the received radio signals are pretty weak there can be considerable noise caused by the thermal

motion of the charge carriers in the electric wires. The antenna temperature (T_A^*) can be derived by measurements of an object with known radiation temperature. This is important because measured intensities, always referred to as brightness temperatures, have to be corrected for the antenna temperature (Wilson et al., 2009).

For further processing it is necessary to amplify the received radio signals without increasing the electrical noise of the components. So called Low Noise Amplifiers (LNA) are placed at the front end of the receiver circuit to push the incoming signal. In the following the high frequency signals have to be lowered again for further processing which is called Heterodyning. The signal can be lowered to chosen output frequencies by mixing of the radio frequency with the frequency of a local oscillator. By combining the two frequencies two additional outputs (beat frequencies) are generated which consist of the sum and the difference of the two input frequencies respectively.

The chosen beat frequency is called Intermediate Frequency (IF) which is amplified again to undergo a bandpass filtering process where only a selected range of frequencies is transmitted. The concept of an IF has high advantages for back end facilities such as filters or spectrometers. In this way they have not to be adjusted to different frequencies and can always process at the same IF independent of the received radio waves frequency (Wilson et al., 2009).

Figure 2.9: MOPRA 22 m radio telescope in the Warrumbungle Mountains (AUS); Credit: ATNF

2.4 Single Dish Observational Methods

2.4.1 The Radio Window

In a frequency range of 15 MHz to 1.5 THz the Earth's atmosphere is transparent for radio waves. This frequency range is variable as the cut-offs depend on element abundances in the atmosphere as well as electron densities in the upper ionosphere. In the high frequency range mainly the rotational absorption bands of water vapor H_2O and molecular oxygen O_2 in the troposphere limit the Earth's transmissivity. Water vapor shows bands at 22.2 GHz and 1.35 GHz while O_2 has an exceedingly strong band at 60 GHz (Wilson et al., 2009, chapter 1). Above 300 GHz also the absorption by other abundant molecules such as N_2 and CO_2 counts to the limitation factor. The lower frequency limit is governed by electron densities in the ionosphere in a height of $\leq$ 400 km. The exact cut-off value depends on time and space weather and can vary between 4.5 MHz at night and 11 MHz at daytime. Fortunately most interesting signals are found in the high frequency range as interstellar molecules radiate at mm wavelengths. As water vapor is one of the limiting factors it is possible to extend the accessible frequency range by observing from high altitude locations in a dry climate. However, to avoid O_2 absorption it is necessary to carry out measurements from above the Earth's atmosphere e.g. with satellites or balloons (Wilson et al., 2009).

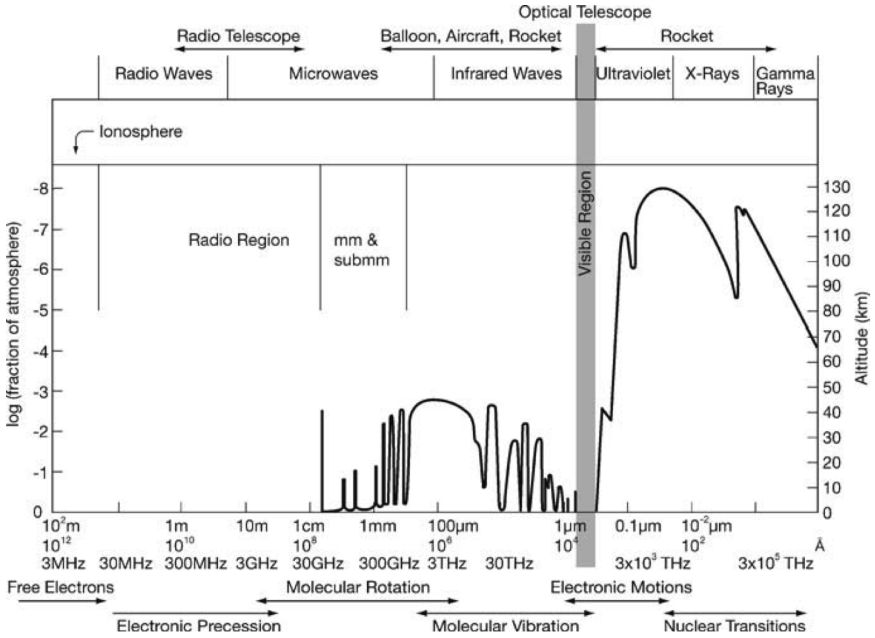

Figure 2.10: Transmissivity of the Earth's atmosphere for electromagnetic radiation; Credit: Wilson et al., 2009

2.4.2 The Earth's Atmosphere

The Earth's atmosphere alters the transmitted waves. The strength of the signal decreases and atmospheric emission lines are added. While the main constituents of the troposphere (N_2, O_2, Ar) stay relatively constant in their abundances some minor constituents (H_2O, CO_2, O_3) can change rapidly.

Water vapor can vary erratically in its concentration depending on local weather conditions and altitude. The amount of A 3sigma detection criterion was applied."can be measured by radio observations at 225 GHz combined with models of the atmosphere (Wilson et al., 2009, chapter 1). CO_2 has an average percentage of 0.03% but shows a seasonal as well as a secular trend. In the last decades a slow but continuous increase was noted (Greenhouse Effect). On the contrary ozone has been found to decrease with time which has dramatic consequences as the ozone layer protects the earth from the solar UV radiation. In addition ozone too shows seasonal and geographic variations (Wilson et al., 2009).

2.5 Calibration Methods

Similar to optical calibration methods celestial standard sources of known radio flux densities are used to derive antenna parameters described in section 2.4. Catalogues of such sources are available for a wide range of frequencies. Flux density calibrations are usually measured using horn antennas. The antenna parameters can then either be computed theoretically or can be measured in an antenna test range. Afterwards the same objects are measured again with the large telescope to be calibrated (Wilson et al., 2009, chapter 8). When observing at mm and sub-mm wavelengths special attention has to be drawn to the Earth's atmosphere. As described above atmospheric absorption properties can change rapidly in the short wavelength regime. A standard calibration procedure in spectral line mm astronomy is the so called *chopper wheel* method after Downes (1989) and Kutner & Ulich (1981). In this procedure the receiver output of cold sky measurements are compared to the receiver output of an object with ambient temperature, placed before the feed horn. By subtracting the two measurements one gets the receiver output calibration depending on the atmospheric absorption for a given frequency. In this way system temperature and antenna (noise) temperature can be identified. For the observation of spectral lines one more calibration step is necessary as line radiation is almost always only a small fraction from the total power received. The signal is therefore damped by system noise, spillover from the antenna and possible background noise (Wilson et al., 2009). The best way to solve this problem is to compare the signal of interest with another signal that contains the

same total power but contains no line radiation. One way to do this is the so called *Position Switching* or *Wobbler Switching*. Here the received signal is compared with another signal obtained at a nearby position in the sky. An alternative procedure is *Frequency Switching* where the frequency of the Local Oscillator is switched at a rate of several Hz. In this way two measurements are received whose difference is direct proportional to the final spectrum (Wilson et al., 2009).

3 The Spectral Data Sample

3.1 Observation and Reduction Methods

The sample underlying this master thesis was obtained with the Australian 22 m telescope MOPRA (fig. 2.9) in the time July 20th to 28th in 2008. MOPRA is a single dish telescope operated by the Australian Telescope National Facility (ATNF). It is located at an elevation of 866 m in the Warrumbungle National Park 450 km north-west of Sydney at a latitude and longitude of $-31°16'58''$ and 149 $°5'58''$, respectively. Observations are possible in a wavelength range between 20 cm and 3 mm with backends capable of spectral line observations. Observing at short wavelengths is generally conducted during the winter months when the water vapor level in the atmosphere reaches its annual minimum values (Ladd et al. 2005). For our observations the MOPRA spectrometer called MOPS was used in narrow-band zoom mode to obtain multiple molecular line transitions simultaneously (Wilson et al., 2006). The MOPS spectrometer possesses an overall beam width of 8.3 GHz which is divided into four overlapping sub bands of 2.2 GHz, each equipped with its own local oscillator. Like it is described in Wilson et al. 2006 each sub band is then digitized in 2-bit samples operating at the Nyquist sampling rate. A polyphase digital filter bank divides the sub bands into larger numbers of independent channels. This way a narrow band observing mode can be addressed which provides up to four 137.5 MHz wide zoom bands within each 2.2 GHz sub band. Each zoom band consists of 4096 channels so the obtained velocity resolution was 0.11 km s^{-1}. Throughout the full 8.3 GHz range up to 16 zoom bands can be placed at chosen locations which allow a simultaneous observation mode (Wilson and collaborators, 2006). In two observational phases we obtained simultaneously spectra of the $(J = 1 \rightarrow 0)$ transitions of the carbon monoxide isotopologues ^{12}CO, ^{13}CO, $C^{17}O$ and $C^{18}O$, as well as of the high density tracers HCO^+, $H^{13}CO^+$, HCN, HNC, $H^{13}CN$, $N_2H^+$and SiO.

Ladd et al. 2005 presented measurements of the beam size, shape, and beam efficiency in the frequency range 85 - 115 GHz for the MOPRA telescope. Thus for the carbon monoxide isotopologues with frequencies at about 115 GHz the MOPRA beam

has a resolution of 33 arc seconds. All other species emit at frequencies below 100 GHz and the beam resolution decreases to 36 arc seconds.

Using the *on-the-fly-mode* of the MOPRA telescope we mapped each line emitting area in longitude and latitude for 90 minutes, respectively. In this mode the telescope takes data continuously while scanning the sky. The accurate coordinate information is written into the data file with each spectrum. For flux calibration the radio source AH Sco was chosen, a red super giant positioned at $\delta = 17°11'17.02''$ and $\alpha = -32^h\ 19^m\ 30.71^s$. The calibration was checked every 90 minutes. The typical system temperature (T_{sys}) for our observations was ~ 222 K.

The spectral maps were reduced using the ATNF Spectral Analysis Package (ASAP) and were initially baseline subtracted before averaged using a system temperature weighting (Rathborne et al., 2009). ASAP possesses a routine for an automatic search of spectral lines and is able to build three dimensional spectral cubes in (x, y, λ). Such can be imagined as stacked images of the same region in the sky differing in their wavelength. The contained spectra are in units of antenna temperature (T_A^*) with a median noise of 0.13 K per channel. A 3 σ detection criterion was applied.

3.2 The Molecular Core Sample

The data provided consist of molecular line spectral cubes and extinction maps of three different regions in the Pipe nebula. Extinction maps were originally produced by Lombardi et al., 2006 using 4.5 million sources taken from the Two-Mass-All-Sky-Survey in the near infrared. The method, called near infrared color excess technique, measures the degree of reddening of light from background stars toward a given line of sight due to the absorption (*extinction*) and re-emission of dust particles. Thus the amount of light reduction is a measurement of the dust column density. Extinction values are given in magnitudes and can be calculated for different spectral bands. A small letter next to the symbol (A) denotes the given frequency range. In the present work extinction values are given in visual magnitudes A_V.

Investigated were the star forming region B59 at the Pipe's north-western end, a neighboring core (Core 20), and part of the Molecular Ring lying at the south-eastern end of the nebula (see section 1.4 for a further description of overall kinematic and magnetic properties of these regions).

Spectral emission maps of the ^{12}CO, ^{13}CO, C^{17}O, C^{18}O isotopologues were obtained for all three sample cores. The remaining species were only observed for B59 and the Molecular Ring but not for Core 20. Table 4.1 in section 4 gives an outline of the measured line intensities at the extinction peak. The figures 3.1 to 3.3 show extinction maps of B59, C20, and the Molecular Ring.

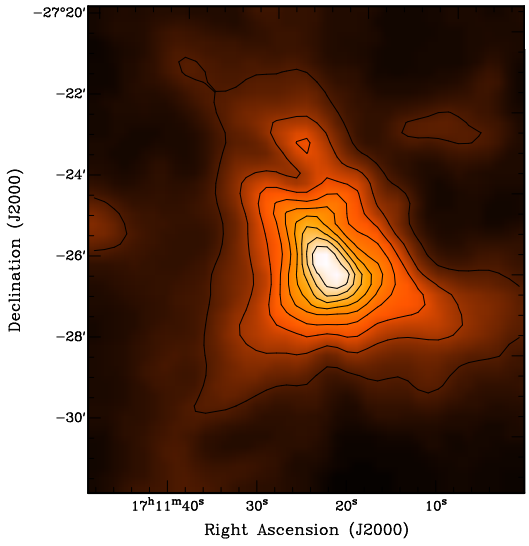

Figure 3.1: B59 $0.2° \times 0.17°$ extinction map; contour levels are $10 - 90$ % in steps of 10 % with 100 % = 78 mag

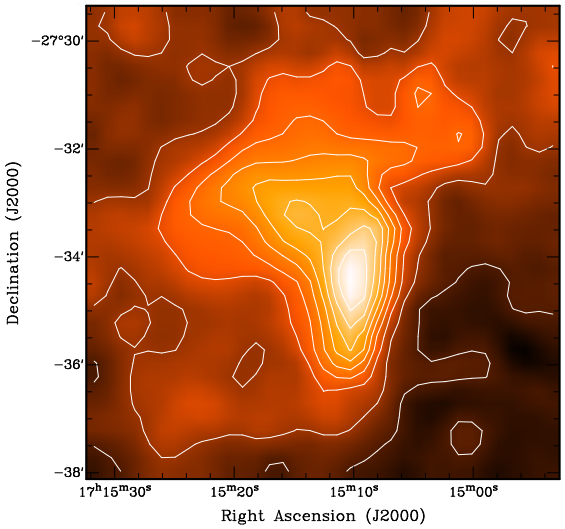

Figure 3.2: C20 $0.14° \times 0.14°$ extinction map; contour levels are $10 - 90$ % in steps of 10 % with 100 % = 14.4 mag

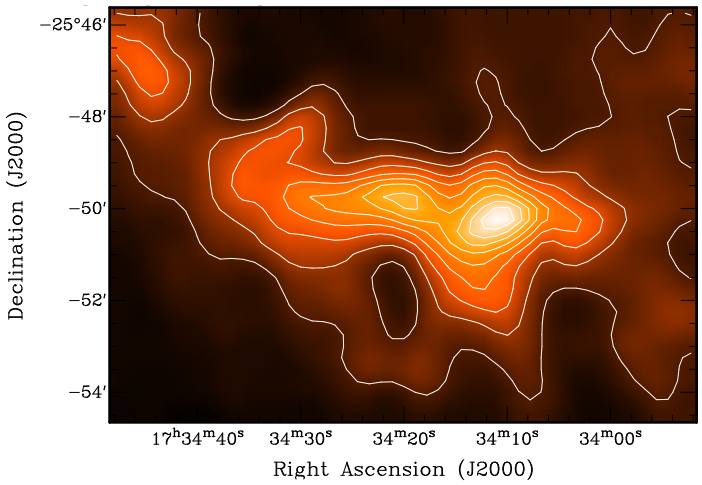

Figure 3.3: Molecular Ring $0.14° \times 0.2°$ extinction map; contour levels are $10 - 90$ % in steps of 10 % with 100% = 44 mag

In the star forming region B59 striking high extinction values of up to 78 mag were measured. In comparison, Core 20 is peaking in extinction at approximately 14.4 mag and the Molecular Ring is reaching density values of approximately 44 mag. As building the main block of the Pipe's bowl the Molecular Ring most probably possesses much more extinction cores. The adjusted extinction map in fig. 3.3 shows with an area of 0.14°$\times$ 0.2°only a small sector of the original extinction map containing the complete Molecular Ring but at least two extinction cores become apparent.

In figure 3.4 the extinction map produces by Lobardi et al. in 2006 is shown. The three investigated regions are highlighted by circles. The big and yellow circle in the north refers to B59 and Core 20 respectively whereas the Molecular Ring is indicated by a black circle in the southeast. Referring to the concept of a chemical evolutionary sequence presented in section 2.3, it is possible that the sample cores represent different evolutionary stages. A detailed description of the differences in emission behavior of molecular species will be presented in chapter 5.

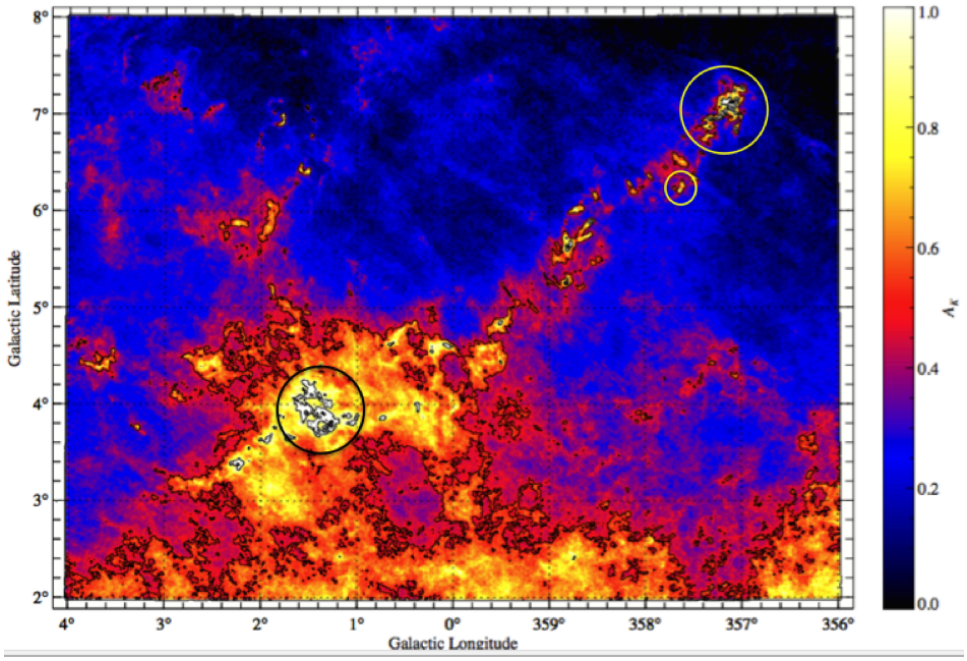

Figure 3.4: Extinction map of Lombardi et al., 2006. The three investigated regions are highlighted by a big and small yellow circle representing B59 and Core 20 respectively, and the Molecular Ring marked by a black circle in the southeast of the Pipe.

Molecule	Intensity **B59** [K km s^{-1}]	Intensity **C20** [K km s^{-1}]	Intensity **mol. ring** [K km s^{-1}]
^{12}CO	13.00 $(3\bar{\sigma} = 0.98$ K)	6.00 $(3\bar{\sigma} = 1.45$ K)	21.15 $(3\bar{\sigma} = 1.03$ K)
^{13}CO	8.01 $(3\bar{\sigma} = 0.62$ K)	2.60 $(3\bar{\sigma} = 1.18$ K)	6.16 $(3\bar{\sigma} = 0.08$ K)
C^{18}O	1.72 $(3\bar{\sigma} = 0.55$ K)	0.46 $(3\bar{\sigma} = 1.09$ K)	0.53 $(3\bar{\sigma} = 0.57$ K)
HCN	0.86 $(3\bar{\sigma} = 0.26$ K)	-	0.20 $(3\bar{\sigma} = 0.16$ K)
$H^{13}CN$	0.22 $(3\bar{\sigma} = 0.86$ K)	-	0.14 $(3\bar{\sigma} = 0.09$ K)
HNC	1.20 $(3\bar{\sigma} = 0.39$ K)	-	0.70 $(3\bar{\sigma} = 0.46$ K)
HCO^+	0.95 $(3\bar{\sigma} = 0.42$ K)	-	0.007 $(3\bar{\sigma} = 0.09$ K)
$H^{13}CO^+$	0.70 $(3\bar{\sigma} = 0.46$ K)	-	0.09 $(3\bar{\sigma} = 0.11$ K)
N_2H^+	1.90 $(3\bar{\sigma} = 0.78$ K)	-	0.70 $(3\bar{\sigma} = 0.28$ K)

Table 4.1: Integrated intensities at the extinction peak per beam with median 3 $\bar{\sigma}$ noise in brackets

4 Data Analysis

In this chapter the different analysis methods applied to the data set will be presented. Although the provided data were already reduced and baseline subtracted a lot of work still had to be done. The aim of this section is to describe the process how the original spectral maps were treated to finally receive significant results. In order to give a comprehensible presentation of the analyzing process the following section is mostly aligned with the used software. Three different software packages are discussed:

- At first the Australian toolkit karma with its special interactive graphic tool kvis was used to get a first impression of the data. For further analysis the GILDAS/-CLASS package (IRAM) was used;
- Following on with GILDAS, the on-site software package of the IRAM 30 m telescope, the CLASS package was used to extract spectral line parameters
- Final plots reduced to just significant data points were obtained using the interactive computational environment Ipython Notebook.

The provided data set comprised spectral data cubes in FITS format as well as moment 0 maps $(mom0)$. The latter represent a special reduction method in which the three-dimensional data cube is summed over one axes and the displayed intensity maps are integrated over a broader velocity range. The investigated molecules and their parameters (including the calculated threshold representing three times the median spectral noise $\bar{\sigma}$) are given in table 4.1.

4.1 Dust Density and Molecular Line Emissivity Distribution in karma/kvis

In a very first step the fits data cubes of the $(J = 1 \rightarrow 0)$ line transitions of the different molecules were examined in karma/kvis to gain a first hint of the intensity distribution throughout the cores. A graphical user interface allows determining the intensity of the emission line at every single pixel in every single channel. The user is able to extract every spectrum directly. Additionally one has the possibility to play a movie running through the spectral cube which helps to identify the central emission peak. The emission peaks can be highlighted by different color justifications.

For the first time it is somehow tricky to discover all possible functions as they are well hidden in the user interface. A desktop snapshot in figure 4.1 shows the output configuration after starting the program. In the beginning a black display window and a green window appear. The black window contains the `Files` button in its upper left corner. The loaded files appear in the green browser and can be selected by holding the mouse cursor on the image button below. In the example in figure 4.1 the spectral cube of the $^{12}CO(J = 1 \rightarrow 0)$ mapping is selected. One can change the `main` file when setting it to `off` or `alt`. Once a data set is chosen the `movie` option allows to run through the cube in a movie. The respective interface can be found in the `view` window which is to open by the equivalent `View` button in the display window. Figure 4.2 shows the interface after opening all required functions. The `view` window can be found in the upper right corner with the movie window just below.

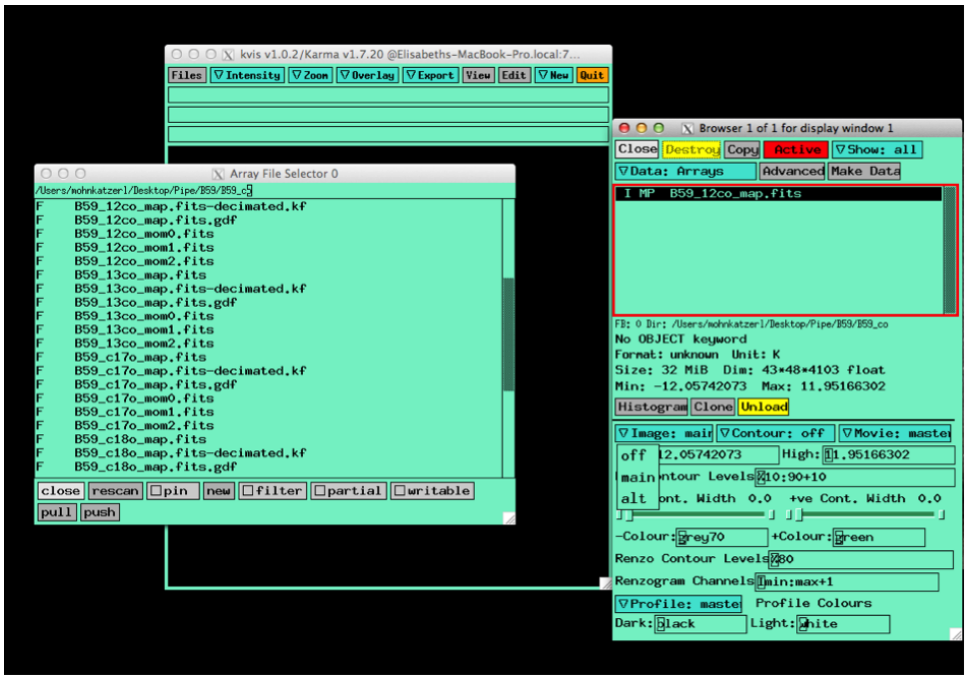

Figure 4.1: Starting interface of karma/kvis

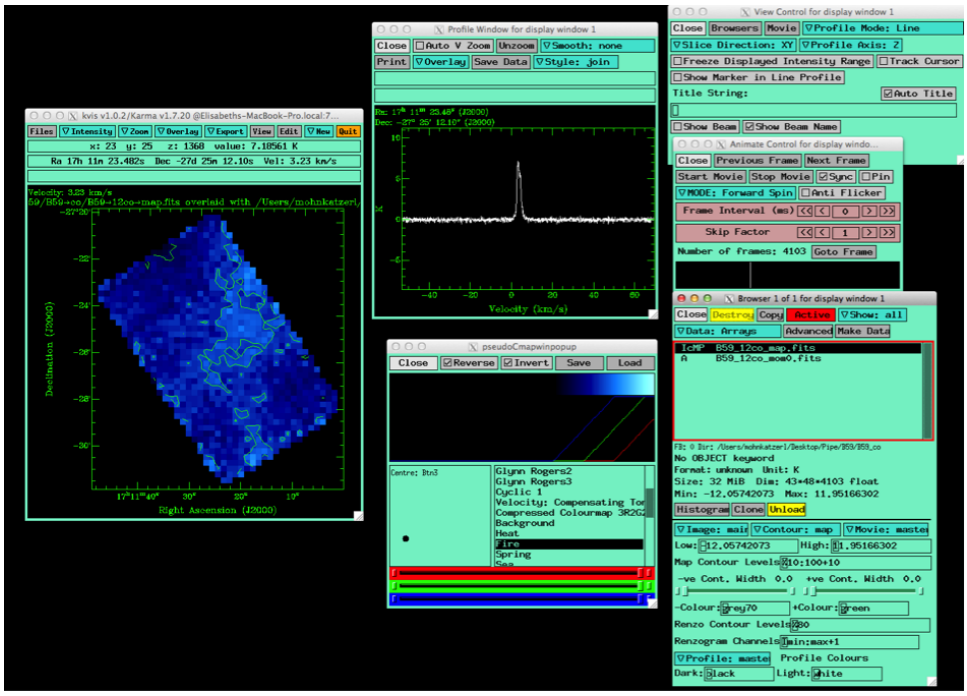

Figure 4.2: Working interface of karma/kvis

In fig. 4.2 the movie has already been played to the peak emission velocity range lying for the Pipe at $\sim$ 4 km s^{-1} (see section 1.4). This can be seen in the Profile Window in the middle range of fig. 4.2. Here the spectrum is extracted directly out of the map by leading the mouse over the individual pixels. So one can get a good impression how the line shape behaves for the different regions of the core. The Profile Window can also be opened in the `view` interface where different profile modes can be chosen. The Profile window gives not only information about peak temperature but also shows the exact position of every pixel. Eventually the *Intensity* button in the display window contains a lot of different color adjustments for a clear presentation of the data. This can be further enhanced by overlaying the map with counters specified for an accurate binning range. Latter can be achieved by activating the *map* function in the *Counter* menu right beside the *Image* menu in the green data browser. Not far underneath the *Map Contour Levels* can be defined.

In this first work step much can be learned. One immediately gets rough estimates of the different peak temperatures of the emitting molecules and their spatial distribution. On the one hand the line emitting regions can be directly compared as well as in their location as in their emission features, while on the other hand this can also be compared with the the extinction structure of the core (fig. 3.1 to 3.3). In the following three paragraphs I will give an overview of the peculiarities of the three investigated cores resulting in a comparison of their emission properties. The used color scales in-

dicating the line intensity are adjusted individually for each spectral line and can not be used for general comparisons.

Extinction and Emission Properties of B59 Like already mentioned above one of the most interesting things to compare are the differences in molecular abundance profiles with rising H_2 column density. Therefore it is practicable to over-plot the integrated intensity maps of molecular radiation with extinction core contours (fig. 3.1).

B59 was found to show the strongest emission in ^{12}CO when compared to the other sample cores followed by its rarer isotopologues ^{13}CO and $C^{18}O$. Table 4.2 is part of the summary in the end of the chapter and provides an overview over measured maximum temperatures and temperatures measured at the extinction peak directly.

In the following moment zero velocity integrated sky maps of the molecular line emission in B59 are presented together with an illustration displaying the extinction contours of B59. Figure 4.3 shows the distribution of the ^{12}CO emission line. As can be easily seen the radiation is concentrated toward the extinction core but not reaching the extinction peak. The reason is that the emission of ^{12}CO fast becomes optically thick when reaching higher densities and escaping photons are re-absorbed instead of leaving the cloud. Thus ^{12}CO is best used to trace the diffuse less dense parts of a molecular cloud core.

In comparison to ^{12}CO the ^{13}CO emission is less affected by saturation at higher optical depths and will trace the gas to higher densities before getting optically thick. This can be seen in figure 4.4 when compared to the ^{12}CO emission map in figure 4.3. the ^{13}CO emission has a more central distribution and is radiated almost from the extinction peak.

This effect gets even more stronger in the case of $C^{18}O$ which is in general found to stay optically thin up to higher densities. So it can be used to trace broader extinction ranges which is of great importance for e.g. column density calculations. The optical properties of the $C^{18}O$ isotopologue will be investigated and discussed in detail in chapter 5. As can be seen in fig. 4.5 the $C^{18}O$ emission is centrally concentrated radiating directly from the extinction peak. Of the $C^{17}O$ isotopologue no significant emission could be measured, which is also true for the other two cores. This component will be treated together with the other non-detections in chapter 5.

In order to map the most dense parts of the molecular core high column density tracers as given in table 4.1 were used since they are expected to radiate from the central extinction peak. To illustrate this fig 4.6 shows the detected N_2H^+ emission of B59. The emission is found to radiate directly from the center, the white dots represent

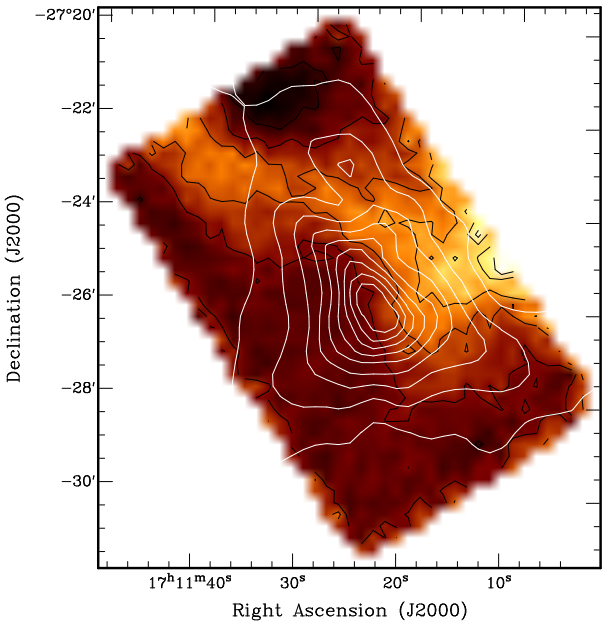

Figure 4.3: Integrated Intensity map of ^{12}CO in B59 (*black*) overlaid with extinction contours (*white*); ^{12}CO emission contours are from $10 - 90$ % in steps of 15 % with 100 % $= 26.3$ K km s-1

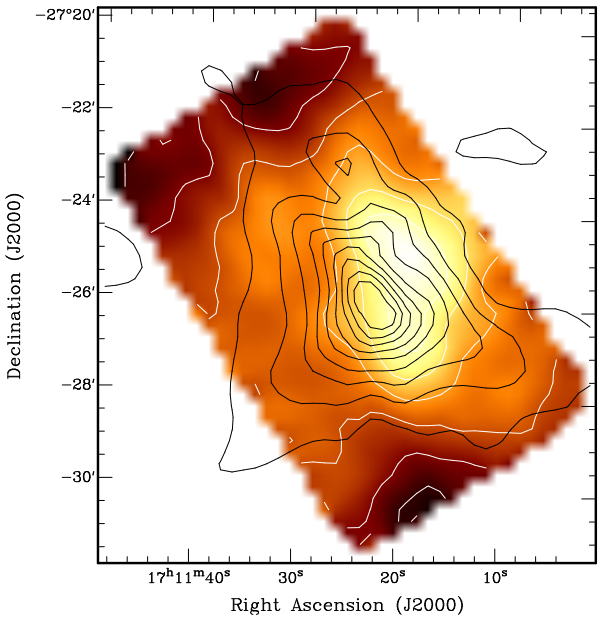

Figure 4.4: Integrated Intensity map of ^{13}CO in B59 (*white*) overlaid with extinction contours (*black*); ^{13}CO emission contours are from $10 - 90$ % in steps of 15 % with 100 % $= 9.7$ K km s-1

single pixels where the interpolation failed. The related tracers HCN, HNC, $H^{13}CN$ show a similar radiation behavior whereas HCO^+ traces a somewhat broader extinction range. This is a very useful tool because like the other high column density tracers HCO^+ remains optically thin. Figure 4.7 pictures the HCO^+ emission in B59; a complete illustration of the whole data set can be found in the appendix.

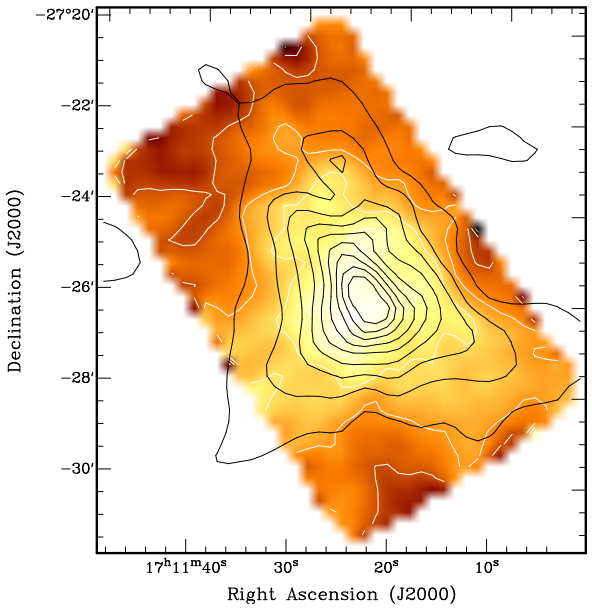

Figure 4.5: Integrated Intensity map of $C^{18}O$ in B59 (*white*) overlaid with extinction contours (*black*); $C^{18}O$ emission contours are from $10 - 90$ % in steps of 15 % with $100\ \% = 3.25\ K\ \mathrm{km\,s^{-1}}$

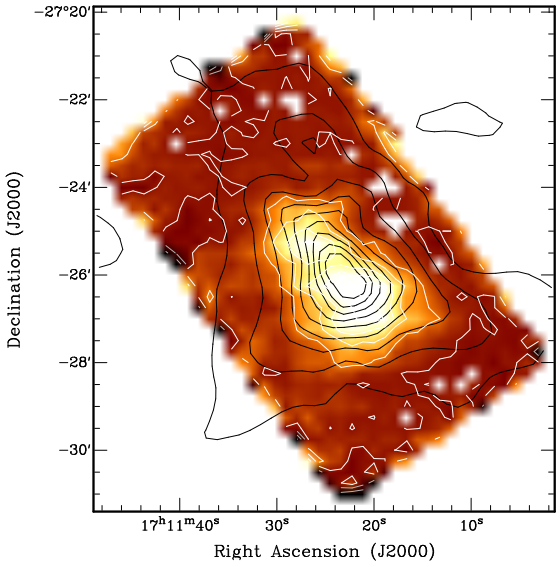

Figure 4.6: Integrated Intensity map of N_2H^+ in B59 (*white*) overlaid with extinction contours (*black*); N_2H^+ emission contours are from $10 - 90$ % in steps of 10 % with 100 % $= 2.52$ K km s^{-1}

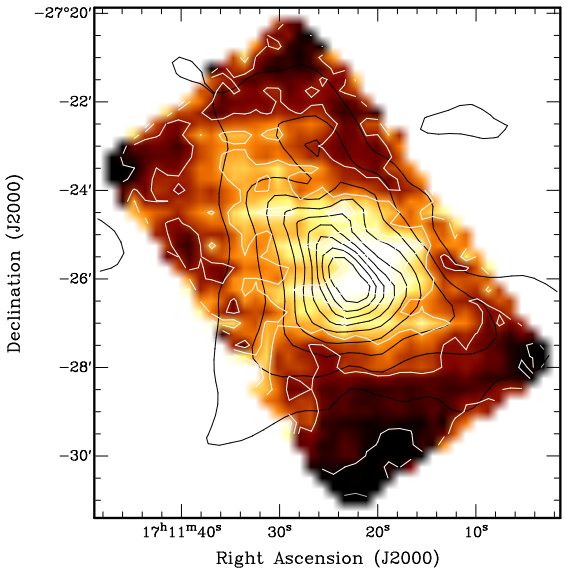

Figure 4.7: Integrated Intensity map of HCO^+ in B59 (*white*) overlaid with extinction contours (*black*); HCO^+ emission contours are from $10 - 90$ % in steps of 10 % with 100 % $= 1.19$ K km s^{-1}

Extinction and Emission Properties of C20 Core 20 of our sample lies in direct neighborhood of B59 as can be seen in fig 3.4 in section 3.2. Unfortunately we obtained only measurements of the CO isotopologues as we were running out of time. Figure 3.2 shows the C20 extinction core with peak density values of $\sim$ 14.4 mag. When compared to the other cores CO emission at these extinction ranges turned out to be the least intense reaching temperatures of 7.5 K km s^{-1}. The integrated intensity of ^{12}CO over plotted with extinction contours in figure 4.8 appears to be more centrally concentrated than in B59 which is most likely due to the lower density values. However, at $A_v \approx 14$ mag the ^{12}CO emission in B59 shows broad scatter in intensity with values ranging between 11.2 K km s^{-1} and 21.9 K km s^{-1}. As described above and as one can see in figure 4.4 the ^{12}CO emission in B59 is located to the western side of the core and the outer extinction contours trace a bigger intensity range.

For completeness at this point the corresponding intensity values of the ^{12}CO component in the Molecular Ring are to mention. At $A_v \approx 14$ mag these range between 19.24 K km s^{-1} and 23.5 K km s^{-1} making the Ring the brightest of our sample cores in the ^{12}CO ($J = 1 \rightarrow 0$) transition.

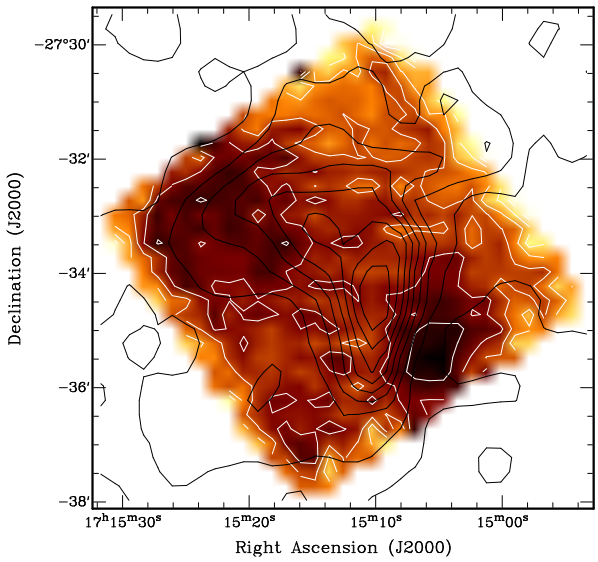

Figure 4.8: Integrated Intensity map of ^{12}CO in C20 (*white*) overlaid with extinction contours (*black*); ^{12}CO emission contours are from $10 - 90$ % in steps of 10 % with 100 % = 10.3 K km s^{-1}

Similar to B59 the ^{13}CO emission in Core 20 is very centrally concentrated but again peaks with intensity values of 2.8 K km s^{-1} below B59 which shows integrated intensities between 5.5 K km s^{-1} and 9.25 K km s^{-1} at corresponding extinction ranges. The Molecular Ring shows a broader scatter at $A_v \approx 14$ mag with integrated intensity values ranging between 4 K km s^{-1} and 7.6 K km s^{-1}.

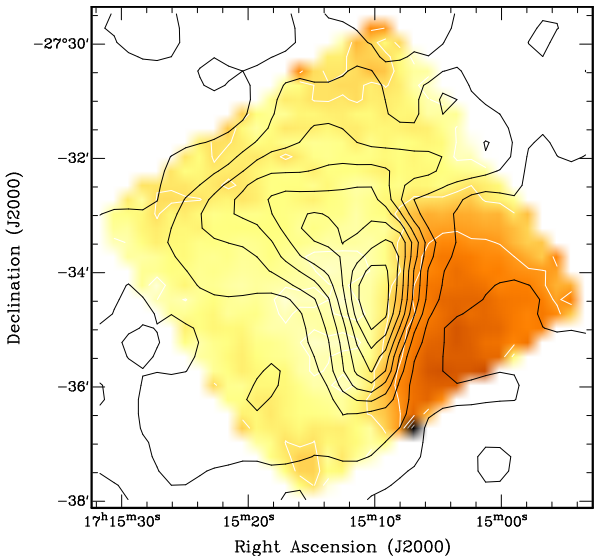

Figure 4.9: Integrated Intensity map of ^{13}CO in C20 (*white*) overlaid with extinction contours (*black*); ^{13}CO emission contours are from $10 - 90$ % in steps of 10 % with 100 % = 2.8 K km s^{-1}

The C^{18}O component of Core 20 (fig. 4.10) is with maximum integrated intensities of 0.46 K km s^{-1} at the extinction peak comparable to the other cores. B59 shows at $A_v \approx 14$ mag integrated intensities ranging between 0.67 K km s^{-1} and 1.16 K km s^{-1} and the Molecular Ring lies with 0.36 K km s^{-1} and 0.75 K km s^{-1} in a similar intensity range.

Although Core 20 is located so close to B59 there are big differences regarding extinction and emission properties. These differences will become more obvious in the further analyzing process and will be discussed in section 5.3.

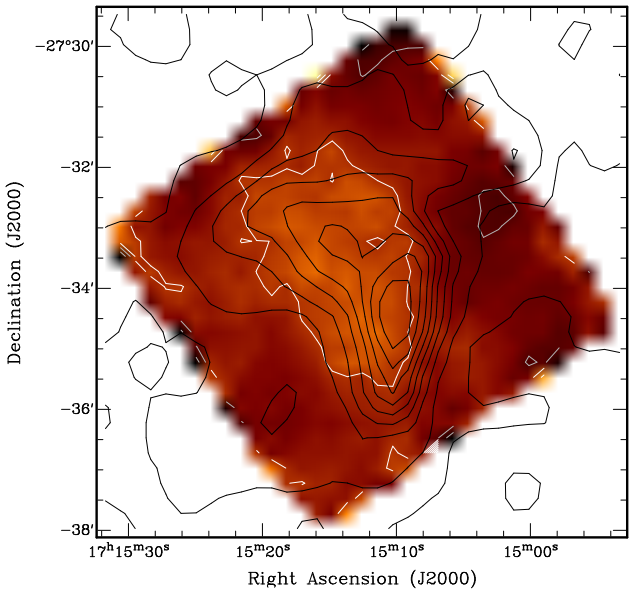

Figure 4.10: Integrated Intensity map of $C^{18}O$ in C20 (*white*) overlaid with extinction contours (*black*); $C^{18}C$ emission contours are from $10 - 90$ % in steps of 10 % with 100 % $= 2$ K km s^{-1}

Extinction and Emission Properties in the Molecular Ring (MR) The Molecular Ring is actually a larger structure lying in the *bowl* at the (south-)eastern end of the pipe nebula. Figure 3.3 shows the extinction map of the investigated area. In chapter 1.4 the classification of the Pipe's main features regarding to their kinematic features derived by Muench et al., 2007 was already described. Following Muench et al. the Bowl appears to be composed of gas from the two main velocity components (at 3 km s^{-1} and 5 km s^{-1}, respectively) forming a coherent ring-like structure. Muench found that core-to-core motions in the Ring are very large compared to the stem which is at least partially caused by the nature of v_{LSR} variations in the Ring. Similar ring-like structures of molecular gas were found in Taurus (Cernicharo & Guelin, 1987) which in contrast to the Pipe's Molecular Ring show strong star formation activity.

In the optical polarimetric survey of Alves et al., 2008 the Molecular Ring is described as being most probably of younger evolutionary age with the fragmentation process just starting. This was concluded by the increasing polarization level and parallel decreasing dispersion when moving along the Pipe's main axis toward the Molecular Ring. Catching up the hypothesis of differences in chemical evolution regarding to the evolutionary age of an extinction core first implemented by Frau et al., 2010 the following analysis may reveal differences in chemical abundances which could be

related to the relative ages of the investigated cores.

An in the literature repeatedly discussed structure is the globule FeSt 1-457 lying inside the Molecular Ring at approximately $17^h\ 35^m\ 70^s$ and $-25^\circ\ 30'$. The region of interest in the present work however lies in the great dark structure to the west at exactly $17^h\ 34^m\ 0^s$ to $17^h\ 34^m\ 40^s$ and $-25^\circ\ 40'$ to $-25^\circ\ 54'$.

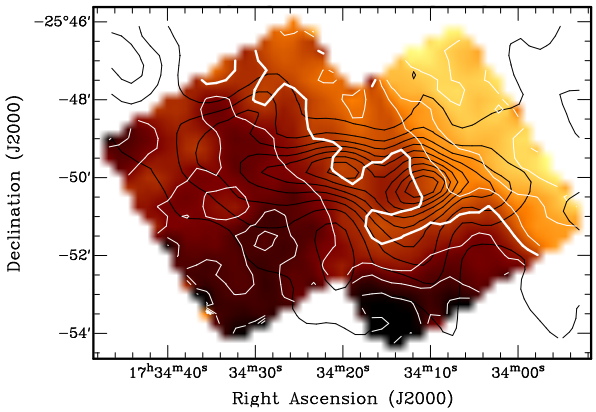

Figure 4.11: Integrated Intensity map of ^{12}CO in MR (*white*) overlaid with extinction contours (*black*); ^{12}CO emission contours are from $10 - 90$ % in steps of 10 % with 100 % = 25 K km s^{-1}

Like it was the case in B59 the ^{12}CO emission line in the Molecular Ring peaks again west to the core showing broader intensity ranges at lower extinction. Maximum integrated intensities reach values of ~ 24 K km s^{-1}. Toward the extinction peak the radiation is decreasing down to integrated intensities of 21.5 K km s^{-1} at $A_v \approx 45$ mag. In comparison B59 reaches only integrated intensities of maximal 18 K km s^{-1} at corresponding extinction values.

Figure 4.12 shows the integrated intensity map of the ^{13}CO component over plotted with extinction contours. The radiation is distributed over the whole map arising to both sides of the core. The emission is decreasing toward the center with broad intensity ranges at lower extinction values. Maximum integrated intensities were found to be 7.8 K km s^{-1} whereas at the extinction peak values of 5.6 K km s^{-1} were measured. In B59 the ^{13}CO emission at $A_v = 45$ mag is distributed between 6.8 K km s^{-1} and 9.3 K km s^{-1} and therefore somewhat higher than in the Molecular Ring.

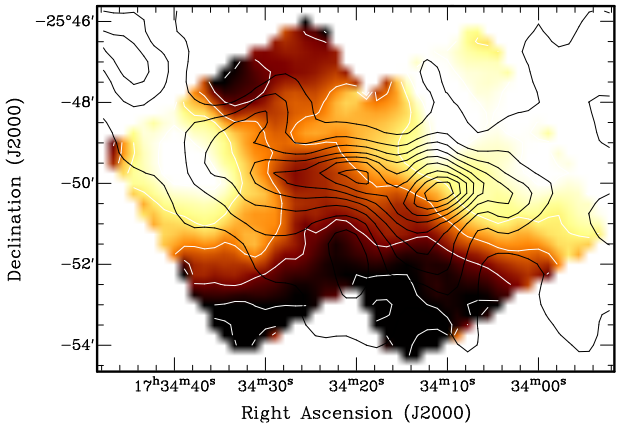

Figure 4.12: Integrated Intensity map of ^{13}CO in MR (*white*) overlaid with extinction contours (*black*); ^{13}CO emission contours are from $10 - 90$ % in steps of 15 % with $100\ \% = 7.8\ K\ \mathrm{km\ s^{-1}}$

In figure 4.13 the $C^{18}O$ component of the Molecular Ring is shown which spans a larger region than compared to the other two cores. The emission peaks with $0.8\ \mathrm{K\ km\ s^{-1}}$ at two maxima located at $\alpha = 17^h\ 34^m\ 27^s$, $\delta = -25°\ 50'\ 30''$ and at $\alpha = 17^h\ 34^m\ 02^s$, $\delta = -25°\ 50'\ 34''$. The intensity is decreasing toward the extinction center by $\sim 0.4\ \mathrm{K\ km\ s^{-1}}$ reaching values of $0.53\ \mathrm{K\ km\ s^{-1}}$ at $A_v \approx 44$ mag. In comparison B59 showed intensities varying between $1.2\ \mathrm{K\ km\ s^{-1}}$ and $1.5\ \mathrm{K\ km\ s^{-1}}$ at corresponding extinction ranges.

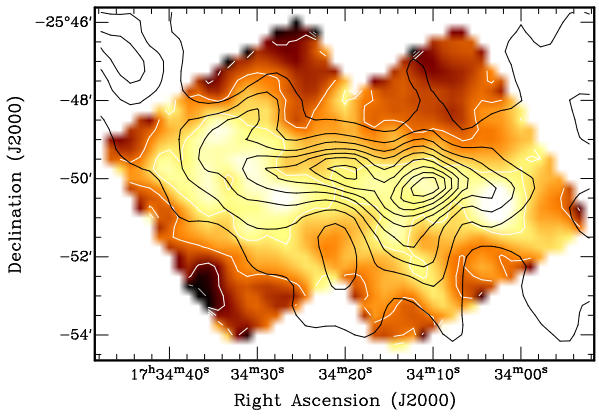

Figure 4.13: Integrated Intensity map of $C^{18}O$ in MR (*white*) overlaid with extinction contours (*black*); $C^{18}O$ emission contours are from $10 - 90$ % in steps of 15 % with $100\ \% = 0.9\ K\ \mathrm{km\ s^{-1}}$

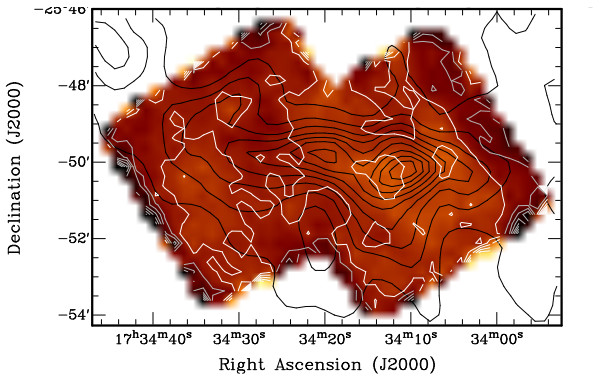

Figure 4.14: Integrated Intensity map of HCN in MR (*white*) overlaid with extinction contours (*black*); HCN emission contours are from $10 - 90$ % in steps of 5 % with $100\ \% = 3.6\ \mathrm{K\ km\ s^{-1}}$

When moving on to high density tracer abundance profiles significant differences to B59 show up. Only HNC and N_2H^+ were detected significantly above a threshold of $\frac{S}{N} > 3$, the remaining species were listed as non-detections.

Although HCN and HNC are thought to have the same formation origin and to be produced with the same probability (Sarrasin et al., 2009) large variations in the ratio of both isomers are reported in the literature. From thermochemical considerations HNC is less stable than HCN. Loison et al. 2014 pointed out that if both of them are formed in thermal equilibrium conditions HNC should be negligible abundant, but the contrary is the case. For this reason interstellar abundance ratios in general are given as $\frac{\mathrm{HNC}}{\mathrm{HCN}}$ which is found to vary between $\sim \frac{1}{80}$ for high star forming regions like OMC-I (Schilke et al., 1982) to values of $1 - 4.5$ for dense molecular clouds (Hirota et al., 1998). Figures 4.14 and 4.15 show the integrated intensity maps of HCN and HNC in the Molecular Ring. As HCN was only detected below the 3-σ threshold criterion the resulting abundance ratio should be interpreted as an upper limit (see p. 118 for further description) and scales to $\frac{\mathrm{HNC}}{\mathrm{HCN}} < 3.5$ at the extinction peak whereas B59 shows with $\frac{\mathrm{HNC}}{\mathrm{HCN}} = 1.4$ a somewhat smaller value. This fact corresponds to the observed lower values in star forming regions reported in the literature (Schilke et al., 1982).

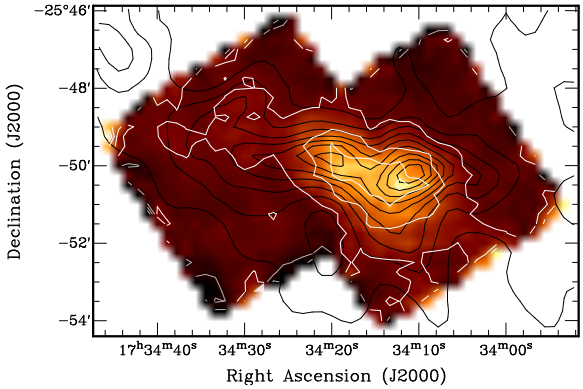

Figure 4.15: Integrated Intensity map of HNC in MR (*white*) overlaid with extinction contours (*black*); HNC emission contours are from $10 - 90$ % in steps of 10 % with 100 % $= 2.6$ K km s^{-1}

In the Molecular Ring HNC reaches maximal intensities of 0.68 K km s^{-1} at the extinction peak lying at $A_v = 44$ mag whereas in B59 slightly higher values varying between 0.6 and 0.9 K km s^{-1} are reached at these extinction ranges.

Figure 4.16 presents the integrated emission map of N_2H^+ in the Molecular Ring with peak intensities of ~ 0.7 K km s^{-1} at $A_v = 44$ mag. At comparable extinction values in B59 N_2H^+ shows considerable scatter with varying intensities between 0.67 and 1.9 K km s^{-1}.

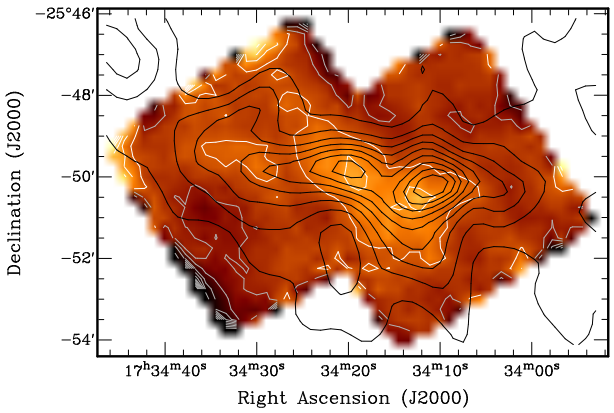

Figure 4.16: Integrated Intensity map of N_2H^+ in MR (*white*) overlaid with extinction contours (*black*); N_2H^+ emission contours are from $10 - 90$ % in steps of 5 % with 100 % $= 3.1$ K km s^{-1}

4.2 Summary

Karma/kvis is a very useful tool to get a general optical impression of the data. The `movie` function allows users to browse through the cube so one is able to determine the variations in emission behavior from frame to frame. It is easy to define the emitting regions by use of the `map` button as color scales and intensities can be adjusted by the user himself. Maybe the most noticeable function is to extract the spectra of the single pixels directly from each frame. This way one can quickly get a general impression of variations in line emission behavior throughout the whole spectrum.

For comparison integrated intensity maps of the observed molecular transitions were used together with the corresponding extinction map. When over-plotted with the contours of the corresponding extinction map the different density dependent radiation behavior of the observed molecules becomes apparent. B59 shows in consequence of its high extinction properties also the highest intensities in molecular emission. But it is to mention that at values corresponding to the Molecular Ring's extinction peak ^{12}CO emission in B59 is 3.5 K km s^{-1} less. Core 20 possesses peak extinction values of 14.4 mag and displays in general lower intensity values. The differences to B59 and the Molecular Ring at comparable extinction ranges are 2.8 K km s^{-1} and 1.3 K km s^{-1}, respectively. In contrast to the other cores the ^{12}CO emission in Core 20 appears more centrally concentrated which is most likely due to the lower peak extinction values. Like in B59 ^{12}CO emission in the Molecular Ring is found to origin west of the core with declining intensities toward the center (see table 4.2) whereas the ^{13}CO and C^{18}O component are showing two emission peaks west and east of the core with C^{18}O being more centrally concentrated. A central distribution for C^{18}O is found in all sample cores which results from the different optical properties of the CO isotopologues. The more abundant a molecule, the earlier its emission gets re-absorbed by the high particle density. As ^{13}CO and C^{18}O are less abundant than ^{12}CO higher extinction ranges can be traced before the emission gets optically thick. In chapter 5 the different optical properties of the CO components are investigated and discussed in detail.

All observed high density tracers in B59 were found to lie above the detection threshold of $\frac{S}{N} > 3\ \sigma$. As it was to expect the emission was found to be strongly centrally concentrated with N_2H^+ showing the highest intensity values of 1.90 K km s^{-1} at the extinction peak followed by HNC with 1.20 K km s^{-1} and HCN with 0.86 K km s^{-1}. The same radiation behavior is found in the Molecular Ring except of the fact that only N_2H^+ and HNC lie above the detection threshold with all remaining high density species being listed as non detected ($\frac{S}{N} < 3\ \sigma$). Table 4.2 provides an overview of measured intensities at the extinction peak compared with measured maximum intensities for the molecular species. In some cases the peak intensity is correlated as

Molecule	**B59** Int. $\left[\mathrm{K\ km\ s^{-1}}\right]$	**C20** Int. $\left[\mathrm{K\ km\ s^{-1}}\right]$	**Mol. Ring** Int. $\left[\mathrm{K\ km\ s^{-1}}\right]$
^{12}CO	13.00 (21.02)	6.00 (7.15)	21.15 (24.2)
^{13}CO	8.01 (9.80)	2.60 (2.80)	6.16 (7.80)
$C^{18}O$	1.72 (1.72)	0.46 (0.46)	0.53 (0.90)
HCN	0.86 (0.90)	-	0.20 (0.58)
$H^{13}CN$	0.22 (0.41)	-	0.09 (0.34)
HNC	1.20 (1.20)	-	0.70 (2.60)
HCO^+	0.95 (1.16)	-	0.007 (0.09)
$H^{13}CO^+$	0.70 (0.70)	-	0.09 (0.36)
N_2H^+	1.90 (2.52)	-	0.70 (0.72)

Table 4.2: Integrated intensities at the extinction peak per beam and maximum measured integrated intensities in brackets ( )

it is the case for $C^{18}O$ or for some high density tracers. Position information for the listed maximum intensities is given in table 4.3 in right ascension and declination. For completeness also the calculated error to the fit (see section 4.4) is displayed.

Molecule	**B59**	**C20**	**Mol. Ring**
^{12}CO	$\alpha = 17^h\ 11^m\ 11.045^s$	$\alpha = 17^h\ 15^m\ 13.664^s$	$\alpha = 17^h\ 34^m\ 07.650^s$
	$\delta = -27°\ 25'\ 05.16''$	$\delta = -27°\ 31'\ 58.19''$	$\delta = -25°\ 47'\ 59.77''$
err.	0.56808 K km s^{-1}	0.18794 K km s^{-1}	0.18499 K km s^{-1}
^{13}CO	$\alpha = 17^h\ 11^m\ 20.072^s$	$\alpha = 17^h\ 15^m\ 12.575^s$	$\alpha = 17^h\ 34^m\ 10.086^s$
	$\delta = -27°\ 24'\ 54.49''$	$\delta = -27°\ 34'\ 28.04''$	$\delta = -25°\ 47'\ 46.16''$
err.	0.05960 K km s^{-1}	0.07763 K km s^{-1}	0.10972 K km s^{-1}
C^{18}O	$\alpha = 17^h\ 11^m\ 24.338^s$	$\alpha = 17^h\ 15^m\ 11.392^s$	$\alpha = 17^h\ 34^m\ 02.188^s$
	$\delta = -27°\ 26'\ 13.05''$	$\delta = -27°\ 34'\ 43.78''$	$\delta = -25°\ 50'\ 30.61''$
err.	0.04868 K km s^{-1}	0.06505 K km s^{-1}	0.04006 K km s^{-1}
HCN	$\alpha = 17^h\ 11^m\ 22.207^s$	-	$\alpha = 17^h\ 34^m\ 35.242^s$
	$\delta = -27°\ 26'\ 14.24''$	-	$\delta = -25°\ 50'\ 36.66''$
err.	0.04771 K km s^{-1}	-	0.02775 K km s^{-1}
$H^{13}CN$	$\alpha = 17^h\ 11^m\ 28.007^s$	-	$\alpha = 17^h\ 34^m\ 26.146^s$
	$\delta = -27°\ 26'\ 14.69''$	-	$\delta = -25°\ 49'\ 31.59''$
err.	0.27216 K km s^{-1}	-	0.10291 K km s^{-1}
HNC	$\alpha = 17^h\ 11^m\ 24.507^s$	-	$\alpha = 17^h\ 34^m\ 12.335^s$
	$\delta = -27°\ 26'\ 15.33''$	-	$\delta = -25°\ 50'\ 30.62''$
err.	0.02597 K km s^{-1}	-	0.02775 K km s^{-1}
HCO^+	$\alpha = 17^h\ 11^m\ 19.991^s$	-	$\alpha = 17^h\ 34^m\ 18.644^s$
	$\delta = -27°\ 25'\ 14.12''$	-	$\delta = -25°\ 48'\ 48.38''$
err.	0.02024 K km s^{-1}	-	0.10376 K km s^{-1}
$H^{13}CO^+$	$\alpha = 17^h\ 11^m\ 24.412^s$	-	$\alpha = 17^h\ 34^m\ 11.233^s$
	$\delta = -27°\ 26'\ 17.85'$	-	$\delta = -25°\ 50'\ 36.62''$
err.	0.02082 K km s^{-1}	-	0.04588 K km s^{-1}
N_2H^+	$\alpha = 17^h\ 11^m\ 20.061^s$	-	$\alpha = 17^h\ 34^m\ 12.251^s$
	$\delta = -27°\ 26'\ 15.96''$	-	$\delta = -25°\ 50'\ 29.49''$
err.	0.00580 K km s^{-1}	-	0.00933 K km s^{-1}

Table 4.3: Position information of listed maximum intensity values of table 4.1 in right ascension (α) and declination δ with calculated error to the fit in $\left[\text{K km s}^{-1}\right]$

4.3 Parameter Measuring with Gildas/CLASS

Gildas is the reduction and analysis software of the IRAM 30 m telescope. The CLASS software package is used for reducing spectroscopic data obtained on a single-dish telescope. The name CLASS stands for *Continuum and Line Analysis Single-dish Software*. On the IRAM homepage www.iram.fr/IRAMFR/GILDAS/ one finds detailed installation instructions and a software documentation. CLASS is very useful to handle large data sets and is able to extract spectral parameters even on condition of selection criteria for individual parameters. After a standard installation class should be able to start directly from the terminal by just typing `class`. The commands are to type into the terminal window while the spectra are displayed in the GREG graphic window which opens as CLASS starts.

Before importing the spectral cubes have to be converted to the Gildas data format *lmv*. This can be done by the following command structure

```
file out B59_12co.lmv single

lmv B59_12co_map.fits

file in B59_12co.lmv
```

The command `file in B59_12co.lmv` sets the given file as input file. With typing `find /all` a list with all the spectra contained in the input file is created. Now one can call individual spectra by the command `get *spectrum number*`. The commands `get first` or `get next` call the first or the next frame according to the displayed spectrum.

Unfortunately we lost the astrometric information contained in the file header during the import process. As a consequence the position information in the spectra is given as offset in right ascension and declination. Figure 4.17 shows an example spectrum of the ^{12}CO component in B59 located at the emission peak. The offsets in B59 were very large as can be seen in the header of fig. 4.17. Normally such a shifting can be calculated on the basis of trigonometry. Therefore the cosinus of the given declination must be multiplied by the given offset in right ascension before adding the offsets to their associated equatorial positions. Unfortunately the offset position of B59 was located too far away ($\lambda = -1.8 \times 10^4, \beta = -6 \times 10^3$) and created image distortions which altered the calculated positions. As a solution to the problem the original astrometry was reconstructed by comparison with the astronomical imaging software SAOImage DS9. The procedure will be explained later in the text when discussing the automatized data extraction. Beforehand it is of importance how to display the spectral information in different implementations. To force class to display the data in dependence of velocity instead of frequency one needs the command

```
set unit v
```

By using this the x-axis will be transformed to $[\frac{km}{s}]$ whereas the frequencies information (in MHz) is shifted to the upper border (see fig. 4.17).

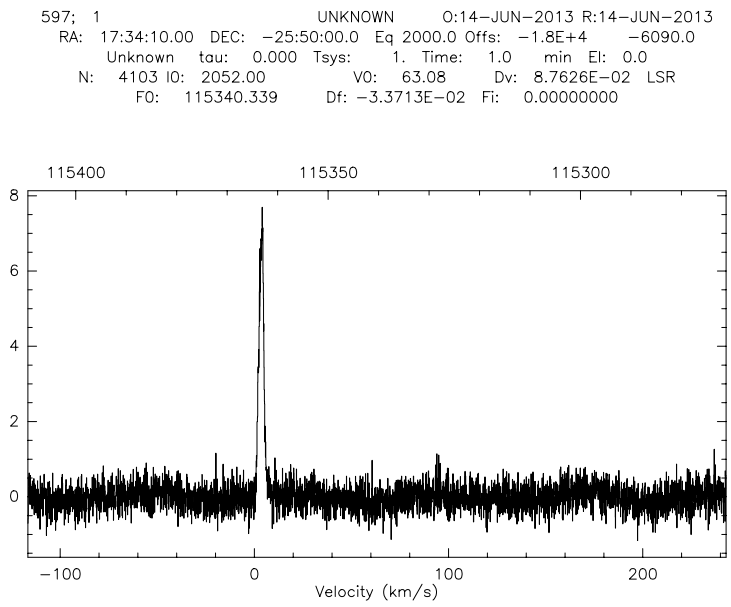

Figure 4.17: Example spectrum derived for ^{12}CO line emission in B59. The Y-axes gives measured line intensity in K, whereas the horizontal axes show velocity and frequency range in km s^{-1} and MHz, respectively.

Figure 4.18 shows a map of the B59 core build up from the single spectra of each individual pixel. The positions in space are given by offsets. To obtain such a spectral map one first need to define the axis to fixed ranges which is done by the following text commands:

```
set mode x -25 25

set mode y -1 9

map /grid
```

The `map /grid` command opens the map. Now the `zoom` or the `popup` command can be used for a closer examination. `zoom` allows the user to define a zoom window which would open by left mouse click in a new window showing a bigger display of

the selected spectra. The size of the zoom window can be adjusted by using the middle mouse button; the right button ends the zoom mode. Similar to this the `popup` command let pop up individual spectra selected by the middle mouse button.

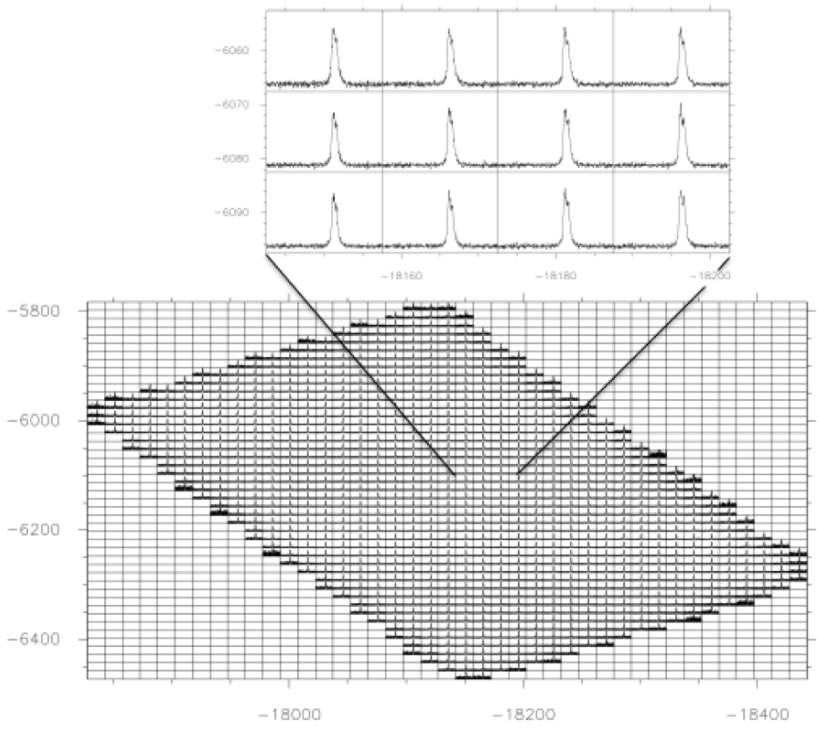

Figure 4.18: Spectral map consisting of single spectra in order to display line variations throughout the mapped region

In a third version the line emission can be displayed in form of integrated intensity maps in different color styles. Therefore the line emitting area is to define by its velocity range and the command

```
print area -5 10 /out B59_12co_IntArea.dat
```

calculates the integrated emission in the given velocity range and creates an output text file. In the case of the B59 ^{12}CO component a velocity range between -5 and 10 $[\frac{km}{s}]$ covers the line emitting area very well. Now we need to enter the graphic utility package GREG which is used to prepare data plots in CLASS. The GREG language can be called by inserting a `g\` in front of the command line. The next command uses the GREG mode to collate the data columns of the output file to the (X,Y,Z) vectors. As the first column includes the spectral number the second, third and fourth column refer to the position vectors.

```
g\col x 2 y 3 z 4 /file B59_12co_IntArea.dat
```

The next step is to interpolate between the data points. The `random` comment takes the (X,Y,Z) arrays to calculate the intensity in a regular grid of 700 $\times$ 750 points referring to the physical dimensions of the `map/grid` illustration. The term `bl 0` sets the blanking value to zero.

```
g\random 700 750 /bl0
```

With the next two commands the box size of the map in creation is set to the appropriate physical dimensions and fixed with `g\set box match`. The limits refer to the offset in right ascension and declination with a relative position of λ (-17800/-18500) and β (-6500/-5750), respectively.

```
g\lim -17800 -18500 -6500 -5750

g\set box match
```

Now everything is prepared to draw the image. With

```
g\set level 10 to 25 by 1
```

the contour ranges can be set to values referring to the measured intensities. These can be reviewed in the third column of the produced output file `B59_12co_IntArea.dat`. The chosen contour values are drawn by the command `g\rgm` whereas `g\rgm /g` fills the contours in grey color. Alternatively one can use the command `g\rgm /plot` to derive a colored picture. Different color modes are available which can be entered by setting `g\lut` to the wanted color table.

Figure 4.19 presents the integrated emission maps of the ^{12}CO component in B59. The image equals the integrated velocity map obtained by the moment zero map with karma/kvis in figure 4.3 but possesses a high resolution as the moment zero map is integrated over a broader range.

The last and most important step in CLASS was to extract the spectral data parameters into a text file for a further use in other plotting programs. This can be done by programming a loop which can be called by the @ symbol and which is running through the whole spectral cube extracting the wanted parameters out of every frame.

For this purpose a gauss function was fitted to the spectra as the gauss curve represents best the physical behavior of the line transition in local thermal equilibrium with the upper level population following a Boltzmann distribution. Mathematically

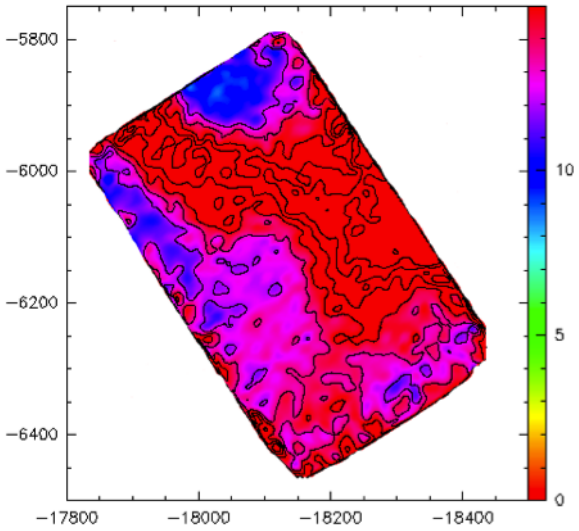

Figure 4.19: Integrated velocity map of the ^{12}CO component in B59 obtained with CLASS. Contour levels are from $10 - 25$ K km s^{-1} by steps of 1; X- and Y-axis correspond to the offset in right ascension and declination in units of arc seconds.

the Gauss function is described by applying the exponential function to a quadratic function. Thus the logarithm of a Gaussian is always a quadratic function.

Figure 4.20 shows an example of the Gauss function which is defined by:

$$f(x) = a \times exp\left(\frac{-(x-b)^2}{2c^2}\right) \tag{4.1}$$

The amplitude a gives the height of the curves peak, b corresponds to the position of the peak's center, and c as the standard deviation gives the curves width. c can be converted into FWHM with:

$$FWHM = 2\sqrt{2\ \log(2)}\ c = \sqrt{8\ \log(2)}c \quad \rightarrow \quad c = \frac{FWHM}{\sqrt{8\ \log(2)}} \tag{4.2}$$

The integral of the Gaussian gives the error function:

$$\int_{-\infty}^{\infty} e^{-x^2} \mathrm{d}x = \sqrt{\pi} \quad \rightarrow \quad \int_{-\infty}^{\infty} a\ e^{-\frac{(x-b)^2}{2c^2}} \mathrm{d}x = a\ c\ \sqrt{2\pi} \tag{4.3}$$

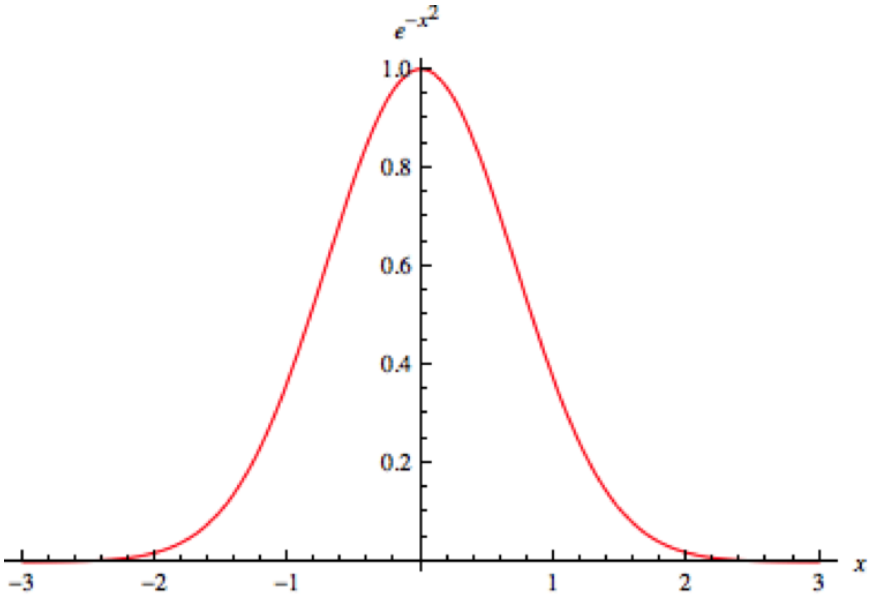

Figure 4.20: Gauss Function; Credit: http://mathworld.wolfram.com

Following line parameters were derived:

- Peak temperature ($Signal$)
- Integrated area under the emission line (Int)
- Signal to Noise ratio (S/N)
- FWHP linewidth (Δv)
- radial velocity (v_{LSR})
- spectral noise σ

The peak temperature corresponds to the peak of the Gaussian:

$$T_{peak} = \frac{\frac{Int}{\Delta v}}{\sqrt{\frac{2\pi}{8log(2)}}} \tag{4.4}$$

whereas the signal to noise value (S/N) is generated by dividing T_{peak} by the spectral continuum noise $sigma$:

$$S/N = \frac{T_{peak}}{\sigma} \tag{4.5}$$

Figure 4.21 illustrates a gauss fitted spectrum of ^{12}CO in B59. The chosen spectrum is one of the strongest lying directly at the emission peak. Two more parameters

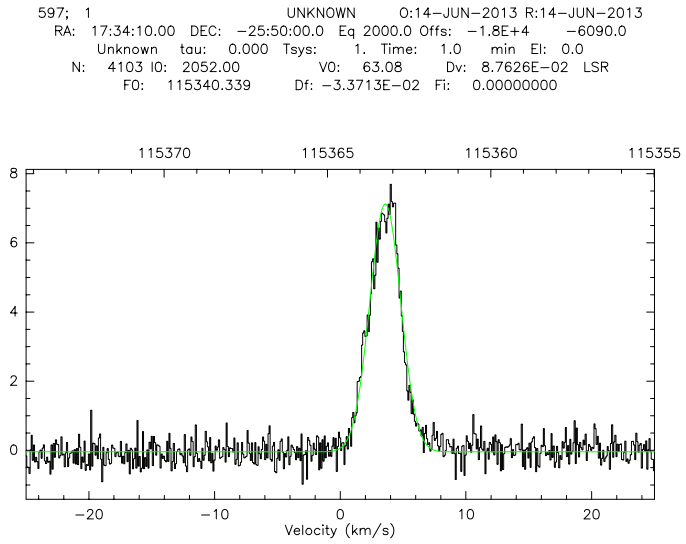

Figure 4.21: Example plot of a gauss-fitted ^{12}CO emission line originating out of the B59 extinction peak

which had to be calculated manually are the physical pixel coordinates. These are synonymous with the display in other software programs and are needed to compare the spectral parameters with for example extinction or temperature maps. The physical coordinates can be equalized as long as the comparison maps have the same pixel astrometry. In the header of the fits cube the pixel coordinates are directly linked to the equatorial position in the sky.

Unfortunately in CLASS the output of the spectral data was given in the form of offsets in equatorial coordinates and a reference position. Like mentioned beforehand the reference position was far away of the observing field and therefore the offsets very high. As a consequence a direct calculation of the real equatorial coordinates was affected by image distortion effects. To solve the problem a formula was applied into the class loop which calculates the physical pixel coordinates by setting a linear relation to the offset coordinates.

For the calculation the astronomical imaging software SAOImage DS9 was used additionally as it displays the equatorial and physical coordinates of the individual pixels. The illustration of the integrated ^{12}CO *mom*0 emission in DS9 and of the spectral map of ^{12}CO generated by `map /grid` in CLASS have exactly the same pixel astrometry. So the two illustrations could be treated like two planes in the sky showing the same picture but shifted in their X- and Y- coordinates. This way a simple linear

equation allows the conversation from offset to pixel coordinates:

$$x_{ds9} = x_{class} \times k + d \quad \text{and} \quad y_{ds9} = y_{class} \times k + d \tag{4.6}$$

By calculating (4.6) for two pixels in X and two pixels in Y one can determine the parameters k and d. In the case of B59 these showed to be:

$$k_x = -0.066785 \quad \text{and} \quad d_x = -1189.1 \tag{4.7}$$

$$k_y = +0.06705 \quad \text{and} \quad d_y = +435.2416 \tag{4.8}$$

With this in hand the loop to process the gauss fit through all the spectra of the cube can be created. This can be simply done in a text file where all important line commands are included such that a simple call of `@12co_gauss_loop.txt` directly after starting class would be enough. In the following an example of a gauss loop created for ^{12}CO will be presented with a subsequent discussion of the individual command lines.

```
file in B59_12co.lmv
find /all
set unit v
define real s_n
define real x_ds
define real y_ds
define real summe
define real sigma_12co

sic out "12co_finished.dat"

set window 0 10
method gauss
for i 1 to found
get next
base 0

fit\lines 1 "0 6.5 1 3.6 0 2" /nocursor
  fit\minimize
  fit\iterate
  fit\vis
```

```
s_n = r%head%gau%nfit[1]/r%head%gau%nfit[3]/1.064467/sigma
x_ds = -0.066785*off_lambda-1189.1
y_ds = 0.06705*off_beta+435.2416
sigma_12co = sqrt(0.262878*10)*sigma

!if s_n.gt.3
Compute summe sum ry[1345:1395]

say  'x_ds'  'y_ds' 'r%head%gau%nfit[1]' 's_n' 'r%head%gau%nfit[3]'
     'sigma_12co'

!endif
next i

sic out
```

The first section in the loop includes the call of the file `B59_12co.lmv`, the loading of the listed spectra with `find /all` and the setting of the X-axis to km s^{-1} by `set unit v`. Afterwards five *real* variables are defined for calculating S/N, physical coordinates and the error of the integrated area. The variable called `summe` summarizes the line emitting area in purpose to compare afterwards with that measured in the gauss fits. The last command `sic out "12co_finished.dat"` defines the output file.

In the next section the gauss loop is prepared by setting a limiting velocity range to the fit (`set window 0 10`). Outside this spectral window just the spectral noise is measured. The method *gauss* is announced and a for loop created which repeats the procedure for every spectrum with index *i* from the first to all found. The command `get next` spins the for loop through the spectra. It is closed with `next i` at the end of the loop. The `base 0` command subtracts the baseline of the spectrum as a polynomial of zeroth grade. This would not be really necessary as the spectra were already base line subtracted but the program demands a base line subtraction in order to set a gauss fit.

The fit is initiated by the number of lines one wants to fit. This can be up to a maximum of 5. Each line is indicated by double quotes (" ") and contains three parameters together with a fixing parameter. In the gauss mode the three parameters represent temperature (T_{peak}), position (v_{LSR}) and line width (Δv). For each of them one must decide if the parameter should be fixed or adjustable. With this possibility one can

force the gauss fit to restricted parameters by positioning a 0 or a 1 before the respective parameter. As in the case of ^{12}CO the position of the line emitting velocity range is fixed to be 3.6 $\frac{km}{s}$ which is declared by a 1 beforehand, whereas temperature and line width are predetermined to be in the order of 6.5 K and 2 $\frac{km}{s}$ but adjustable, declared by 0. The command `min` minimizes a gaussian function to the best fit of the line profile. The command `iter` repeats the iteration process. It is not necessary to make the fit visible when processing through the cube but if wanted one can achieve this with the command `vis`.

The remaining code consists of the calculation of the variables `s_n, x_ds, y_ds, sigma_12co` which represent the signal to noise ratio, the physical coordinates calculated with the use of DS9, and the calculated spectral noise within the integration area. Additionally a small *if loop* offers the possibility to select only data points with an S/N value greater than three. The call signs indicate that these commands are excluded and read as text comments. The lines in between the excluded comments are not affected. With `Compute summe sum ry[1345:1395]` the area of the manually selected spectral channels corresponding to the line emitting velocity range is summarized. This was done in caution to test the accuracy of the results derived with the gauss method. When everything has worked out fine the two outputs should be linear related. In the case of more complicated fits, as it was required for species which show hyperfine structure splitting in their line profiles (see below), this method was very useful to optimize the accuracy of the fits. The spectral noise within the integration area is calculated as the square root of the spectral resolution $\Delta\ v$ in km s^{-1} times the width of the integrated area in km s^{-1} (w). This is further multiplied with the spectral noise σ calculated outside the integration field:

$$sigma_{12co} = \sqrt{\Delta v\ w}\ \sigma \tag{4.9}$$

At the end of the loop the command `say` defines the parameters to write into the output file. It is important not to forget `sic out` as the last command, otherwise the output file would not be created. The created output file with name `12co_finished.dat` includes data columns representing the parameters listed in the `say` command. The two variables named `r%head%gau%nfit[1]` and `r%head%gau%nfit[3]` refer to the fit results of the area under the gauss curve and the FWHP line width, respectively. The parameter `sigma_12co` represents the calculated noise of the fit.

As shortly mentioned above some of the molecules show hyperfine structure splitting in their line profiles. This was the case for HCN, H^{13}CN and N_2H^+. Additional quantum mechanical interaction processes cause the atomic energy levels to split up which leads to line splitting in the spectrum. The spectral line splitting corresponds to

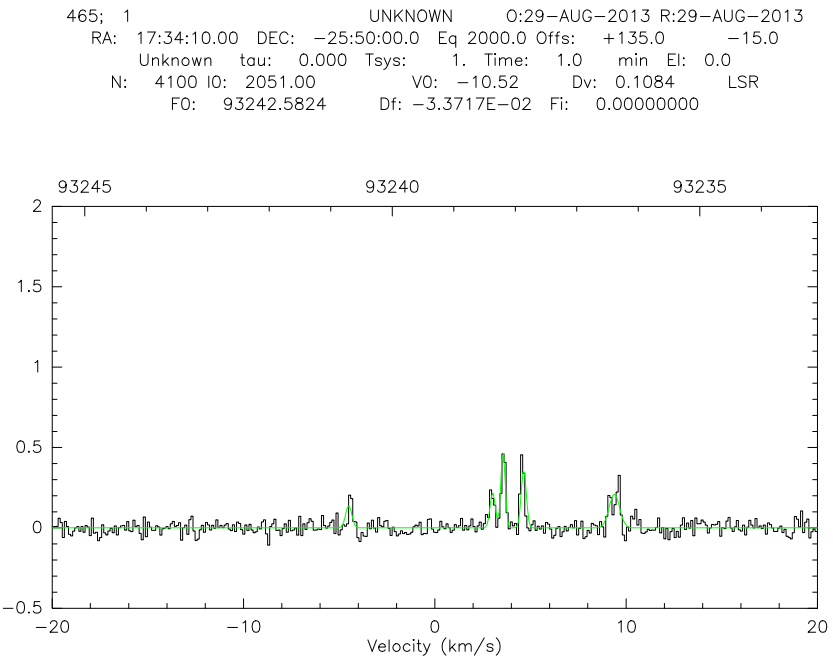

Figure 4.22: Hyperfine structure fit for N_2H^+ in the Molecular Ring

the distance between the atomic energy levels which are in the case of fine structure splitting approximately about a factor of 10^{-5} smaller. Reason for this is the interaction between the magnetic moment of the nucleus in the rest frame of the electron (caused by the nucleus' charge) and the magnetic moment of the electron caused by its spin. Due to its orbital motion the electron encounters a magnetic field originating from the apparent motion of the charged nucleus at the electron's position. The magnetic momentum of this field (L) couples to the magnetic momentum of the electron-spin (S) leading to a new total orbital momentum J

$$J = L + S \tag{4.10}$$

Under very high resolutions fine structure line profiles are found to split further into hyper fine structures which are again about a factor of 10^{-3} smaller. The effect is caused by the angular momentum of the nucleus, the nuclear spin (I) which is about a factor of 10^{-3} smaller than the angular momentum of the electron shell. The coupling of these both results in a quantized total angular momentum (F) corresponding to the sum of nuclear spin and total orbital momentum:

$$F = I + J \tag{4.11}$$

With regard to the Fermi-Dirac statistics F can only take half-integral values be-

tween $|F - J|$ and $F + J$.

Figure 4.22 shows an example of a hyperfine structure fit for N_2H^+ in B59. CLASS provides a fitting method especially for fitting molecular hyperfine structure lines which is focused on the line emitting behavior of ammonia (NH_3). Since this routine is using Gaussians we kept the old fitting procedure. In the case of HCN and $H^{13}CN$ the line profile splits into three hyperfine structure components. N_2H^+ shows seven discrete hyperfine components in its first transition which partly lie so close to each other that they could not be resolved individually.

Wavelength and frequency of an electromagnetic wave are connected by its propagation velocity. Thus, frequency multiplied with wavelength gives always the speed of light. As the universe is expanding any observed emission is Doppler-shifted relative to us. For non-relativistic velocities the Doppler shift is defined as

$$f = f_0(1 + \frac{v}{c}) \tag{4.12}$$

with c the speed of light, f the frequency, and f_0 as the rest frequency of the molecule. With knowledge of f_0 one can determine the relative velocity of the observed object by measuring the sky frequency. Optical and radio astronomers have different approaches to do that as in optics rather wavelength shifts are measured while radio astronomers observe shifts in frequency.

To calculate the appropriate velocities for hyperfine components the formula for conversion into radio velocity was used:

$$v_{radio} = c \ [1 - \frac{f}{f_0}] \tag{4.13}$$

The frequencies of rest corresponding to the hyperfine components were taken from the Leiden atomic and molecular database, an online catalogue of atomic and molecular spectroscopy databases. In table 4.4 the frequencies for the N_2H^+ satellite components are listed. These were to convert into radio velocities corresponding to the observed Doppler shift toward the Pipe nebula. Therefore the source velocity was set to zero and relative velocities were calculated. These were shifted to v_{LSR} of the Pipe nebula by adding the measured average velocity of the respective core. This way they were shifted to the observed positions in the molecular core and could easily be determined in the fit. As some hyperfine structure transitions in N_2H^+ lie very close to each other a fit applied to five transition lines sufficed to cover the line emitting area accurately. The derived integrated intensities were summarized as each hyper fine structure component contributes to the total energy of the transition. For the error of the fits in the single components the standard deviation was calculated for each spectrum which is shown as error bars in the corresponding plots of intensity versus

frequency	calculated velocity	relative velocity	shifted velocity
93.1716081	7.082 km s^{-1}	6.936 km s^{-1}	9.635 km s^{-1}
93.1719049	6.127 km s^{-1}	5.981 km s^{-1}	8.681 km s^{-1}
93.1720398	5.693 km s^{-1}	5.547 km s^{-1}	8.246 km s^{-1}
93.1734669	1.101 km s^{-1}	0.955 km s^{-1}	3.654 km s^{-1}
93.1737637	0.146 km s^{-1}	0.000 km s^{-1}	2.700 km s^{-1}
93.1739540	- 0.467 km s^{-1}	- 0.612 km s^{-1}	2.088 km s^{-1}
93.1762522	-7.861 km s^{-1}	-8.007 km s^{-1}	-5.307 km s^{-1}

Table 4.4: Frequencies and calculated velocities of hyperfine structure components in the J 1 $\rightarrow$ 0 transition of N_2H^+

extinction in chapter 5.

Like mentioned beforehand the fit results were tested against the values obtained by summarizing over the whole line emitting area. In the case of the fine structure fits several runs were necessary until both results behaved similar in a linear plot. In order to achieve such a satisfactory agreement spectra out of line were examined and fit properties were altered until the scatter around the line was reduced to a minimum. Figure 4.23 resembles the final plot in a series of fitting attempts of the N_2H^+ molecule. The molecular data sets must behave like the points in this scatter plot or better to be accepted for further treatment.

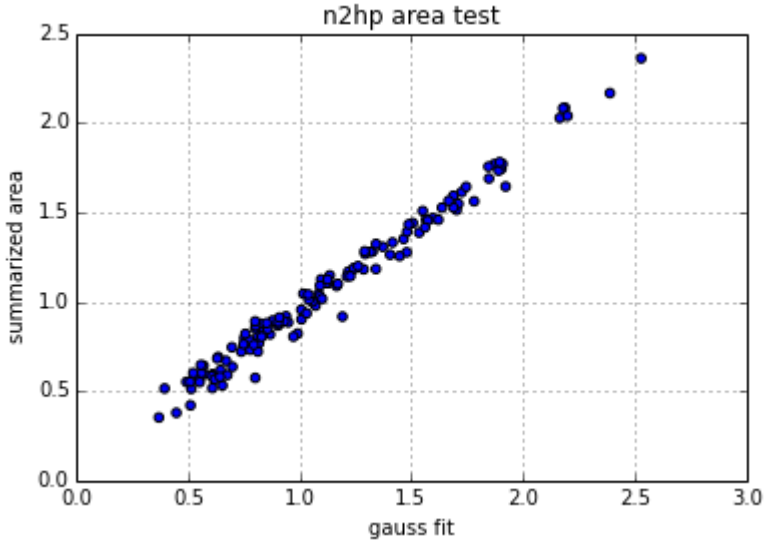

Figure 4.23: Example test plot of accordance between the results of summarized and gauss-fitted line measurements

This process was repeated for every transition line in the molecular core sample. The obtained text files were further used to investigate the different parameter dependencies and variations throughout the sample. In the next section the process of obtaining significant results by the use of IPython Notebook - a web-based interactive computing program - will be explained in detail. Afterwards the last two chapters present a summary of all significant results and a detailed discussion.

4.4 Plotting with Ipython Notebook

IPython Notebook is an advancement of the programming language Python produced in the late 1980s. The advantage is a web-based interface which supports code, mathematical expressions and inline plots. The online created notebooks are saved as *.ipynb* documents which can be easily shared and operated from different computers. To facilitate the sharing properties a general installation package for IPython was developed (Anaconda) which includes multiple packages and libraries. After installation the software can be started from the terminal by typing `ipython notebook`. Referring to the folder IPython is started from a dashboard will open which allows the user to create as many notebooks as wanted. By additionally setting the extension `-- script` when starting IPython, the Notebooks are not only saved in the .ipynb format but also as .py files readable in form of text files. The code sections partially included in this chapter were obtained in that way.

Very important libraries to import when creating a new Notebook are:

- AplPy (astronomical plotting library)
- AstroPy (tools for astronomy & astrophysics)
- Matplotlib (2D plotting library)
- NumPy (provides basic numerical routines)
- SciPy (scientific calculator)

The code is structured into single cells executable individually *within* the code. The syntax can be built in fewer lines of code as is possible in other programming languages. Due to the direct compiling of every cell the results can be directly examined or altered. The main aim of the use of Python was to compare the spectral line data with extinction measurements. As extinction and molecular emission maps differed in resolution and astrometry it was necessary to adjust the maps to the same display. The astrometry can be easily equalized by using the Montage Wrapper package affiliated by Astropy. The adjustment of resolution requires some more steps which will be discussed in the text.

This section consists mainly of two parts illustrating the working process with Python software. The first will explain the adjustment of observational parameters to the same resolution and astrometry for a further comparison of the data. The second part will show the attainment of the different plots in order to achieve significant results worth of a more extensive discussion.

4.4.1 Parametrical Adjustment

The provided extinction maps were of a resolution of 20″ whereas the CO-isotopologue maps were resolved with 33″ and all others with 36″. This different spectral resolutions can be viewed as normal distribution functions of different scales. By the technique of Gaussian Image Blurring (or Smoothing) they can be converted into each other. As this process naturally works only toward worse resolution one gets rid of details but also of noise. The gaussian function is invariant to convolution which means the sum of two Gaussian functions will result in a Gaussian again. Therefore the extinction maps had to be convolved with a Gaussian function of certain FWHM to be of the same grid as the molecular maps. In IPython a filter using a gaussian shaped kernel is applied to the extinction maps. The kernel function is defined by its FWHM (Γ) which follows

$$\Gamma_k = \sqrt{\Gamma_{12co}^2 - \Gamma_{ext}^2} \tag{4.14}$$

The code starts with importing the gaussian filter and loading of the input data. Output cells are indicated by the < > symbols. In the first data block the different shapes of the original extinction map and integrated velocity map of ^{12}CO in B59 are displayed.

```
from scipy.ndimage import gaussian_filter

hdu_ext=fits.open("ext_map_B59.fits")[0]
hdu_12co=fits.open("B59_12co_mom0.fits")[0]
hdu_12co.data.shape
 <(1, 48, 43)>
hdu_ext.data.shape
 <(161, 239)>
```

The second data block defines the beam resolution of the input data in arc seconds and calculates the corresponding resolution in terms of the number of pixels within a beam. This is done via the velocity information included in the header (CDELT2) of the individual files.

```
beam_ext_arcsec = 20
beam_12co_arcsec = 33

beam_ext_pix = beam_ext_arcsec / 3600. / hdu_ext.header["CDELT2"]
beam_ext_pix
 <1.99999840000128>

beam_12co_pix = beam_12co_arcsec / 3600. / hdu_12co.header["CDELT2"]
beam_12co_pix
 <2.1999998997574446>
```

Now the kernel function to convolve with must be calculated. Therefore the different beam sizes in arc seconds are subtracted from each other like illustrated in equation (4.14). The division by `hdu_ext.header["CDELT2"]` evaluates the number of extinction map pixels within the kernel beam. From this finally the full wave half maximum of the kernel function (`sigma_kernel_pix`) can be expressed.

```
beam_kernel_arcsec = np.sqrt(beam_12co_arcsec**2 - beam_ext_arcsec**2)
beam_kernel_arcsec

 <26.248809496813376>

beam_kernel_pix = beam_kernel_arcsec / 3600. / hdu_ext.header["CDELT2"]
beam_kernel_pix    # resolution of kernel gauss function in number of
                     extinction map pixels

 <2.6248788497782574>

sigma_kernel_pix = beam_kernel_pix / (2 * np.sqrt(2 * np.log(2.)))
sigma_kernel_pix   # FWHM of kernel gauss function

 <1.1146834151158072>
```

With this the gaussian filter can already be applied. The corresponding function in the code is defined by the input data which should be convolved and the FWHM of the kernel gauss function to convolve with. The command `writeto` creates the new extinction map:

```
hdu_ext.data = gaussian_filter(hdu_ext.data, sigma_kernel_pix)
hdu_ext.writeto("ext_map_B59_12co_smooth.fits", clobber=True)
```

To finally adjust the pixel astrometry between the maps the montage wrapper package must be imported into IPython. With the two simple commands `get header` and `reproject` the adjustment is completed. The shapes of the data can be checked again by `filename.data.shape`.

```
import montage_wrapper as montage

montage.mGetHdr("B59_12co_mom0.fits", "header_12co.hdr")

montage.reproject("ext_map_B59_12co_smooth.fits",
                  "ext_map_B59_12co_repr.fits", "header_12co.hdr")
```

Both maps should now be in the same grid and if so the data sets are comparable to each other. With the `scatter` command the intensity and extinction properties of each pixel can be displayed (fig. 4.24).

```
figure(figsize=(6,6))

scatter(hdu_ext_repr.data.ravel(), hdu_12co.data[0,:,:].ravel(), s=15)
xlabel("extinction")
ylabel("12CO")
```

The integrated velocity information of the moment zero maps is suited to provide a first look at the data and how the molecular emission behaves throughout the core. A further processing made use of the complete spectral cube including the spectral line parameter lists read out in CLASS. One of the first priorities was to apply selection criteria to the molecular data which allow to sort out all insignificant or noisy data points. The procedure, including parts of the code, will be explained in the next subsection.

4.4.2 Data Processing - Plotting Possibilities in IPython Notebook

Basically for plotting in IPython Notebook is the import of Matplotlib, a 2D plotting library and its numerical mathematics extension NumPy. The present code includes also many tools of the Astropy library like for example `astropy.wcs` which enables the world coordinate system. With this and the apply FITS tool the moment zero maps can be displayed in their equatorial coordinates (4.25). The following code demonstrates how such an illustration can be achieved:

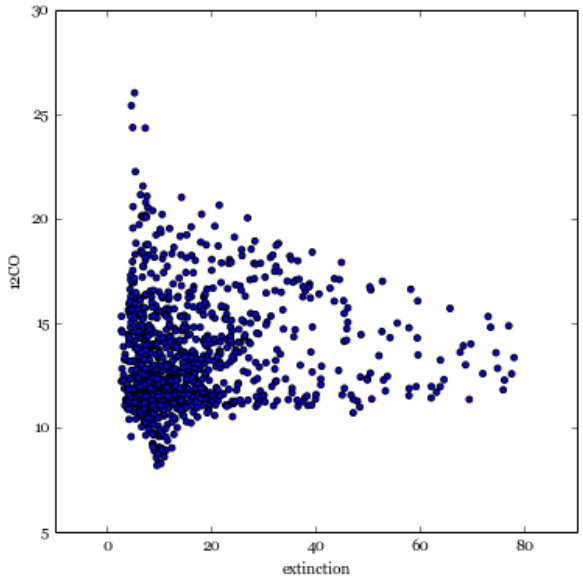

Figure 4.24: Plot of the ^{12}CO integrated intensity values of the moment zero map in B59 against extinction values

```
a=fits.open("B59_12co_map.fits")
fig=aplpy.FITSFigure("B59_12co_mom0.fits",dimensions=[1,0], slices=2000)
fig.show_colorscale(velocity integrated map of $^{12}$CO emission in B59)
```

For a closer examination of the molecular data not the integrated velocity maps but the whole spectral cubes were used. Based on the spectral parameters derived in CLASS and the reprojected and resolution adjusted extinction map the behavior of the different molecular species depending on the density structure of the core was investigated.

```
ext_data_12co=fits.open("ext_map_B59_12co_repr.fits")[0].data
mol_data_12co = ascii.read("12co_finished.dat")
```

In order to equalize the extinction map with the pixel positions in a cube the pixel coordinates first had to be converted to integers. This can be done by defining the input data and applying the `round` function. As the data output of the CLASS files is structured in columns the variables can be easily assigned to the column number.

```
x_ds_12co=mol_data_12co["col2"]
y_ds_12co=mol_data_12co["col3"]
```

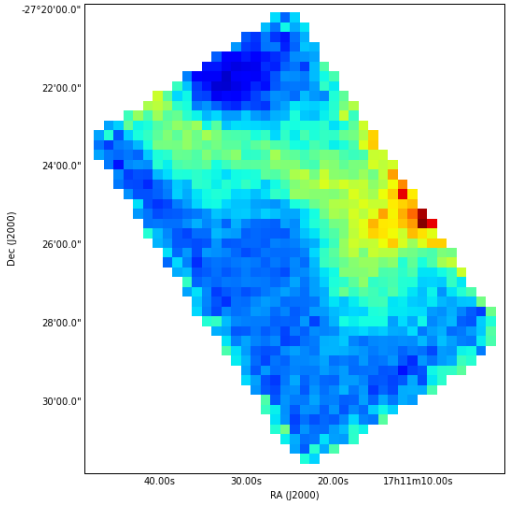

Figure 4.25: Moment Zero Map of ^{12}CO in B59 showing integrated intensities on a grid of equatorial coordinates

```
round2_12co =[int(round(n,0)) for n in x_ds_12co]
round3_12co =[int(round(n,0)) for n in y_ds_12co]
```

In the next step variables according to the listed spectral data had to be defined. These include x,y coordinates as well as the spectral index, integrated area (intensity), S/N values (`mol_z`), line widths, errors and calculated spectral noise. The latter were used to declare error bars and upper limits in the plots.

With the command `ext_values_12co=ext_data_12co[round3_12co,round2_12co]` the positions of molecular and extinction data can be equalized.

```
index_12co=mol_data_12co["col1"]
mol_x_12co=mol_data_12co["col2"]
mol_y_12co=mol_data_12co["col3"]
mol_z_12co=mol_data_12co["col4"]
mol_area_12co=mol_data_12co["col5"]
y_error_12co=mol_data_12co["col6"]
sigma_12co = mol_data_12co["col7"]


ext_values_12co=ext_data_12co[round3_12co,round2_12co]
```

Before the data sets could be finally plotted a selection criteria was introduced into the code to sort for data points with lower S/N values. This can be achieved by defin-

ing the whole data set as a list of arrays and applying a `for` loop to the data. In this way a result array is created which contains only the data points above a set selection criteria which in this case accorded to S/N values bigger than three. A second result vector was created to cope with marginal detections with an S/N value < 3. The variable `limit_12co` defines the upper limit as the triple of the calculated noise within the integration area. These values will be used in the following plots to represent detections below the $\frac{S}{N} > 3$ criterion in order to give upper limits for highest possible detections.

```
res_12co = np.array([[mol_x_12co[i] + 1,mol_y_12co[i] + 1,mol_z_12co[i],\
                      mol_area_12co[i],ext_values_12co[i],error_12co[i],\
                      sigma_12co[i],  index_12co[i]] for i in xrange
                      (len(mol_z_12co))  if mol_z_12co[i] > 3])

x = np.array(res_12co)
np.savetxt('res_12co>i_B59.txt', x)

res_12co_limits = np.array([[mol_x_12co[i] + 1,mol_y_12co[i] + 1,mol_z_12co[i],\
                      mol_area_12co[i],ext_values_12co[i], y_error_12co[i],\
                      sigma_12co[i], index_12co[i], sigma[i]] \
                      for i in xrange(len(mol_z_12co)) if mol_z_12co[i] < 3])
limit_12co = 3*res_12co_master_limits[:,7]
```

The commands `x = np.array(res_12co)` and `np.savetxt('res_12co>i_B59.txt', x)` create a new output file containing only the sorted data lists. The arguments of the result vector can be called by `res_12co[:,*]` with the asterisk referring to the individual argument which are counted starting from zero. The output data were again tested for authenticity as they should be comparable to the adjusted extinction and moment zero maps. As it turned out a display error has occurred originating from different dimensions between the moment zero maps and the appendant spectral cubes. The moment zero map included one additional row of pixels framing the spectral map. As in the beginning extinction maps were adjusted to moment zero maps (see 4.4.1) the equalization of the spectral data with extinction data resulted in a shift of $(-1, -1)$ for every pixel position. This effect was corrected by adding $+1$ in the final result vectors.

The following code cell gives an example referring to the plots treated in the next chapter. In this case the intensity versus extinction behavior for ^{12}CO in B59 would be illustrated. Two scatter commands referring to detections with S/N > 3 and S/N < 3 plot the whole set of data points. The color code is set by `c = sn_12co` to the S/N

values of the individual data points. A third plotting command adds error bars to all significant detections corresponding to the calculated error of the fit:

```
figure(figsize=(15,7))

scatter(ext_12co, int_12co, c=sn_12co, s=40)
plt.colorbar()
scatter(ext_12co_limits, limit_12co, marker='v',color='black',s=20)
text(96.2,30.7, 'S/N',  fontsize=13)
xlabel("Av [mag]")
ylabel("Intensity [K km/s]")

plt.errorbar(ext_12co, int_12co, linestyle='none', fmt='black',
             yerr = error_12co)
```

The molecular emissivity plots show the line intensity on the Y-axes in [K km/s] and extinction values on the X-axes in [mag]. The data points are displayed whether as filled circles or as black triangles depending on their S/N value. Detections which fulfilled the S/N criterion are shown colored regarding to their S/N value. For these data points error bars are provided. The remaining points with too low S/N ratio are shown as upper limits following the calculation described earlier in the text. In the next chapter the obtained scatter plots are discussed and compared to each other in order to investigate the relative differences/similarities between the sample cores.

5 Results

The present section mainly falls into two categories. First the results of the CO isotopologue analysis for all three sample cores are discussed in detail and compared to each other, whereas high density tracers are considered in the second part. Additionally to a presentation of scatter plots depicting the measured abundance profiles of CO components with growing extinction depths, calculations of excitation temperature and column density are presented. Latter is based on the work of Frerking et al., 1982 and was retrieved from the original work and 'Tools of Radio Astronomy' by Wilson et al., 2009 (chapter 15).

The second part of the section considers the emission behavior of high density tracers HCN, $H^{13}CN$, HNC, HCO^+, $H^{13}CO^+$. Complete data sets only exist for B59 and the Molecular Ring. A direct comparison between low and high density tracers in the optical thin regime allows to draw conclusions about the chemical and physical structure of the extinction cores. At higher densities CO is expected to get depleted from the gas phase leaving a depletion hole in the spectral map around the extinction peak. Caselli et al., 1999 investigated depletion effects on $C^{17}O$ and $C^{18}O$ in the starless cloud core Lynds 1544 in the Taurus molecular cloud. They found depletion of CO from the gas phase setting in at $\approx 10^5$ cm^{-3}. Except for H_2 molecular nitrogen is the least affected by depletion. For N_2 being a homonuclear molecule there exist the same observational difficulties as for H_2 but the daughter products NH_3 and N_2H^+ can be used to trace the most dense parts of the core. In general these tend to peak in a shell around the extinction peak inside the CO depletion hole (Bergin et al., 2002, Caselli et al., 1999). Figure 5.1 shows an example of CO depletion in B68 with N_2H^+ peaking in a shell-like structure within the CO depletion hole (Bergin et al., 2002).

Hotzel et al., 2002 pointed out how the out-freezing of CO onto dust grains changes the chemical and physical structure of the core. By CO depletion the cooling efficiency and thermal balance are altered. Gas-phase cooling can be greatly reduced and as a consequence gas kinetic temperatures might be increased (Goldsmith 2001). Furthermore depletion effects must be taken into account when deriving H_2 column densities by CO measurements.

In the last step of the analyzing process possible depletion effects in B59 and the Molecular Ring were investigated by comparison of $C^{18}O$ and N_2H^+. Abundance profiles as well as contour maps indicate that at least B59 is affected by gas-phase depletion of CO. The Molecular Ring shows in general less diversity in molecular emission and lower intensity values but might exhibit signs of ongoing depletion too.

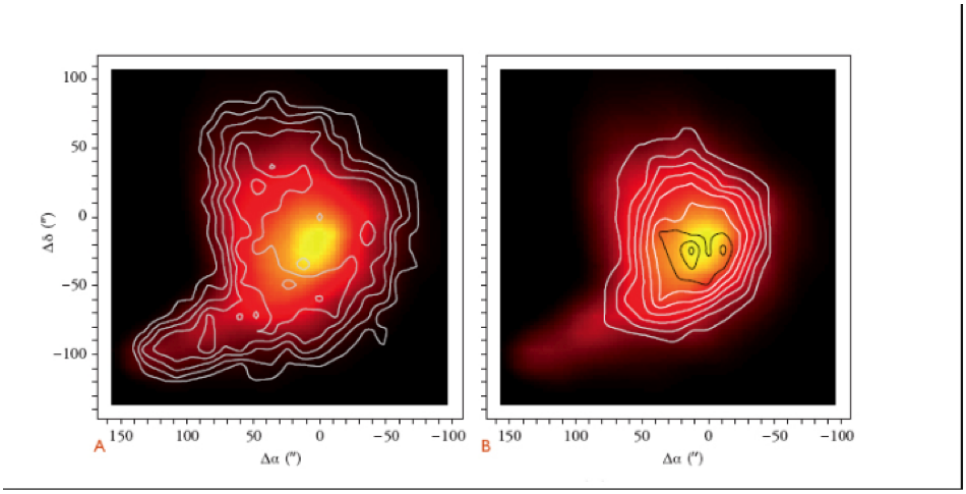

Figure 5.1: Extinction map of B68 overlaid with $C^{18}O$ contours (white) beginning at 0.2 K km s^{-1} with steps in units of 0.1 K km s^{-1} and N_2H^+ contours (green) beginning at 0.3 K km s^{-1} with steps in units of 0.2 K km s^{-1}; (Bergin et al., 2002)

5.1 CO Isotopologues in B59

As it was described in section 2.1 carbon monoxide requires a sufficient shielding of the interstellar radiation field to survive in molecular clouds. Thus there exists a certain threshold of optical depth in visual extinction for CO emission to arise. Regarding to their different relative abundances CO and its isotopologues possess different optical properties. This context already becomes apparent in the ratios of relative line strengths in the molecular spectra. Figure 5.2 shows a conglomeration of the averaged spectra of CO isotopologues ^{12}CO (*black*), ^{13}CO (*blue*) and $C^{18}O$ (*green*) in B59. By a comparison of temperature ratios at the peak with relative galactic abundances we obtain information about the optical properties of the different CO isotopologues. Following Wilson et al., 2009 chapter 16 the galactic values of relative abundances for CO isotopologues are given as:

$$\frac{^{12}CO}{^{13}CO} \sim 70 \qquad \text{and} \qquad \frac{^{13}CO}{C^{18}O} \sim 7.14 \tag{5.1}$$

Rohlfs & Wilson (2004) described how the $\frac{^{13}CO}{C^{18}O}$ intensity ratio can be related to the optical depths of both species. From the radiative transfer equation for the isothermal slab (5.4) they showed that:

$$\frac{T_A^* \ (^{13}CO)}{T_A^* \ (C^{18}O)} = \frac{1 - exp(-\tau_{13})}{1 - exp(-\tau_{18})} \tag{5.2}$$

Regarding to the dense environment and as one can see easily in figure 5.2 the relation between ^{12}CO and ^{13}CO line strength does not scale with a factor of 70 but with much smaller values. In the case of B59 the measured abundance ratios were:

$$\frac{^{12}\mathrm{CO}}{^{13}\mathrm{CO}} \sim 1.2 \qquad \text{and} \qquad \frac{^{13}\mathrm{CO}}{\mathrm{C}^{18}\mathrm{O}} \sim 5.59 \tag{5.3}$$

Since the relative abundances in the galactic field given in (5.1) represent the optical thin case strong differences imply ^{12}CO being optically thick whereas ^{13}CO behaves to C^{18}O very similar as in (5.1). In the other cores the respective ratios were found to be $\frac{^{12}\mathrm{CO}}{^{13}\mathrm{CO}} \sim 1.02$ and $\frac{^{13}\mathrm{CO}}{\mathrm{C}^{18}\mathrm{O}} \sim 5.78$ in Core 20 and $\frac{^{12}\mathrm{CO}}{^{13}\mathrm{CO}} \sim 1.96$ and $\frac{^{13}\mathrm{CO}}{\mathrm{C}^{18}\mathrm{O}} \sim 4.42$ in the Molecular Ring.

Although the abundance of C^{18}O is much higher in dense molecular cores the emission is still optically thin relative to the other CO isotopologues. This fact will play an important role in the column density determinations displayed later in the text.

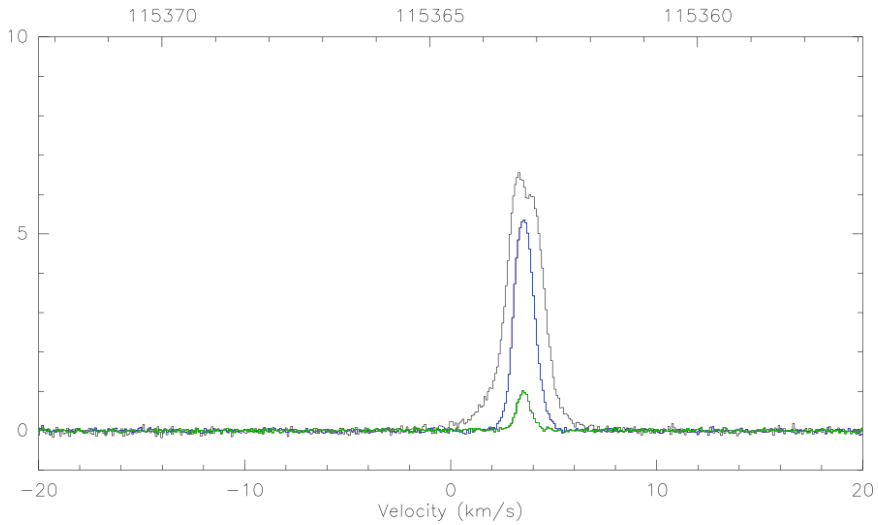

Figure 5.2: Conglomeration of the averaged spectra of CO isotopologues ^{12}CO (*black*), ^{13}CO (*blue*) and C^{18}O (*green*) in B59 with the y-axes representing antenna temperature in units of K

The different optical properties of the CO isotopologues were already described in section 4.1 on the basis of velocity integrated moment zero maps showing different distributions in the CO components. Those also become apparent in the comparison of integrated intensities with A_v. Figures 5.3 and 5.4 show the extinction-correlated abundance profiles of ^{12}CO and ^{13}CO color-coded by their $\frac{\mathrm{S}}{\mathrm{N}}$ value. The data cubes for the CO-mapping in B59 contained 1009 spectra. Those which fulfilled the selection

criterion of $\frac{S}{N} > 3$ are shown as colored data points while spectra with an $\frac{S}{N}$ value < 3 are represented as upper limits in form of black triangles. The upper limits were calculated by taking the integrated spectral noise of the fit times three. This way any possible detection which could be missed due to various reasons (e.g. sensitivity limits) is covered.

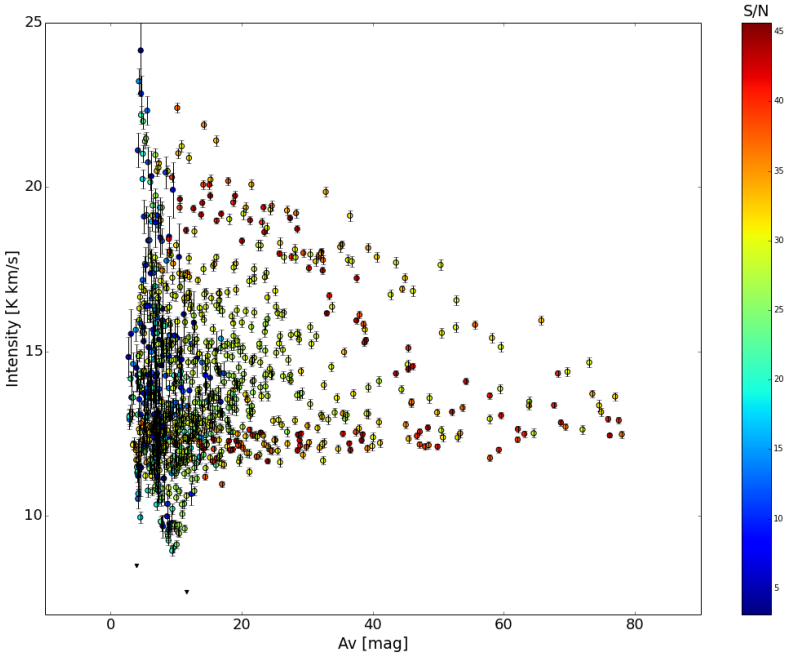

Figure 5.3: ^{12}CO emission in B59 versus extinction; the color of the data points refers to their S/N value (color bar), the mean error of the fits is $= 0.1$ K km s^{-1}. Data points below the S/N selection criterion are presented as upper limits (black triangles).

We detected ^{12}CO emission in B59 for an extinction range of 2.7 to 78 mag, below $A_v = 2.7$ mag no statements are possible. The ^{12}CO abundance declines from edge to center about ~ 8 K km s^{-1}. This reflects the spatial distribution shown in the moment zero map of ^{12}CO in fig. 4.3 in chapter 4. There the emission was found to arise mostly west to the extinction core declining toward greater densities. With a comparison to fig. 4.3 also the big scatter present in figure 5.3 can be explained. As a consequence of the spatial extension of the ^{12}CO component the extinction contours of B59 cover a broad range of intensity. The mean error of the gauss fits is 0.1 K km s^{-1}.

Due to the high detection rate in the $J = 1 \rightarrow 0$ transition ^{12}CO shows only very few upper limits (2 out of 1009 observations) which refer to edge pixels of very high spectral noise. Points of highest S/N seem to envelop the spectral distribution. This

comes from a co-adding of two observational maps which leaded to an increased signal to noise ratio in the overlapping area. Although the spectral noise too would be added a bar representing enhanced S/N values shows up if the spatial map is color-coded by S/N (fig. 5.4).

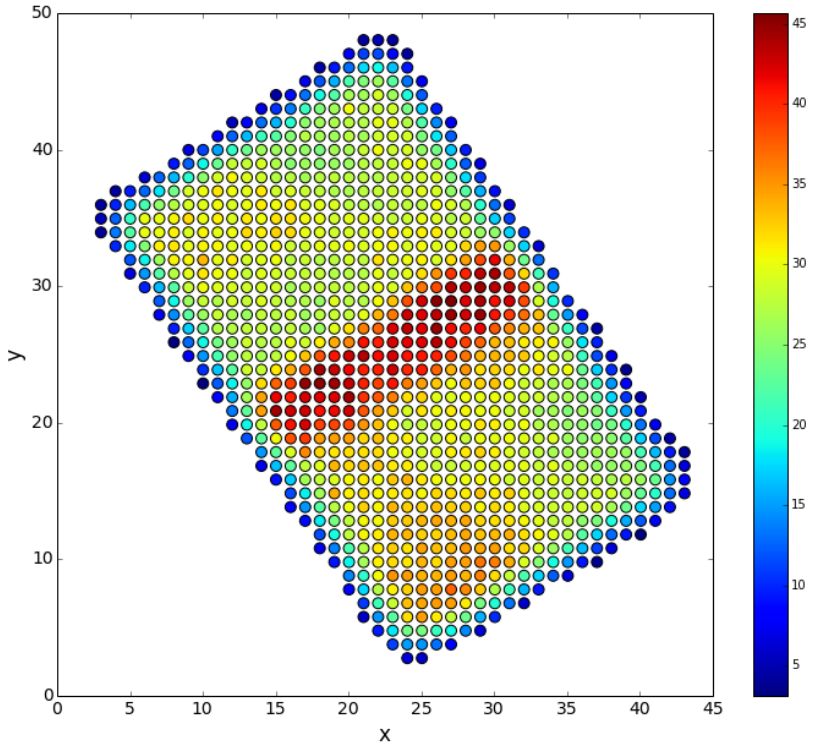

Figure 5.4: Spectral map of the ^{12}CO component in B59 color-coded by S/N. Axes are given in physical pixel coordinates.

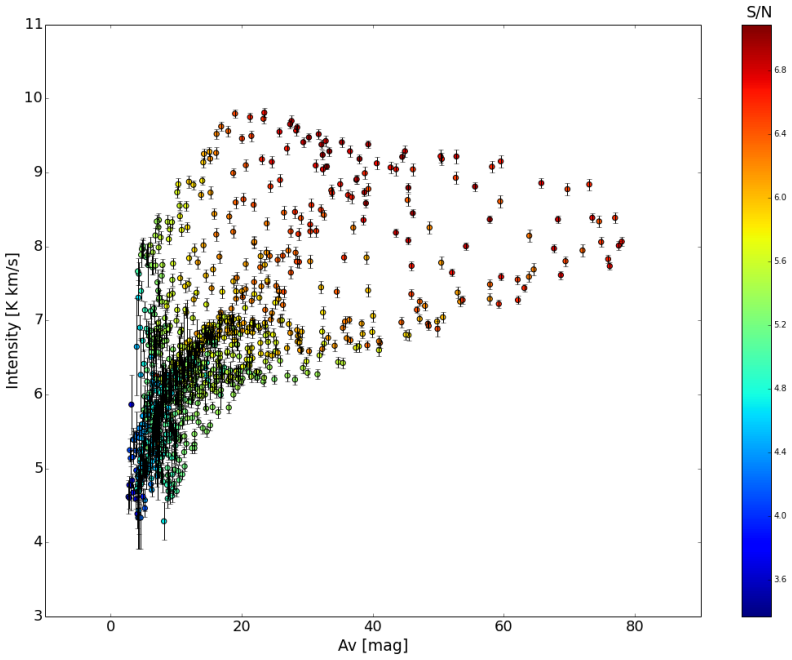

Figure 5.5: ^{13}CO emission in B59 versus extinction; the color of the data points refers to their S/N value (color bar), the mean error of the fits is $= 0.08$ K km s^{-1}. Data points below the S/N selection criterion are presented as upper limits (black triangles).

The ^{13}CO distribution in fig. 5.5 follows that of ^{12}CO but already shows some more detail in its morphology. Like ^{12}CO no emission is detected below ~ 2.5 mag. The temperature is steeply rising up to $A_v \sim 20$ mag where the trend turns around and starts to decrease slowly but systematically. Maximum integrated intensities at the extinction peak are found to lie ~ 1.8 K km s^{-1} below the peak values at $A_v \sim 20$ mag. In case of ^{13}CO no detections below $\frac{S}{N} \leq 3$ were found.

The S/N values this time represent a much more realistic picture with the highest values arising at greater extinction depths. Figure 5.6 depicts again the spatial map in physical x- and y-pixel coordinates color-coded by S/N. The distribution follows that of the ^{13}CO emission shown in the moment zero map in figure 4.4 and exhibits a more centrally concentrated shape than ^{12}CO.

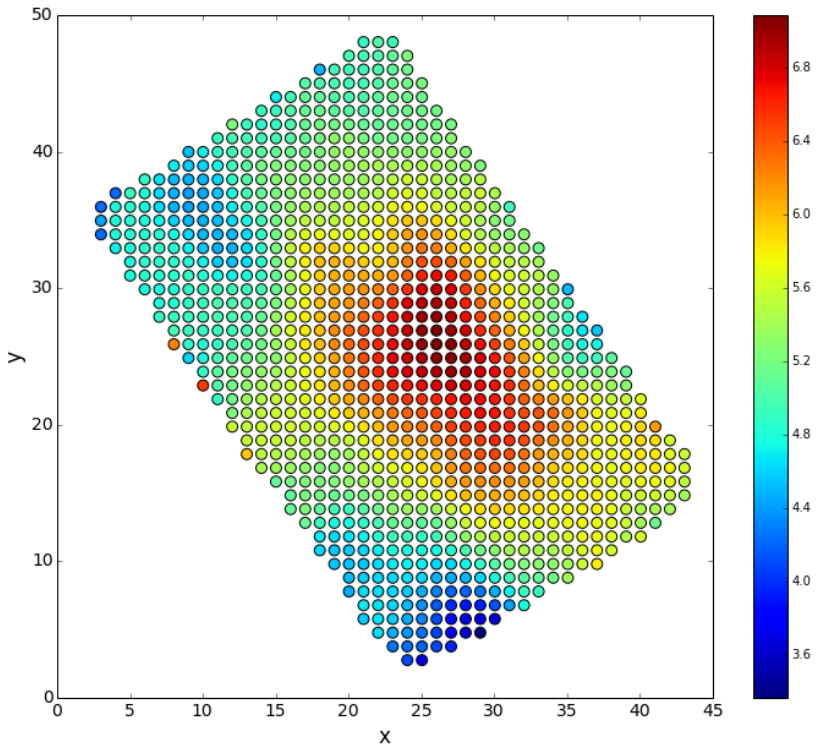

Figure 5.6: Spectral map of the ^{13}CO component in B59 color-coded by S/N. Axes are given in physical pixel coordinates.

With C^{18}O we encounter the first time an optically thin tracer and one immediately notices striking differences in the emission behavior (fig. 5.7). Contrary to the ^{12}CO and ^{13}CO component C^{18}O shows the lowest intensity at the outer cloud ranges and is rising constantly toward greatest extinctions. The increase in molecular line strength is more than 1 K km s^{-1} with the highest S/N values tracing the most dense parts of the core. The scatter of the data points is small compared with ^{12}CO and ^{13}CO with a mean error to the fits of 0.07 K km s^{-1}. The upper limits (813/1009) referring to data points with S/N < 3 show big scatter and are caused by noisy data points at the edges of the map.

After Lada et al. (1994) a linear correlation between integrated intensity and A_v corresponds to a constant abundance throughout the cloud. In figure 5.7 C^{18}O is found to rise linearly with increasing density until a break is indicated at approximately $A_v \approx 20$ mag followed by a second at approximately $A_v \approx 40$ mag. Bergin et al.

(2002) found a similar situation in the dark cloud *Barnard 68*. A decrease in molecular abundance with increasing extinction can be either due to depletion effects in the central regions or caused by high opacity saturating the molecular emission (Lada et al. 1994). Since $C^{18}O$ was already proven to stay optically thin up to highest extinction values the observed decline in molecular emission behavior must be a consequence of ongoing depletion effects in the extinction core.

As the only one low column density tracer which stays optically thin up to higher optical depths $C^{18}O$ emission can be used to compare with high density tracers. Such investigations can give indications if gas-phase depletion is going on in the extinction core and will be treated in context of high density tracers in section 5.4. But before moving to higher densities the next section will consider column density measurements based on the optical properties of $C^{18}O$.

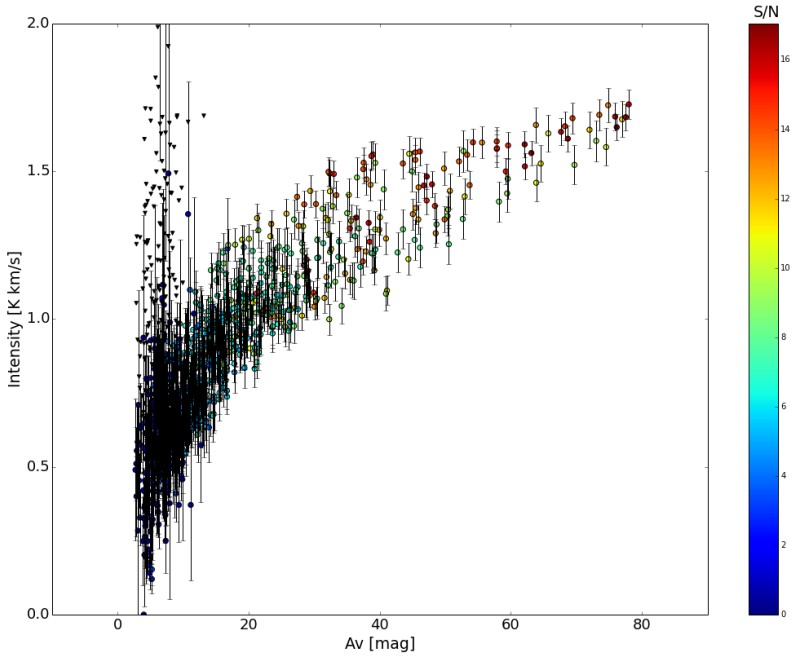

Figure 5.7: $C^{18}O$ emission in B59 versus extinction; the color of the data points refers to their S/N value (color bar), the mean error of the fits is $= 0.07$ K km s^{-1}. Data points below the S/N selection criterion are presented as upper limits (black triangles).

5.1.1 Excitation Temperature and Column Density in B59

The following approximation of excitation temperature and thereon based column density estimation is taken from Wilson et al., 2009 and can be found there in chapter 15. The basic concept is to relate the radiation brightness in the lowest transition(s) to a thermodynamic temperature. This can be achieved making the assumptions of an infinitely large medium (with respect to the telescope beam) in Local Thermal Equilibrium (LTE) defined by a single excitation temperature T_{ex}. In LTE a single excitation temperature is corresponding to an isothermal cloud where the transitions in question are thermalized and T_{ex} is describing the relative populations of all $J-$levels (Hotzel et al., 2002).

Equation (5.4) gives the radiative transfer equation for the isothermal case:

$$T_B = \left(1 - e^{-\tau}\right) \frac{h\nu}{k} \left(\frac{1}{exp\left(\frac{h\nu}{k\ T_{ex}}\right) - 1} - \frac{1}{exp\left(\frac{h\nu}{k\ T_{BG}}\right) - 1} \right) \tag{5.4}$$

Wilson et al., 2009 describes the derivation of this basic formula in the context of black-body radiation and brightness temperature in chapter 1. It is shown that two limiting cases exist:

1. For the optically thin case $\tau << 1$

$$T_B = \tau_\nu T \tag{5.5}$$

2. For the optically thick case $\tau >> 1$

$$T_B = T \tag{5.6}$$

As equation (5.4) contains the two unknowns τ and T_{ex} we can only use it for the optically thick case to derive the excitation temperature T_{ex}. Reduced by the term $(1 - e^{-\tau})$ we can convert equation (5.4) to

$$T_{ex} = \frac{T_0}{ln\left[1 + \frac{T_0}{T_A + \frac{T_0}{exp\left(\frac{T_0}{2.7}\right) - 1}}\right]} \tag{5.7}$$

with

$$T_0 = \frac{h\nu}{k} \tag{5.8}$$

and

- $h = 6.6206957 \times 10^{-34}[Js]$ as the Planck constant
- $k = 1.3806488 \times 10^{-23}[\frac{J}{K}]$ as the Boltzmann constant
- ν the frequency of the ^{12}CO $(J = 1 \rightarrow 0)$ transition ($\nu = 115.27120 \times 10^{9}$[MHz])

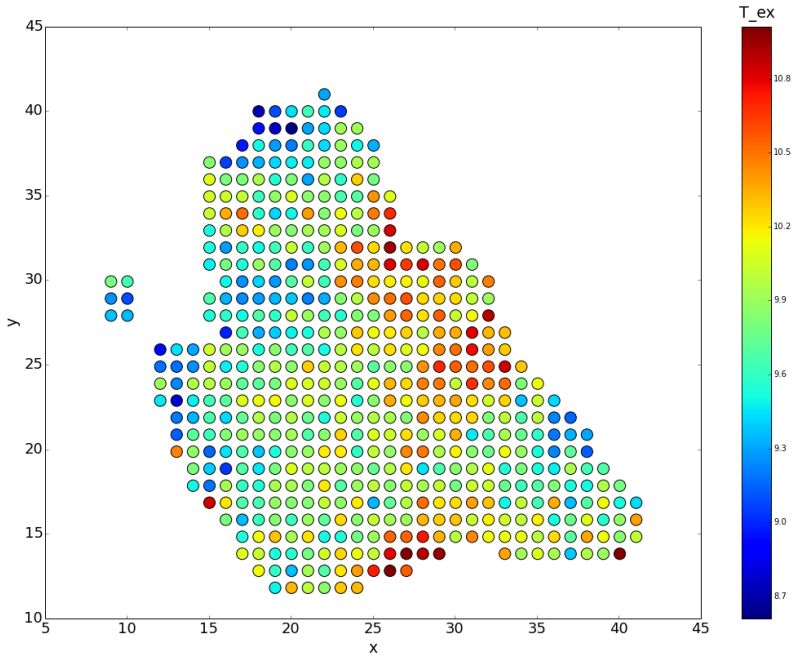

Figure 5.8: B59 in physical x and y coordinates color coded with excitation temperature T_{ex} derived by ^{12}CO for data points with $\frac{S}{N} > 5$

The derived excitation temperatures range between 8.2 and 13.3 K. Figure 5.8 shows the distribution of T_{ex} over the extinction core. The data points were restricted to S/N > 5 in order to trace the physical structure of the core. As we had assumed a constant excitation temperature along the line of sight T_{ex} values in the central region stay relatively constant scattering around a mean value of 10.02 K (standard deviation $\sigma = 0.6766$ K).

There exist several methods to derive CO column densities in molecular cores. Common to all is the constraint of an optically thin molecular line in order to trace the column density over a sufficient range of extinction. The method outlined in Wilson et al., 2009 is mainly based on the assumption that all CO isotopologues possess a uniform excitation temperature along the line of sight which in general cannot meet

the real conditions. Because we have found the ^{13}CO emission in B59 to turn optically thick the emission line of C^{18}O was used for column density determination. The total column density can be calculated via equation (5.9):

$$N_{C^{18}O} = 3.0 \times 10^{14} \frac{T \int \tau(\nu)\, \mathrm{d}\nu}{1 - exp\left(\frac{-5.3}{T_{ex}}\right)} \tag{5.9}$$

The optical depth of the C^{18}O line is obtained by solving equation (5.4) for

$$\tau_0^{18} = -ln\left[1 - \frac{T_{MB}^{18}}{T_0}\left[\left[exp\left(\frac{T_0}{T_{ex}}\right) - 1\right]^{-1} - 0.16\right]^{-1}\right] \tag{5.10}$$

In the optically thin regime the integral over τ can be approximated by the integrated line intensity $\int T_{MB}(\nu)d\nu$. The relation $T\ \tau(\nu) = T_{MB}(\nu)$ holds not completely and must be corrected for optical depth effects which can be eliminated to some extent using the approximation

$$T \int_0^\infty \tau(\nu)\, \mathrm{d}\nu \cong \frac{\tau_0}{1 - e^{-\tau_0}} \int_0^\infty T_{MB}(\nu)\mathrm{d}\nu \tag{5.11}$$

with

$$T_{MB} = \frac{T_A}{\mu_{MB}} \tag{5.12}$$

Like it is outlined in Wilson et al., 2009 the formulas' accuracy is about 15% for $\tau_0 < 2$. For $\tau > 1$ equation (5.9) overestimates CO column density but it's not mentioned to which extent. As the value of interest is not the column density of C^{18}O but rather the column density of H_2 the derived values have to be corrected for the relative abundance ratio of C^{18}O to H_2. A correction factor of 1.7×10^{-7} which is corresponding to the galactic mean of $\frac{\mathrm{C}}{\mathrm{H_2}} = 10^4$ satisfies the condition and leads to a mean value for H_2 column density of 8.849×10^{21} cm^{-2} ($\sigma = 3.209 \times 10^{21}$)..

Figure 5.9 shows a map of B59 color-coded in N(H_2) determined by C^{18}O which contains only data points with S/N > 5. Under these conditions the structure of the extinction core appears with its extensions to the southwest and north. The six data points to the left could be due to a small agglomeration of dust or a sign of overestimation.

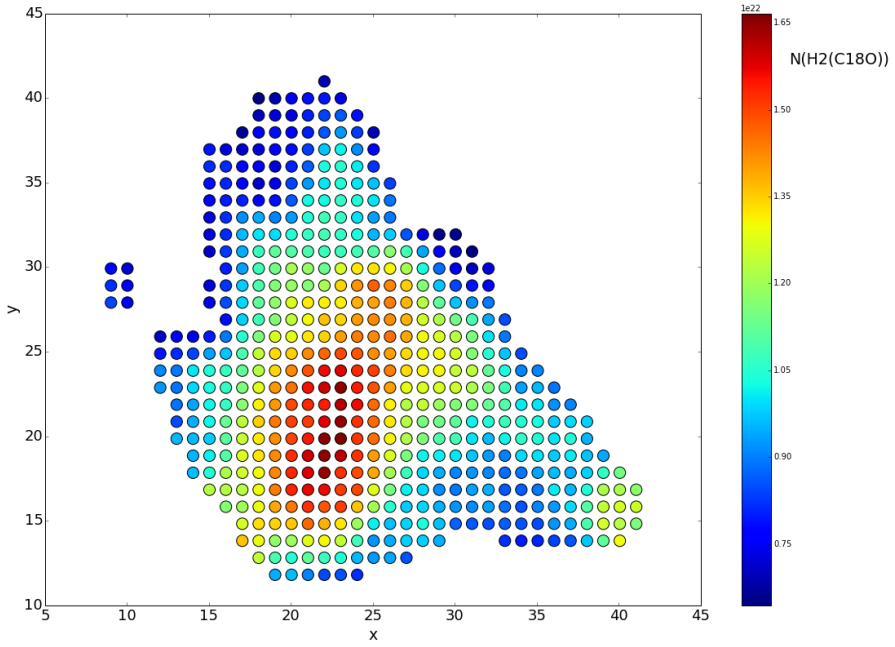

Figure 5.9: H_2 column density in B59 in x- and y- physical pixel coordinates for data points with $\frac{S}{N} > 5$

To compare H_2 column density with dust extinction the derived visual extinction values had to be converted into H_2 column densities too. This can be achieved by applying a conversion factor to A_v referring to the galactic gas-to-dust ratio. A complete discussion of this topic can be found in the literature for example in (Ryter et al., 1996 and Vuong et al., 2003).

Thus extinction values were multiplied by a factor 2.0×10^{21} cm^{-2} per magnitude in order to derive H_2-dust column densities for a direct comparison. Figure 5.10 shows the resulting plot with H_2 column density derived by dust absorption on the x-axes and N(H_2) calculated from $C^{18}O$ measurements on the y-axes. As it is described in the introduction of the present chapter H_2 column density determinations based on $C^{18}O$ measurements can lead to underestimation of N(H_2) if CO depletion effects are present in the inner core regions.

Naturally H_2 column density measurements derived by the methods of dust extinction and CO emission should be linearly correlated. Although the overall behavior in figure 5.10 meets the expected trend a decline in N(H_2($C^{18}O$) is found with increasing dust column density. The deviation from the linear regime becomes immediately apparent when comparing calculated mean column densities and standard deviations.

	min $[cm^{-2}]$	max $[cm^{-2}]$	mean $[cm^{-2}]$	st.dev σ $[cm^{-2}]$
$N(H_2(C^{18}O))$	6.437×10^{21}	1.666×10^{22}	8.849×10^{21}	$\sigma = 3.209 \times 10^{21}$
$N(H_2(dust))$	5.436×10^{21}	1.559×10^{23}	3.312×10^{22}	$\sigma = 2.765 \times 10^{22}$

Table 5.1: Column density ranges with calculated mean and standard deviation for $N(H_2(C^{18}O))$ and $N(H_2(dust))$ in B59

Values obtained with the method based on $C^{18}O$ are found to lie approximately one magnitude below derived dust column densities. Table 5.1 gives an overview of the column density ranges for the two different methods together with mean values and calculated standard deviation. The difference between the derived mean values is most likely a sign of ongoing CO depletion in the extinction core. Further comparisons with high density tracers in section 5.4 will allow a closer examination of possible depletion effects in B59. The excitation temperature given by the color code in figure 5.10 matches our assumption of a uniform T_{ex} along the line of sight being approximately 10 K for B59.

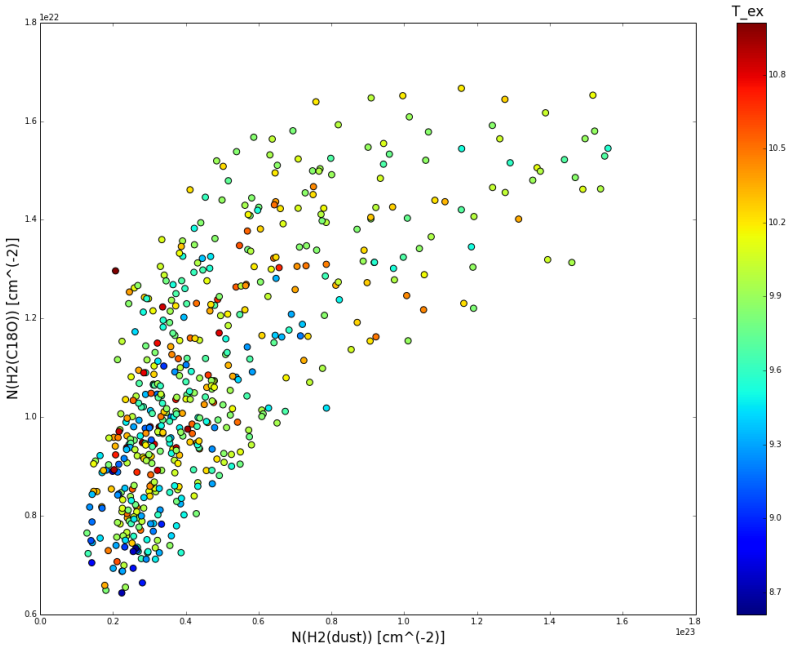

Figure 5.10: H_2 column density determined by $C^{18}O$ measurements vs. H_2 dust column density for data points with $\frac{S}{N} > 5$ color-coded with excitation temperature T_{ex} derived by ^{12}CO

5.1.2 Non-Detections

At first it seemed that no emission was measured for the $J = 1 \rightarrow 0$ transition line of $C^{17}O$ in B59 but at a closer look a marginally detected emission was found radiating only from the most central spectra. As the sum of these spectra was only a small part of the data sample an integration over the whole cube was not reasonable. Instead spectra covering the extinction peak were summarized with CLASS to a single averaged spectrum enhanced in its S/N ratio. Of this region the most intense emission could be inspected and as figure 5.11 shows $C^{17}O$ emission was detected in its two hyperfine components in the $(J = 1 \rightarrow 0)$ transition appearing at ≈ 4 K km s^{-1} and ≈ 1 K km s^{-1} with measured maximum intensities of ~ 0.5 K.

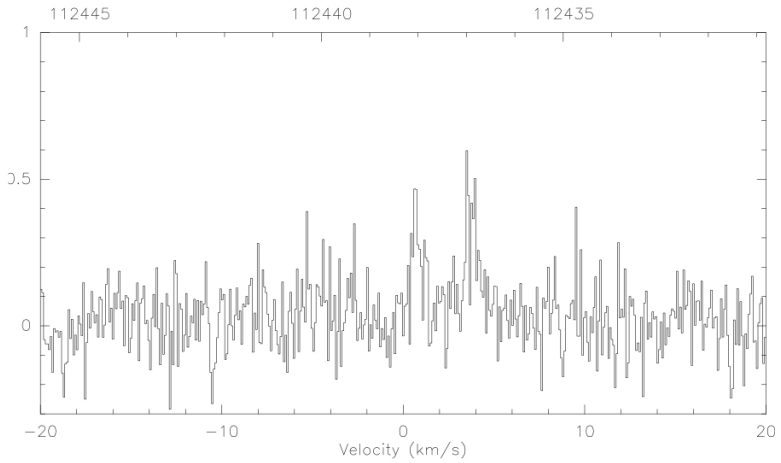

Figure 5.11: Averaged spectrum out of 20 observations in $C^{17}O$ covering the extinction peak of B59; spectral noise $\sigma = 0.10079$ K

5.2 CO Isotopologues in C20

Like it was already outlined in section 4.1 Core 20 possesses the lowest peak density values with a maximum of $A_v = 14.4$ mag and correspondingly also the weakest emission in CO isotopologues. When compared to the other cores the differences in ^{12}CO emission at these density ranges amount up to 15.9 K km s^{-1} for B59 and 17.5 K km s^{-1} for the Molecular Ring. Also for ^{13}CO the intensity in Core 20 is about 6.65 and 5.00 K km s^{-1} less respective to B59 and the Molecular Ring. Only the C^{18}O component shows similar intensities as in the other cores. This fact becomes also apparent in the corresponding abundance profiles with ^{12}CO and ^{13}CO displaying obvious differences to B59 whereas C^{18}O can be described as showing a much more similar behavior. Figures 5.12 and 5.13 present the ^{12}CO and ^{13}CO abundance profiles evolution with extinction. Both of them possess a good detection rate with only 12 detections below $\frac{S}{N} < 3$ out of 623 spectra for ^{12}CO and 66 upper limits for ^{13}CO.

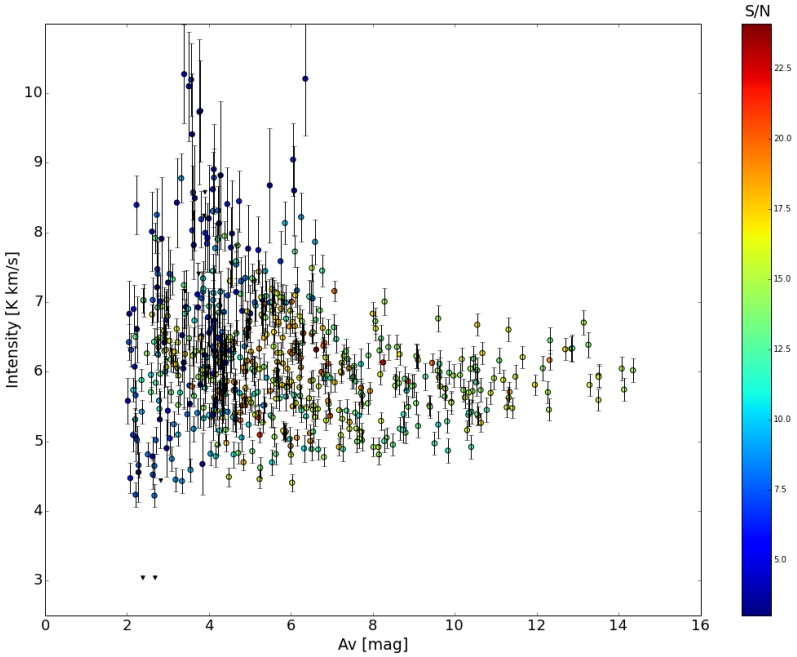

Figure 5.12: ^{12}CO emission in C20 versus extinction; the color of the data points refers to their S/N value (color bar), the mean error of the fits is = 0.12 K km s^{-1}. Data points below the S/N selection criterion are presented as upper limits (black triangles).

Similar as in B59 we detected no ^{12}CO emission below $\sim$ 2 mag and thereforee cannot make any statements about the very outermost cloud regions. In Figure 5.12

we find the scatter in ^{12}CO spanning a smaller intensity range than in B59. Moreover the scatter is declining by ~ 4 K km s^{-1} between 2 and 8 mag and the profile function $f(Int, A_v)$ is becoming more confined showing a steady trend until peak density values are reached. This behavior corresponds to the central concentration of the ^{12}CO emission in Core 20 shown in figure 4.8. The distribution at lower extinction ranges is not as broad as in B59 where the ^{12}CO component dominates mainly the outer shells of the extinction core.

The S/N values in figure 5.12 follow no particular trend being scattered in peak values over a broad density range of ~ 10 mag. In the case of Core 20 no observational data were added so this scatter must have some other reasons. The error of the fits gives also information about the S/N values reliability. Large errors represent a bad description of the integrated area to the line profile's real shape and so the derived peak intensity values of the fit may differ from the real signal strength. However, as S/N values are expected to rise toward greater extinction and the errors in fig. 5.12 are heavily decreasing with that direction, the scattered distribution of higher S/N values is most likely a consequence of the general low visual extinction in Core 20.

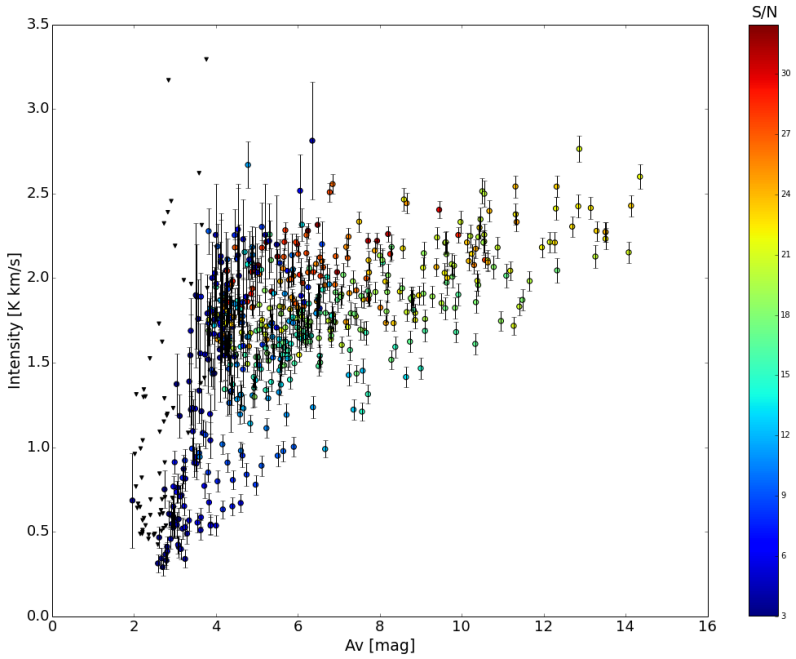

Figure 5.13: ^{13}CO emission in C20 versus extinction; the color of the data points refers to their S/N value (color bar), the mean error of the fits is $= 0.06$ K km s^{-1}. Data points below the S/N selection criterion are presented as upper limits (black triangles).

Figure 5.13 shows the intensity of ^{13}CO rising toward greater extinctions. The main trend follows a linear increase with a big scatter cloud at $\sim$ 5 to 8 mag containing the highest S/N values. As it was already described earlier in the context of C^{18}O a linear rise with density is representative of an optically thin tracer. A test after the abundance criteria described in equations (5.1) and (5.2) proven the ^{13}CO component in Core 20 to be optically thick at extinction ranges of $\sim$ 5 mag with abundance ratio values of $X\left[\frac{^{12}CO}{^{13}CO}\right] = 1.49$ K. Despite the general trend in the figure the steep increase at lower extinction ranges is crucial in determining the optical properties. After reaching its first maximum the curve tends to stay steadily rising only about 0.5 K km s^{-1} to the extinction peak.

For the C^{18}O component only 7 spectra out of 623 showed S/N values greater than 3. These spectra were located at the extinction peak. Exceptionally we tried to plot the data with a criterion referring to half the value applied for the other plots, namely $\frac{S}{N} > 1.5$. This way the calculated upper limits were reduced nearly by a factor of two from 616 being only 338 left and we were able to derive the general trend of the molecular line emission. It is to note, that due to the exceptionally reduced selection criterion the shown measurements should be taken as upper limits.

Detections shown in figure 5.14 display a strictly linear distribution rising over a density range of 2.0 to 14.4 mag. The function displays little scatter staying below values of $\sim$ 0.2 K km s^{-1}. In contrast to the C^{18}O emission measured in B59 there are no clear signs of a decrease in C^{18}O abundance toward the extinction peak. From this one can follow that the decline in abundance of ^{12}CO in Core 20 is most likely a consequence of its optical properties and not due to depletion. Although we obtained no measurements for high density tracers in Core 20 it is most likely that such - if present at all - would be not very abundant. The high closeness to B59, as Core 20 is more or less neighboring the star forming region, may be associated with a suppression or at least a hindering of chemical evolution in Core 20 due to the highly energetic radiation of the new born stars.

Like it was done for B59 the excitation temperature calculation for Core 20 is based on equation (5.7) and the assumption of a uniform T_{ex} along the line of sight for all CO isotopologues. Using the optically thick ^{12}CO emission line the obtained excitation temperature of Core 20 ranges between 5.411 K and 11.797 K with a mean of 8.106 K ($\sigma = 0.099$ K). Figure 5.15 shows again the distribution of T_{ex} in physical x and y pixel coordinates with the data points restricted to S/N$>$ 1.5. Corresponding to our assumption the derived temperatures appear to stay constant over the pictured range of the extinction core ($A_v = 2.21 - 14.4$ mag).

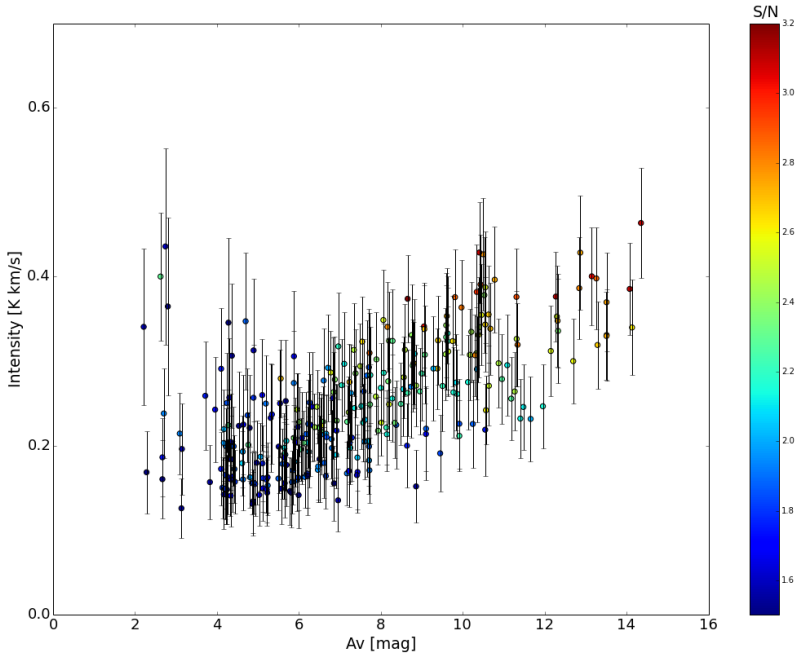

Figure 5.14: $C^{18}O$ emission (only marginally detected for the most part) in C20 versus extinction; the color of the data points refers to their S/N value (color bar), the mean error to the fits is $= 0.04$ K km s^{-1}. Data points below the S/N selection criterion are presented as upper limits (black triangles).

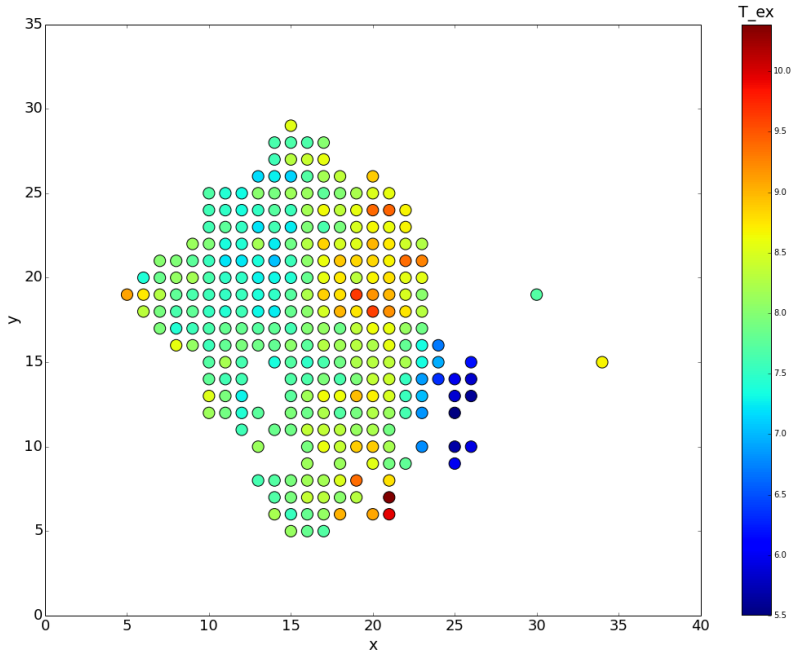

Figure 5.15: C20 in physical x and y coordinates color-coded with excitation temperature T_{ex} derived by ^{12}CO

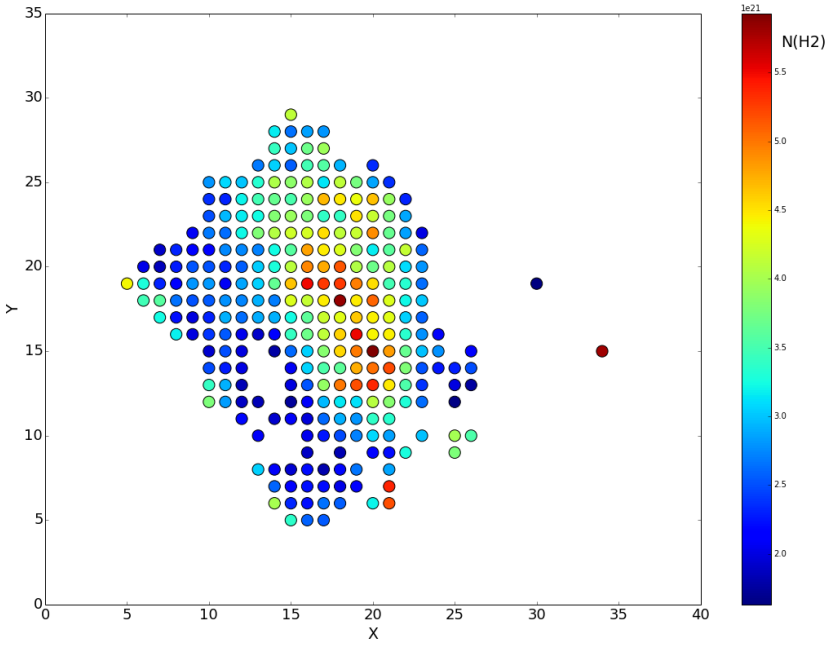

Figure 5.16: C20 in physical x and y pixel coordinates color-coded with column density N_{H_2}

	min $[cm^{-2}]$	max $[cm^{-2}]$	mean $[cm^{-2}]$	st.dev σ $[cm^{-2}]$
N(H_2($C^{18}O$))	1.63×10^{21}	5.93×10^{21}	2.783×10^{21}	$\sigma = 1.605 \times 10^{21}$
N(H_2(dust))	3.922×10^{21}	2.870×10^{22}	1.139×10^{22}	$\sigma = 5.055 \times 10^{21}$

Table 5.2: Column density ranges with calculated mean and standard deviation for N(H_2($C^{18}O$)) and N(H_2(dust)) in C20

Finally the H_2 column density was calculated using the optically thin $C^{18}O$ component and equation (5.9). The obtained values for N_{H_2} range between 1.63×10^{21} cm^{-2} and 5.93×10^{21} cm^{-2} with a mean of 2.783×10^{21} cm^{-2} ($\sigma = 1.605 \times 10^{21}$ cm^{-2}). Figure 5.16 shows the resulting column density map for data points with S/N > 1.5. The form and color reveal the structure of the C20 extinction core (compare figure 4.9). In order to relate these results with the core's density structure derived by visual dust extinction, H_2 column density was also calculated after Vuong et al., (2003) as described in 5.1. Like it is shown in table 5.2 obtained column density ranges and mean values differ by about 1 order of magnitude.

Figure 5.17 shows the results for H_2 column density derived by $C^{18}O$ measurements and dust extinction. Although differing by about 1 order of magnitude the two column density determinations seem to be linearly related except of some scatter points at lower optical depths. The color code refers to excitation temperature values derived by ^{12}CO and corresponds to a uniform excitation temperature throughout the core with T_{ex} being approximately 8 K. One could speculate that if depletion effects are present in Core 20 the decline in CO abundance may be less pronounced than in B59. But anyway it is to notice that the treated extinction range only spans over ~ 15 mag. In this regime the N_{H_2} column density relation in B59 also showed a linear behavior.

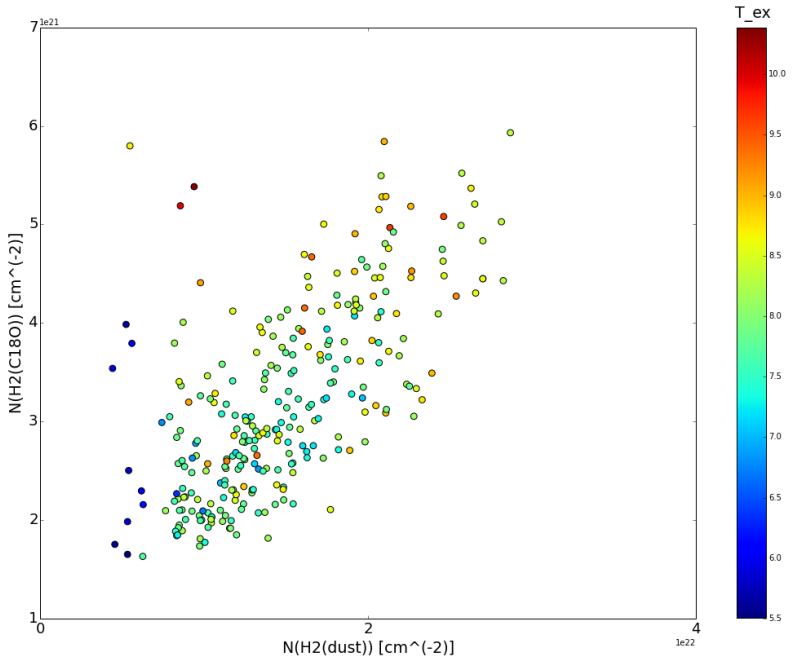

Figure 5.17: H_2 column density determined by $C^{18}O$ measurements vs. H_2 dust column density for data points with $\frac{S}{N} > 1.5$ color-coded with excitation temperature T_{ex} derived by ^{12}CO

5.2.1 Non-Detections

In Core 20, where we posses no high column density tracer observations, the only non-detection is represented by the $C^{17}O$ component. As it was not possible to fit a Gaussian to the spectrum because there is none the observation could not be treated any further. Thus the spectra located at the extinction peak were summarized and averaged to one single spectrum out of 18 with a reduced spectral noise of 0.16911 K. If there was a hidden emission somewhere in the core it would show up in the sum of the spectra. Like it is shown in figure 5.18 the averaged $C^{17}O$ spectrum is dominated by continuum noise and no distinct emission lines appear.

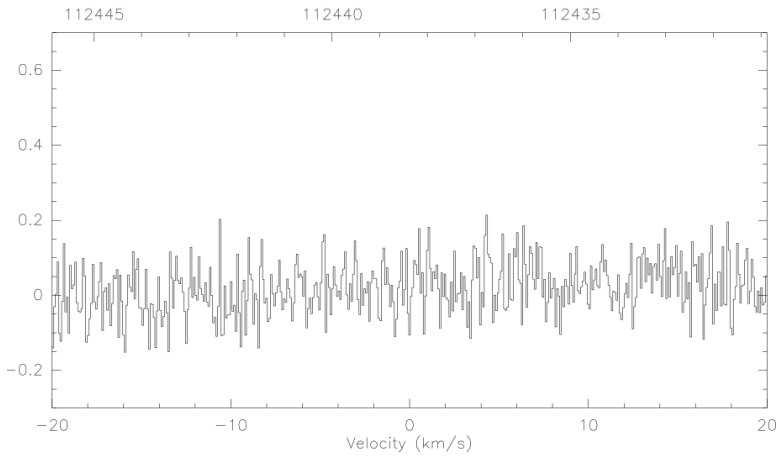

Figure 5.18: Averaged spectrum out of 18 observations in $C^{17}O$ covering the extinction peak of C20; spectral noise $\sigma = 0.16911$ K

5.3 CO Isotopologues in the Molecular Ring

Although the Molecular Ring at first seems to be very similar to B59 in his general CO emission properties a direct position-to-position comparison of the single spectra with the extinction map reveals some striking differences. It is noticeable that the ^{12}CO component is found to be the brightest of our sample although the Molecular Ring possesses with maximum visual extinction values of $A_v = 44$ mag only half the density of B59. Whereas ^{12}CO emission in B59 occurs already at extinction ranges of $A_v \approx 2.5$ mag ($A_v \approx 2$ mag in C20) in the Molecular Ring no detections below $A_v \approx 8$ mag were obtained and no conclusions can be drawn about the outermost cloud regions.

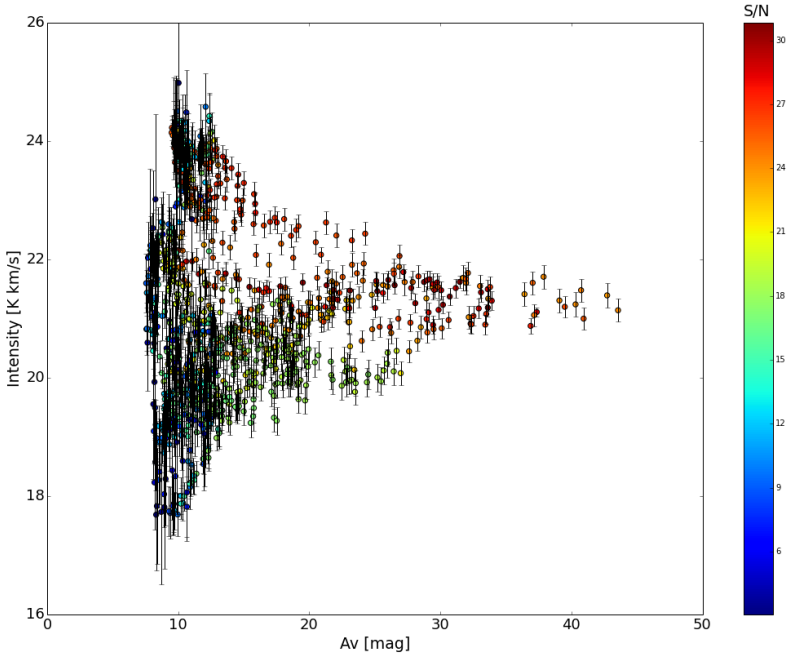

Figure 5.19: ^{12}CO emission in MR versus extinction; the color of the data points refers to their S/N value (color bar), the mean error of the fits is $= 0.2$ K km s^{-1}. Data points below the S/N selection criterion are presented as upper limits (black triangles).

Figure 5.19 shows the ^{12}CO intensity distribution with visual extinction. Like it was the case in B59 the emission radiates with highest intensities at the cloud edges and is declining toward the center by about ~ 3 K km s^{-1}. With higher density values also the scatter is systematically declining until at approximately $A_v = 30$ mag the trend changes to a steady intensity range until maximum extinctions are reached. As

it is given in table 4.1 highest measured intensities at the cloud edges were found to be 24.20 K km s^{-1} whereas 21.15 K km s^{-1} were measured at the extinction peak directly. In comparison measured intensities in B59 at $A_v = 44$ mag range between 12.00 and 18.00 K km s^{-1} being considerably smaller than for the Molecular Ring.

Out of altogether 1064 spectra only 8 were declared as non-detected and displayed through the calculated upper limits for these positions. The points of highest S/N are related to high intensity spectra and to greater extinction values. Like it was the case for B59 two observational maps were added. This again produced an area of enhanced S/N ratio. Figure 5.20 shows the resulting map color-coded in S/N to highlight the overlapping area in the center. The red colored part at the right corner corresponds to the location of the integrated emission of ^{12}CO shown in figure 4.11.

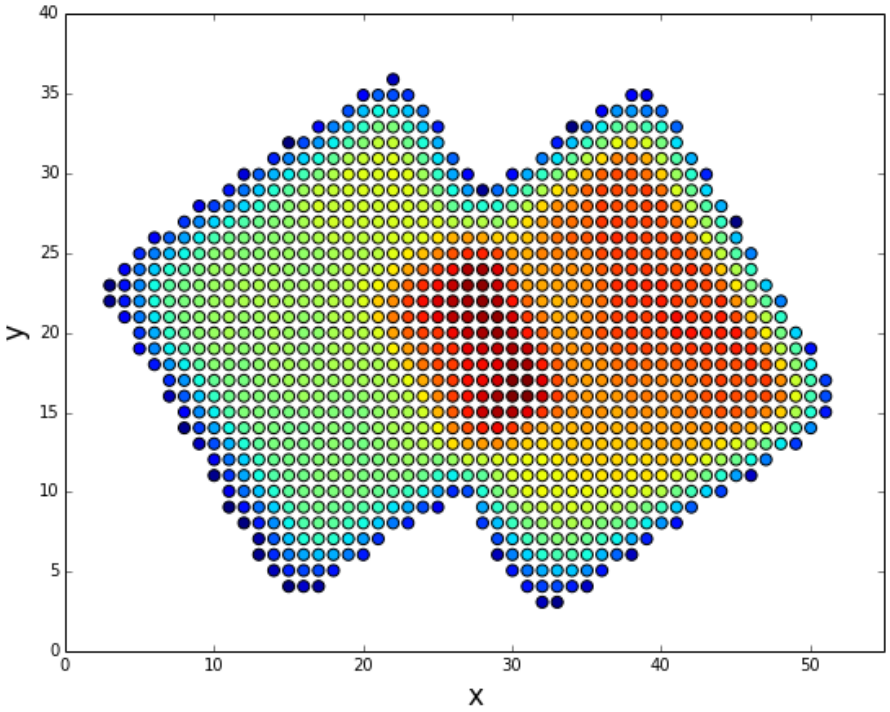

Figure 5.20: Spectral map of the ^{12}CO component in the Molecular Ring color-coded by S/N. Axes are given in physical pixel coordinates; see text for further description.

The ^{13}CO component in the Molecular Ring shows to emission maxima west and east of the extinction core (fig. 4.12). The emission is more extended than in B59 and spans a broader distribution in intensity at lower extinction ranges. Arising at a density

threshold of $A_v = 8$ mag the measured peak intensities are with 7.80 K km s^{-1} about 2 K km s^{-1} less than B59 at the outer core edges and are systematically declining until reaching 6.16 K km s^{-1} at the core center. At corresponding extinction ranges ^{13}CO emission in B59 is found to vary between 6.8 and 9.3 K km s^{-1} being therefore about $0.64 - 3.14$ K km s^{-1} higher than in the Molecular Ring.

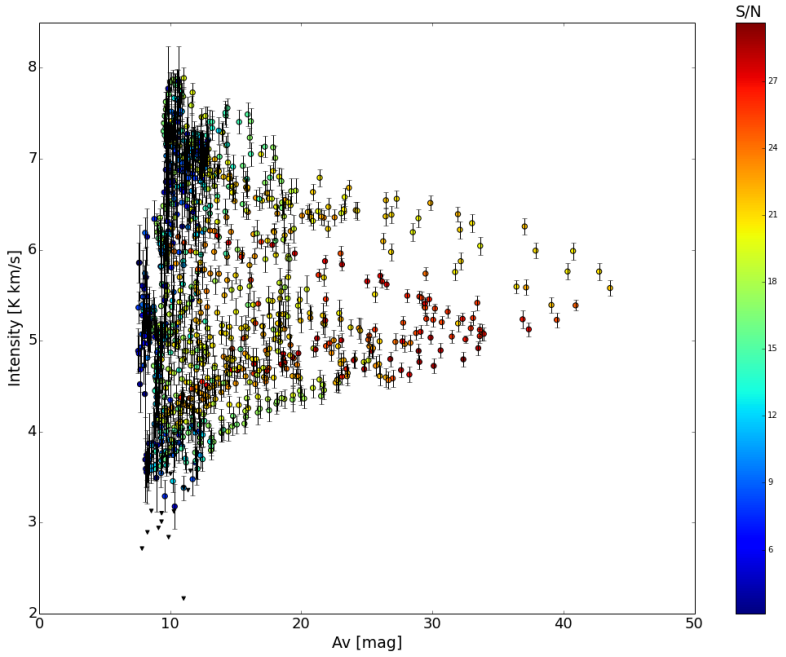

Figure 5.21: ^{13}CO emission in MR versus extinction; the color of the data points refers to their S/N value (color bar), the mean error of the fits is $= 0.2$ K km s^{-1}. Data points below the S/N selection criterion are presented as upper limits (black triangles).

The derived S/N values to the spectra in figure 5.21 suffer from the co-adding of the two maps in a way that they should not be given any credit. The fact that only low intensity points show high S/N ratios is very suspicious. As can be seen in figure 5.22 the high S/N values arise from the center of the map where we know that there is an emission minimum in the ^{13}CO component (fig. 4.12).

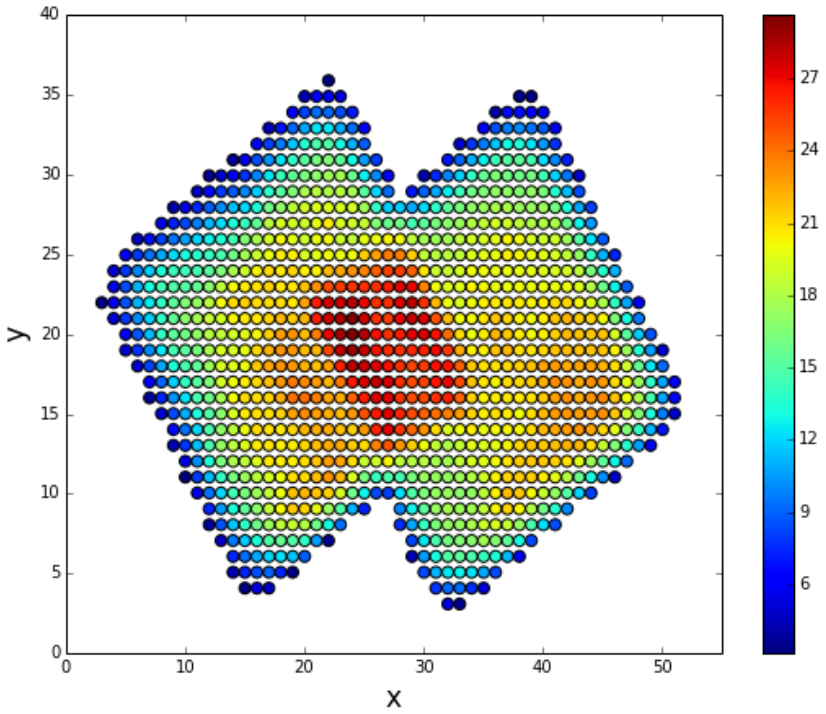

Figure 5.22: Spectral map of the ^{13}CO component in the Molecular Ring color-coded by S/N. Axes are given in physical pixel coordinates; see text for further description.

The C^{18}O component in the Molecular Ring differs from its counterparts in the other sample cores. Figure 5.23 shows the derived abundance profile for C^{18}O over an extinction range of $\sim$ 8.5 to 44 magnitudes. In contrast to the other cores the function shows very large scatter over a broad extinction range of about 20 mag. The emission is rising steeply up to a maximum at $A_v = 20$ mag followed by a steep decrease until $A_v = 30$ mag where the curve flattens out and remains steady until $A_v = 44$ mag are reached.

In section 4.1 the $C^{18}O$ emission in the Molecular Ring was already described to show two maxima with integrated intensity values of 0.8 K km s^{-1} west and east of the core. The exact positions of the maxima are $\alpha = 17^h\ 34^m\ 27^s$, $\delta = -25°\ 50'\ 30''$ and $\alpha = 17^h\ 34^m\ 02^s$, $\delta = -25°\ 50'\ 34''$ (see figure 4.13). Toward the core center the emission is declining about 0.37 K km s^{-1}. The difference to B59 at corresponding extinction ranges is about 0.82 to 1.19 K km s^{-1} at $A_v = 44$ mag.

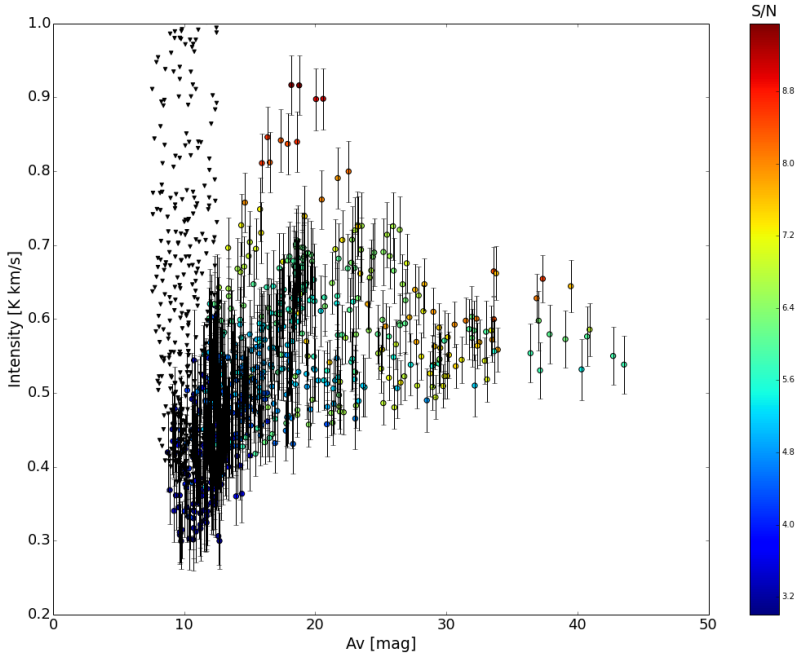

Figure 5.23: $C^{18}O$ emission in MR versus extinction; the color of the data points refers to their S/N value (color bar), the mean error of the fits is = 0.04 K km s^{-1}. Data points below the S/N selection criterion are presented as upper limits (black triangles).

The western component counts to the highest S/N and intensity values dominating at $A_v \sim 20$ mag. Out of 1064 detections 643 were counted as significant fulfilling the S/N criterion of greater than 3 and 421 detections were declared as non-detected of which upper limits were calculated. Those appear in fig. 5.23 only at low extinction ranges and have been proven to originate from the outermost pixel rows of the spectral map.

In a last step excitation temperature and column density were calculated according to equations (5.7) and (5.9). Abundance ratio calculations after (5.1) proven ^{12}CO

being optically thick whereas $C^{18}O$ stays optically thin up to highest extinction values. The respective abundance ratios were $\frac{^{12}CO}{^{13}CO} \sim 1.96$ and $\frac{^{13}CO}{C^{18}O} \sim 4.42$. This lead to temperature ranges of $T_{ex} = 7.32 - 10.71$ K with a mean excitation temperature of 9.08 K ($\sigma = 0.62$ K). The H_2 column density based on $C^{18}O$ observations was calculated to range between 3.874×10^{21} and 1.171×10^{22} cm^{-2} with a mean value of 5.46×10^{21} cm^{-2} ($\sigma = 2.000$ cm^{-2}).

Figure 5.24 and 5.25 show the spatial distribution of the derived excitation temperature and H_2 column density in units of physical pixel coordinates. The data points were restricted to S/N > 3 which reveals the physical structure of the extinction core; (pictured are extinction ranges from $A_v = 8.74$ mag to $A_v = 44$ mag).

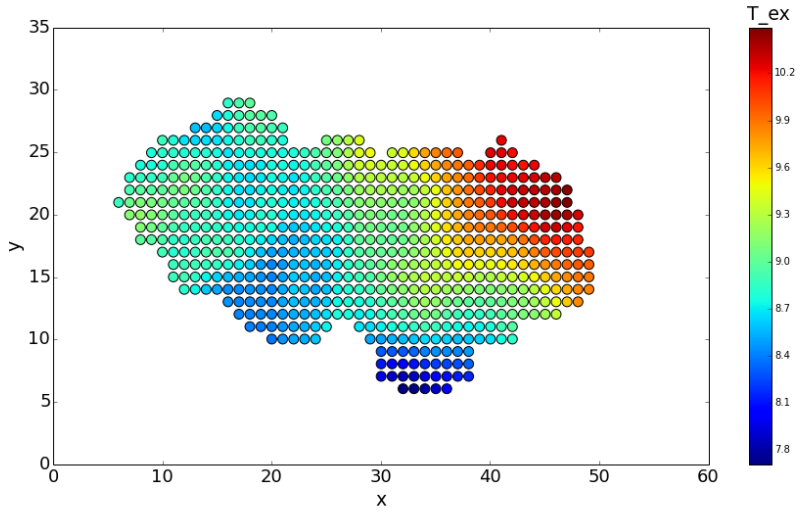

Figure 5.24: MR in physical x and y pixel coordinates color coded with excitation temperature T_{ex} derived by ^{12}CO

In figure 5.25 the extinction peak located in the western side of the core is traced very well. However, in order to compare H_2 column density based on $C^{18}O$ emission with observed dust extinction, N(H_2) was calculated again by applying a conversion factor to derived visual extinction values (see Ryter et al., 1996 for a complete discussion). Table 5.3 gives the derived values for column density ranges according to the two different methods. Again we found a deviation in calculated mean column densities of about 1 order of magnitude which is representative for a strong decline in CO abundance with higher densities and could be again a sign of depletion effects in the inner core regions. Figure 5.26 pictures the relation between column density values derived by dust extinction and by CO measurements. Similar as in B59 and Core 20

	min [cm^{-2}]	max [cm^{-2}]	mean [cm^{-2}]	st.dev σ [cm^{-2}]
N(H_2(C^{18}O))	3.874×10^{21}	1.171×10^{22}	5.463×10^{21}	$\sigma = 2.000 \times 10^{21}$
N(H_2(dust))	1.511×10^{22}	8.711×10^{22}	2.865×10^{22}	$\sigma = 1.2557 \times 10^{22}$

Table 5.3: Column density ranges with calculated mean and standard deviation for N(H_2(C^{18}O)) and N(H_2(dust)) in the Molecular Ring

the resulting column density values differ by one order magnitude with N(H_2(dust)) exceeding N(H_2(C^{18}O)). In contrast to the respective plots for B59 (fig. 5.10) and C20 (fig. 5.17) we found a warmer gas component influencing the distribution at lower A_v. This component is about one degree warmer than the average excitation temperature of the core being approximately 9 K (see table 5.5, page 101).

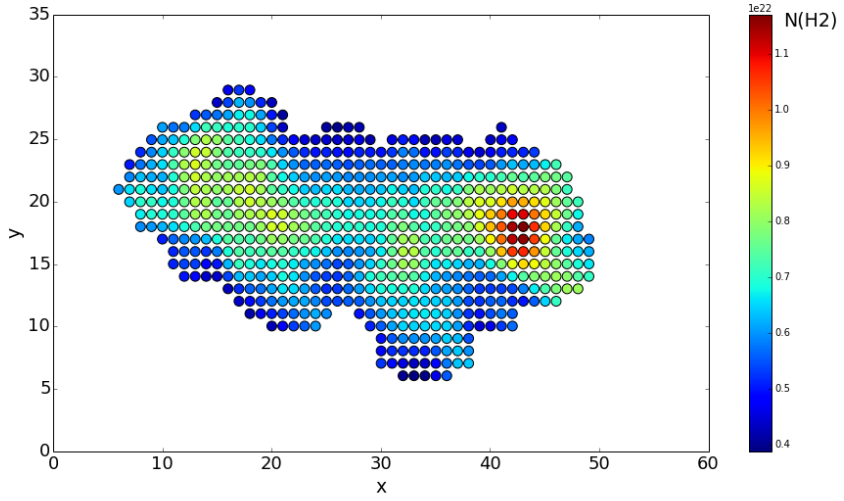

Figure 5.25: MR in x and y coordinates color coded with column density N_{H_2}

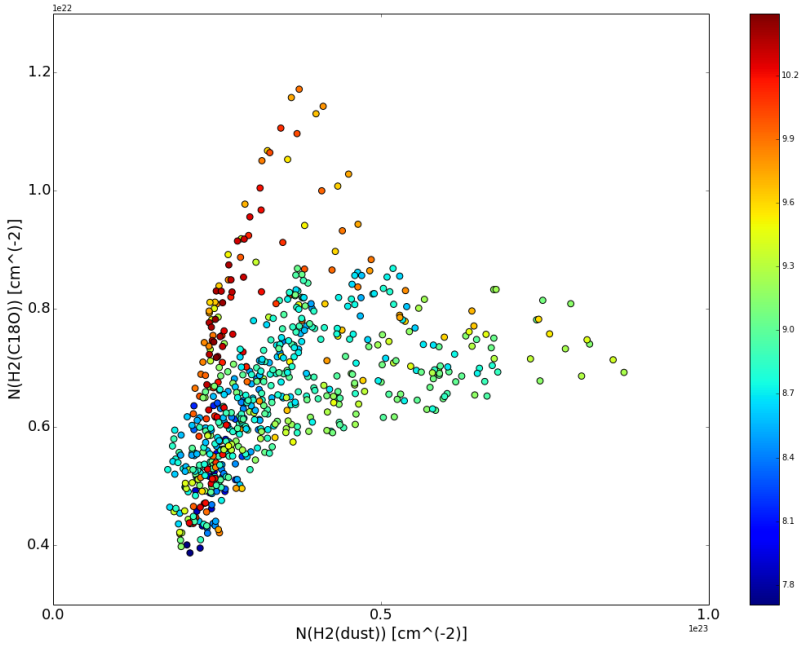

Figure 5.26: $C^{18}O$ column density in the Molecular Ring vs. dust column density color-coded with excitation temperature T_{ex} derived by ^{12}CO

5.3.1 Non-Detections

As it was the case in Core 20 the Molecular Ring too shows no emission in $C^{17}O$. Figure 5.27 displays the averaged spectrum summarized over 15 spectra covering the extinction peak of the map. Maybe one could find to see a slight rise in the continuum noise at about 4.5 km s^{-1} accompanied by a second rise at approximately 1 km s^{-1}, which most probably represent a weak detection of $C^{17}O$ and its hyperfine structure component in the first transition. The characteristics are much less distinct than in B59. A fit to the line profile was in any case not reasonable and like it was the case for the other two cores the observation was not treated any further.

Before the text continues with high density tracer observations a short summary will collect the most important results of the present section. As Core 20 was only observed in its four isotopologues it will not show up again in the remaining part of the section.

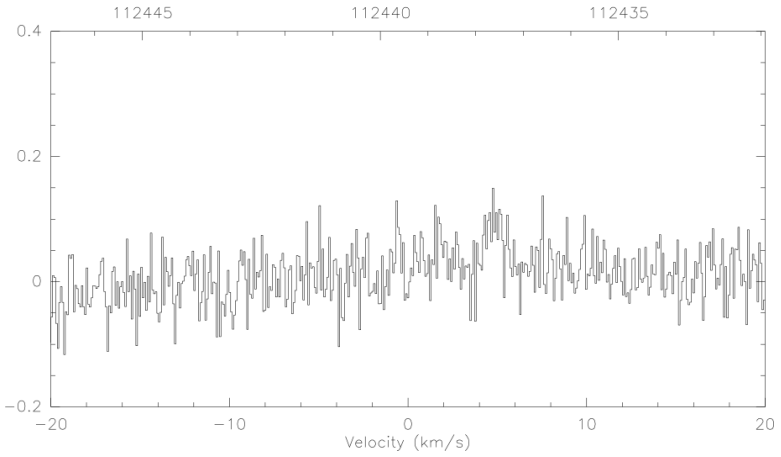

Figure 5.27: Averaged spectrum out of 18 observations in $C^{17}O$ covering the extinction peak of MR; spectral noise $\sigma = 0.12169$ K

5.3.2 Summary

The spatial distribution shown in the integrated intensity maps in section 4.1 is represented in the extinction correlated abundance profiles where the optically thick ^{12}CO and ^{13}CO component in general show a strong declination from edge to center whereas C^{18}O tends to rise toward greater extinctions. The data points in the plots representing single spectra at a certain position were divided referring to the retrieved S/N values into significant detections $\left(\frac{S}{N} > 3\right)$ shown as colored dots and non-detections $\left(\frac{S}{N} < 3\right)$ presented as upper limits. Latter were calculated by multiplying the measured intensity with three times the spectral noise calculated for the integration area. In this way any possible detection which could be missed due to various reasons (e.g. sensitivity limitations) is covered. The ^{12}CO component shows due to the high detection rate in the $(J = 1 \rightarrow 0)$ transition in general very few upper limits. In B59 those were 2 detections out of 1009, whereas Core 20 possesses a somewhat weaker detection rate in ^{12}CO with 66 upper limits out of 623 observations being present, and the Molecular Ring possesses 8 upper limits out of 1064 detections. For B59 and the Molecular Ring ^{12}CO emission was found to decline slowly but systematically toward greater extinctions which corresponds to a decline from edge to center by ≈ 8 K km s^{-1} and ≈ 2.7 K km s^{-1} for B59 and the Molecular Ring respectively. Both cores display large scatter at lower extinction ranges which is due to the ^{12}CO emission peaking mostly west to the extinction core (B59) or to both sides (MR). In Core 20 the ^{12}CO component is much more centrally concentrated as becomes visible in the integrated intensity maps in section 4.1. The emission is much steeper declining between $A_v = 4 - 8$ mag than in the other cores and flattening out into a steady trend until greatest extinctions. The decrease in integrated intensity from edge to center amounts to 1.15 K km s^{-1} reaching 6.00 K km s^{-1} at the extinction peak whereas B59 and the Molecular Ring show much higher intensities of 15.9 K km s^{-1} and 17.5 K km s^{-1} at corresponding extinction values of $A_v = 14.4$ mag. Furthermore it is noticeable that the Molecular Ring showed the highest detection threshold with no molecular emission being observed below 8 magnitudes of visual extinction whereas B59 and Core 20 possess comparable values of $A_v = 2.5$ mag and $A_v = 2$ mag, respectively.

For the ^{13}CO component again similarities between B59 and the Molecular Ring were detected whereas Core 20 shows some discrepancies. In Both B59 and MR the ^{13}CO emission is decreasing with extinction with a steeper inclination found for the Molecular Ring. The differences between core edge and center amount to 1.8 K km s^{-1} (B59) and 1.64 K km s^{-1} (MR). At extinction values of $A_v = 44$ mag B59 lies with integrated intensities ranging between $6.8 - 9.3$ K km s^{-1} only $0.64 - 3,14$ K km s^{-1} above the Molecular Ring with 6.16 K km s^{-1}. In the integrated intensity map of the

^{13}CO component in the Molecular Ring two emission maxima located slightly east and west to the core become visible whereas the distribution in the other two cores is much more centrally concentrated. However B59 showed still large scatter at extinction values smaller than $A_v = 20$ mag spanning a range of ~ 4 K km s^{-1}. Core 20 exhibits the smallest scatter reaching maximum values of ~ 1.5 K km s^{-1} for $A_v < 8$ mag. A scatter cloud between $A_v = 5 - 8$ mag was proven ^{13}CO to already have turned optically thick at these extinction ranges. Unlike that in the other two sample cores the main trend of the abundance function for ^{13}CO in Core 20 follows a strictly linear increase. In B59 and the Molecular Ring ^{13}CO emission was found to decline from edge to center by about 1.8 K km s^{-1} only Core 20 is increasing in ^{13}CO toward the center by ~ 0.2 K km s^{-1}. If it were not for the scatter cloud at $A_v = 5 - 8$ mag the emission behavior resembles strongly that of an optically thin tracer but despite the general trend the steep increase at lower extinction ranges in crucial is determining the optical properties. For B59 no non-detections in the ^{13}CO component were measured; Core 20 possesses 66 upper limits out of 623 observations and the Molecular Ring shows only 14 detections below $\frac{S}{N} = 3$.

Integrated peak intensities of C^{18}O were found to be comparable for the three sample cores. In the extinction abundance profiles B59 and Core 20 exhibit a strictly linear behavior in C^{18}O whereas the Molecular Ring possesses two locally emission maxima and shows significant scatter at extinction ranges smaller than $A_v = 30$ mag. For B59 and Core 20 C^{18}O emission is found to rise constantly toward the extinction peak reaching 1.72 K km s^{-1} at $A_v = 80$ mag in B59 and 0.46 K km s^{-1} at $A_v = 14.4$ mag in C20. At density values corresponding to the extinction peak of Core 20 B59 shows with $0.63 - 1.06$ K km s^{-1} somewhat higher intensities. Both emission lines have been proven to behave optically thin but the extinction abundance profile of C^{18}O in B59 shows a declination toward the core's center. Since opacity can be excluded this decline in abundance must be a consequence of depletion in the central regions. This can be proven by a direct comparison of C^{18}O with high density tracers e.g. N_2H^+ and will be treated in the next section. Furthermore it is to mention that C^{18}O in Core 20 was only marginally detected and the selection criterion exceptionally was reduced by a factor of two $\left(\frac{S}{N} > 1.5\right)$. This way the upper limits in the plot were reduced from being 616 out of 623 detections to be only 338. In the Molecular Ring 421 spectra out of 1064 didn't fulfill the $\left(\frac{S}{N} > 3\right)$ criterion and were shown as upper limits. Due to two local emission maxima slightly west and east to the extinction core ($\alpha = 17^h\ 34^m\ 27^s$, $\delta = -25^\circ\ 50'\ 30''$ and $\alpha = 17^h\ 34^m\ 02^s$, $\delta = -25^\circ\ 50'\ 34''$) the Molecular Ring shows very large scatter at lower extinction ranges spanning ~ 0.7 K. At $A_v \sim 20$ mag the emission reaches a maximum followed by a steep decrease to $A_v = 30$ mag. From

	B59	C20	mol. ring
$T_{ex(^{12}CO)}$	10.02 K	8.10 K	9.08 K
$N_{(C^{18}O)}$	8.84×10^{21} cm^{-2}	2.78×10^{21} cm^{-2}	5.46×10^{21} cm^{-2}
$N(H_2(dust))$	3.312×10^{22} cm^{-2}	1.139×10^{22} cm^{-2}	2.865×10^{22} cm^{-2}

Table 5.4: Mean Values for derived excitation temperature and column density in B59, Core 20 and the Molecular Ring

$A_v = 30$ mag to $A_v = 44$ mag the curve flattens out staying steady until peak extinctions are reached.

In contrast to B59 and Core 20 where $C^{18}O$ intensities are found to rise strictly linear to the core's center the Molecular Ring shows an overall decline of about 0.37 K km s^{-1} toward the center. At density values corresponding to the extinction peak of Core 20 B59 shows with $0.63 - 1.06$ K km s^{-1} at $A_v = 14.4$ mag somewhat higher intensities. As in the other cores $C^{18}O$ emission has been proven to be optically thin in the Molecular Ring so the observed decline in abundance must be related to depletion as it was the case in B59. A direct comparison to high density tracers in the next section will reveal if depletion effects are likely.

By comparison of abundance ratios of $\frac{^{12}CO}{^{13}CO}$ and $\frac{^{13}CO}{C^{18}O}$ with the values obtained in the galactic field representing the optically thin case the optical properties of CO isotopologues could be defined. For all three cores ^{12}CO and ^{13}CO were found to behave optically thick whereas $C^{18}O$ remains optically thin toward greatest extinctions. This fact was used to derive CO excitation temperatures and H_2 column densities in the sample cores after the method outlined in Wilson et al., 2009, chapter 15.

In order to compare results for $N(H_2)$ with the core's density structure derived by extinction measurements A_v had to be converted into H_2 column density too. This was achieved by applying a correction factor of 2.0×10^{21} cm^{-2} per magnitude to the measured extinction values, which takes the galactic gas-to-dust ratio into account. A detailed discussion of this can be found in Vuong et al., 2003. Table 5.4 gives a comparison of the calculated mean values for H_2 column density derived by $C^{18}O$ measurements and by visual dust extinction. The results differ from each other by approximately one order of magnitude which may be caused by depletion effects reducing the gas phase abundance of CO and therefore leading to an underestimation of H_2 column density based on $C^{18}O$ measurements.

5.4 High Density Tracers in B59

As the name tells highs density tracers possess higher critical densities at which the molecular transitions become thermalized and so they are expected to radiate from the more central parts of the core. Thus upper limits can provide us with useful information at which ranges no emission can be found. Table 2.1 in chapter 2 gives an overview of calculated critical densities for the investigated molecules. HCN possesses the lowest critical density of the observed high density tracers followed by HNC, HCO^+ ($H^{13}CO^+$) and N_2H^+. In B59 all molecules except of $H^{13}CN$ were detected and sorted referring to the selection criterion of $\left(\frac{S}{N} > 3\right)$.

Figure 5.28 shows the HCN component versus extinction with 219 calculated upper limits (black triangles) out of 929 observations. As expected for high density tracers HCN behaves optically thin rising linearly between $A_v \sim 10 - 80$ mag reaching 0.86 K km s^{-1} at the extinction peak. With extinction also the scatter increases spanning a range of ~ 0.4 K km s^{-1} at the peak.

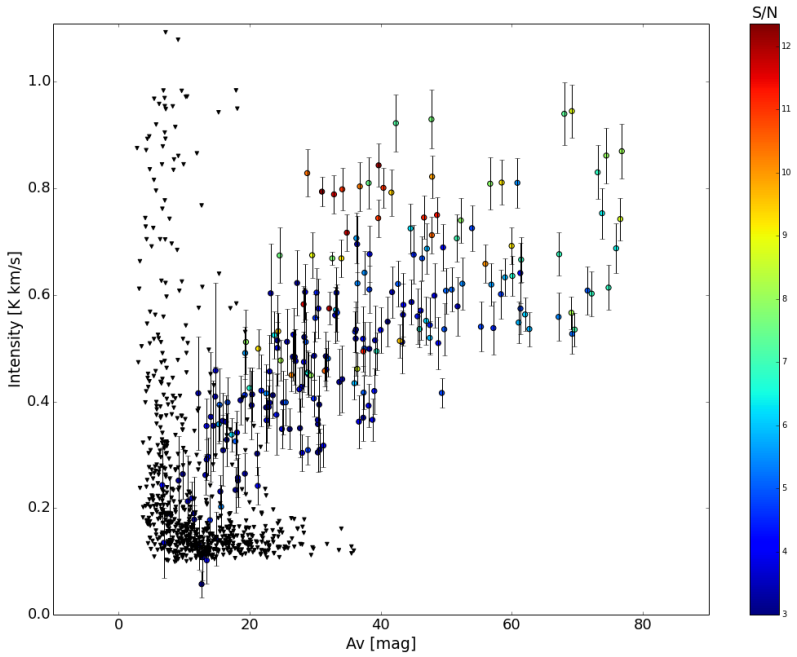

Figure 5.28: HCN emission in B59 versus extinction; the color of the data points refers to their S/N value (color bar), the mean error of the fits is $= 0.047$ K km s^{-1}. Data points below the S/N selection criterion are presented as upper limits (black triangles).

Like it was already outlined in section 4.1 HCN and its isomer HNC are thought to have the same formation mechanism (Sarrasin et al., 2009) and to form in equilibrium (Loison 2014). But although HNC is less stable than HCN and should be negligible abundant the contrary is observed. That's the reason why intergalactic ratios are given as HNC to HCN. In the literature large variations of $\frac{\mathrm{HNC}}{\mathrm{HCN}}$ are observed varying between $\frac{1}{80}$ for high star forming regions like e.g. ONC-I (Schilke et al., 1982) to values of $\frac{\mathrm{HNC}}{\mathrm{HCN}} = 1 - 4.5$ of molecular clouds (Graniner et al, 2014).

In B59 the HNC component reaches maximum intensities of 1.72 K km s^{-1} at the extinction peak therefore being about 0.30 K km s^{-1} more intense than HCN. The ratio of both yields $\frac{\mathrm{HNC}}{\mathrm{HCN}} = 1.4$. Thus B59 lies at the lower ranges reported for molecular clouds in the literature which could be related to the star forming activity in the core.

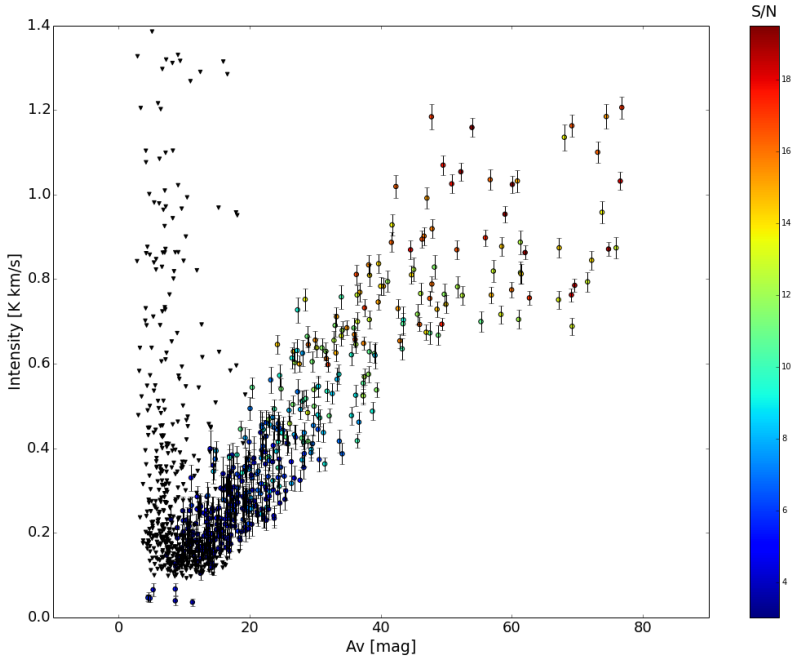

Figure 5.29: HNC emission in B59 versus extinction; the color of the data points refers to their S/N value (color bar), the mean error of the fits is = 0.025 K km s^{-1}. Data points below the S/N selection criterion are presented as upper limits (black triangles).

Figure 5.29 displays the evolution of HNC emission with extinction. The function follows a strictly linear trend rising from $\sim$ 0.22 K km s^{-1} at outer cloud ranges to 1.72 K km s^{-1} at $A_v = 80$ mag. In total 219 detections were listed as upper limits (as was the case for HCN) which were again related to the outermost pixel rows of the spectral map. Like N_2H^+ also the HNC molecule exhibits spectral hyperfine splitting

in its $(J = 1 \rightarrow 0)$ transition. As it was explained in section 4.3 in the context of hyper fine structure fits the standard deviation for the calculated errors of the individual fits in the single components in each spectrum was calculated and plotted as error bars to the total intensity.

HCO^+ and its rarer isotopologue $H^{13}CO^+$ lie at higher critical density ranges of about $1.34 \times 10^6 cm^{-3}$. As it is shown in figure 5.30 HCO^+ is still tracing the complete extinction range starting from a detection threshold at $A_v \sim 5$ mag. The overall trend follows a linear behavior rising toward the extinction peak but with large scatter at all extinction ranges. The intensities increase from 0.5 K km s^{-1} at outer core ranges to 0.95 K km s^{-1} at the $A_v = 80$ mag. Due to the large scatter maximum intensities are already reached at $A_v \sim 25$ mag. In the integrated intensity map (fig. 4.7) HCO^+ emission is found to be more extended than it is the case for the other high density tracers which appear more confined to the innermost extinction contours. For HCO^+ 209 spectra were listed as upper limits which again are related to the outer map ranges were spectral noise is greatly enhanced compared to the more central regions.

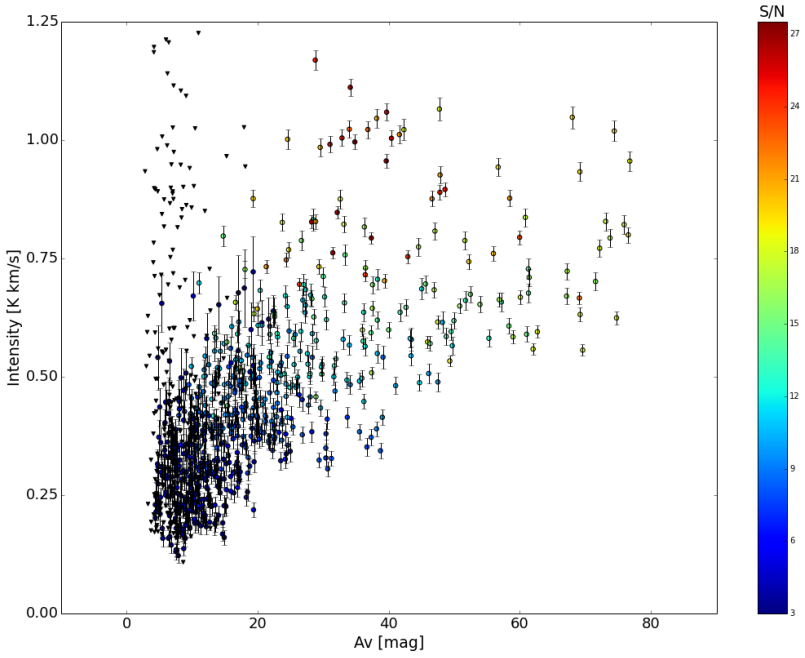

Figure 5.30: HCO^+ emission in B59 versus extinction; the color of the data points refers to their S/N value (color bar), the mean error of the fits is = 0.02 K km s^{-1}. Data points below the S/N selection criterion are presented as upper limits (black triangles).

The rarer isotopologue $H^{13}CO^+$ displayed in figure 5.31 also shows a strictly linear rise with extinction but with significantly less scatter than for HCO^+. No emission is detected below a detection threshold of $A_v \sim 14$ mag which is emphasized by the presence of 660 upper limits at lower extinction ranges. Intensities increase from 0.20 K km s^{-1} at the outer edges to 0.70 K km s^{-1} at the extinction peak.

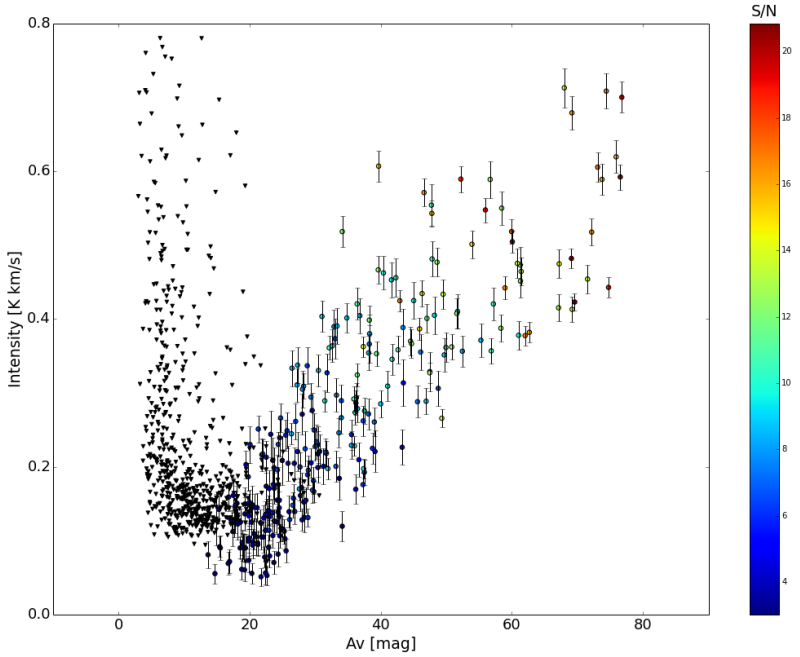

Figure 5.31: $H^{13}CO^+$ emission in B59 versus extinction; the color of the data points refers to their S/N value (color bar), the mean error of the fits is = 0.023 K km s^{-1}. Data points below the S/N selection criterion are presented as upper limits (black triangles).

As by far the strongest detected emission line of the high density tracers N_2H^+ reaches maximum values of about 2.52 K km s^{-1} at the extinction peak. The function is linear rising from 0.50 K km s^{-1} at the outer edges to 2.52 K km s^{-1} at A_v = 80 mag (figure 5.32). Also the scatter is increasing with extinction spanning a range of more than 1 K km s^{-1}. Figure 4.6 in section 4.1 shows N_2H^+ emission to be very centrally concentrated within the innermost extinction contours. The 794 derived upper limits belong again to edge pixels of the spectral map but also to the outermost pixels of the extinction core lying close to the edge of the map. A closer investigation of upper limits at higher extinctions revealed a high spectral noise of e.g. 5.09×10^{-2} K at

$A_v = 45$ mag whereas the retrieved signal strength amounts to 9.03×10^{-2} K.

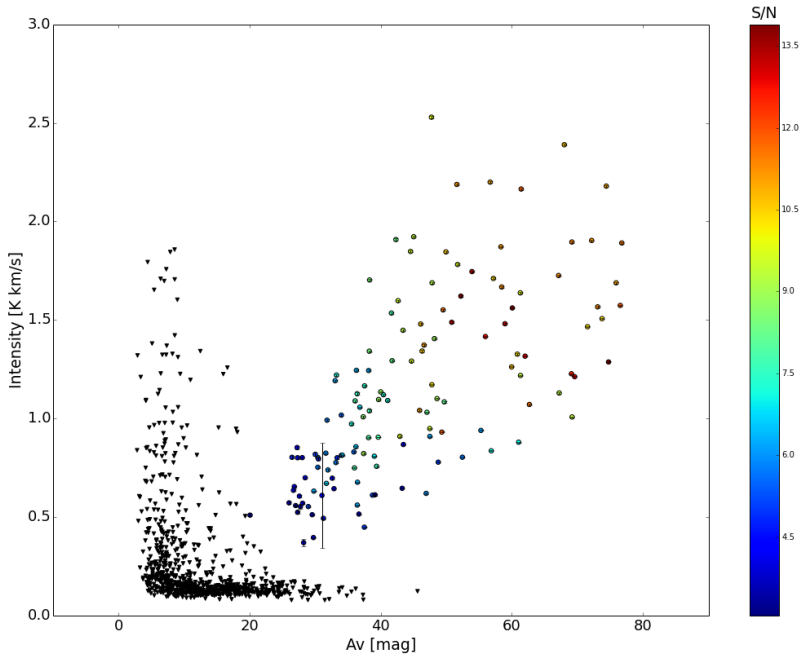

Figure 5.32: N_2H^+ emission in B59 versus extinction; the color of the data points refers to their S/N value (color bar), the mean error of the fits is $= 0.0058$ K km s^{-1}. Data points below the S/N selection criterion are presented as upper limits (black triangles).

In a last step the emission behavior of the optically thin low- and high density tracers $C^{18}O$ and N_2H^+ are compared as together they trace the complete range of extinction and thus draw a more general image of the core's physical and chemical structure.

Figure 5.33 shows the two abundance functions evolving with extinction. The $C^{18}O$ component is represented by the colored dots and N_2H^+ is shown as black stars. Whereas $C^{18}O$ declines in abundance toward the center, N_2H^+ emission is increasing systematically toward the extinction peak although showing larger scatter. As one can see in figure 5.33 N_2H^+ emission is arising at approximately $A_v = 20$ mag and starts to dominate over $C^{18}O$ at approximately $A_v = 40$ mag. Since $C^{18}O$ has been proven to be optically thin (equation 5.1) and N_2H^+ clearly dominates at the core center this is a clear sign of CO depletion going on in B59.

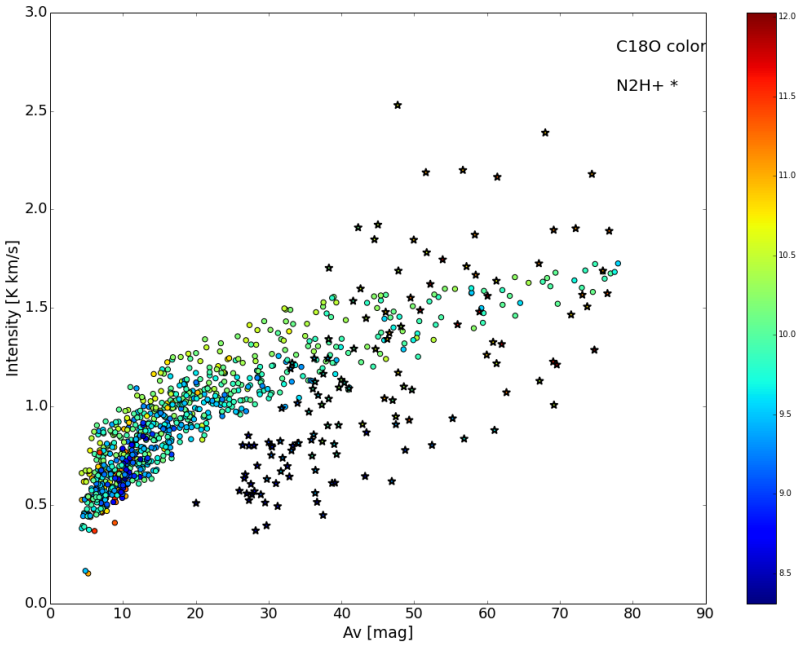

Figure 5.33: $C^{18}O$ (colored dots (T_{ex})) and N_2H^+ (black stars) in B59 versus extinction.

Figure 5.34 shows the two emission components normalized by extinction which gives an approximation of the relative abundances. Although extinction effects are removed it is to note that due to the rules of error propagation for division the error of the function $Q = \frac{a}{b}$ increases relative to the individual errors of a and b. Therefore the strong decrease in $C^{18}O$ recorded for the outer extinction ranges is not authentical. Of real scientific significance is the fact that $C^{18}O$ is constantly declining until $A_V = 80$ mag whereas N_2H^+ emission is not arising until $A_V \approx 27$ mag and remains constant toward the center.

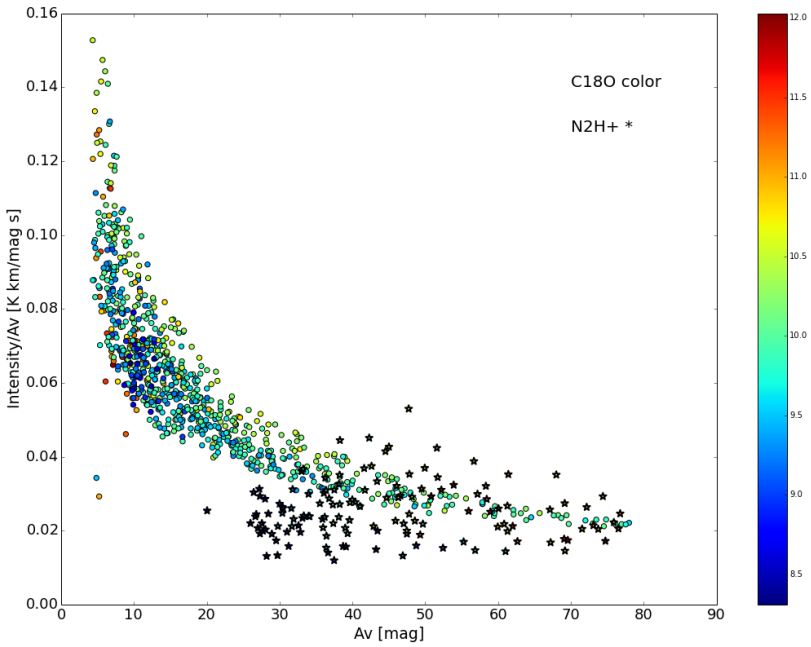

Figure 5.34: Intensity distribution normalized with extinction; $C^{18}O$ (colored dots (T_{ex})) and N_2H^+ (black stars) in B59 versus extinction.

Figure 5.35 shows the extinction map of B59 over plotted with intensity contours of $C^{18}O$ (black) and N_2H^+ (red). The map was obtained with karma/kvis. In order to emphasize just the molecular emission contours and the central regions of the core, rising visual extinction depths are implied by the coloring of the background. As one can see the black contours of the $C^{18}O$ component form a shell-like structure around the extinction peak with N_2H^+ emission peaking inside corresponding to the compared abundance profile shown in figure 5.33.

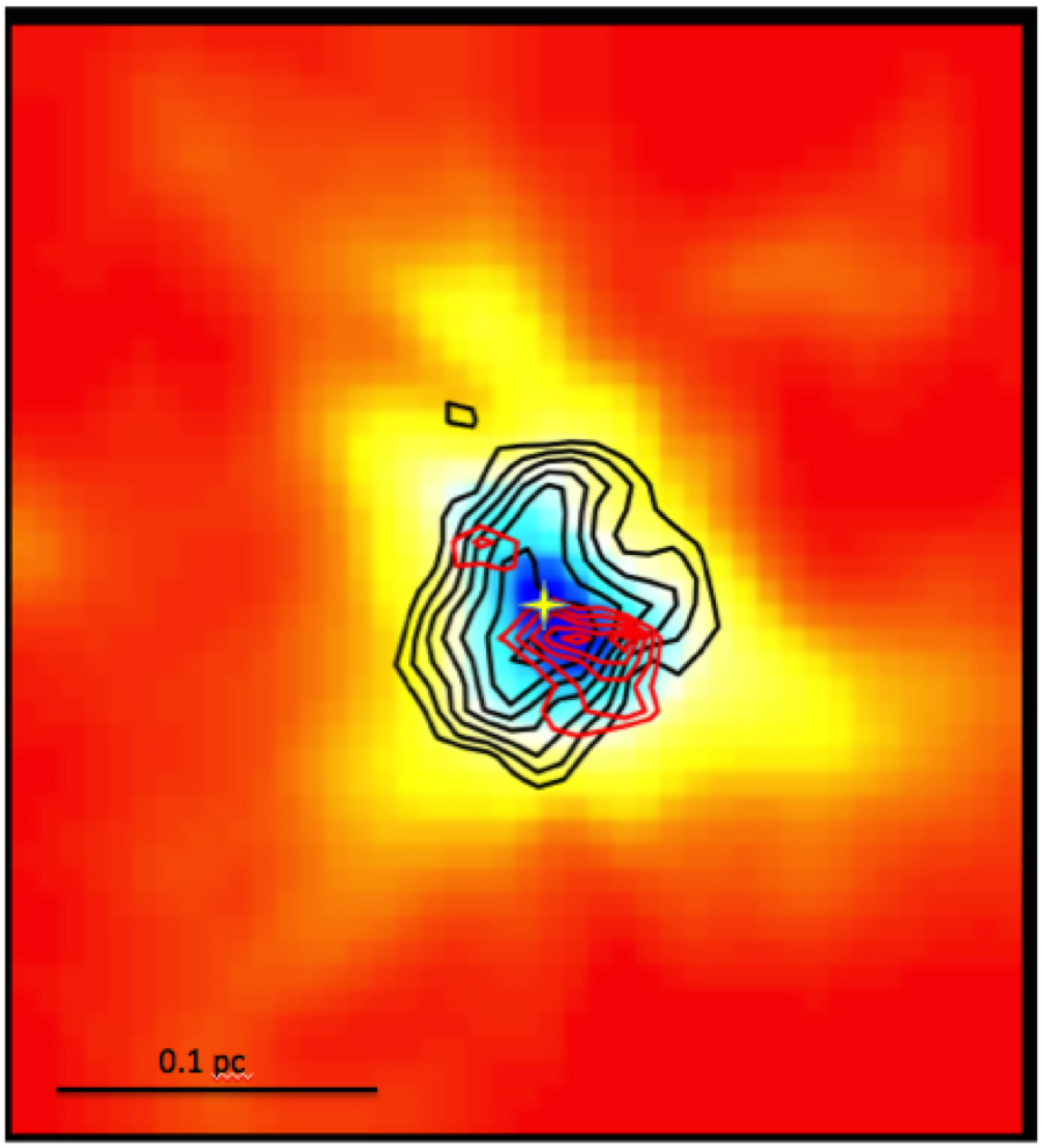

Figure 5.35: Extinction map of the B59 core over plotted with $C^{18}O$ contours (*black*) from $75-100\%$ $(100\% = 3.25\ \mathrm{K\ km\ s^{-1}})$ in steps of $+4\%$ and N_2H^+ contours (*red*) from $75-100\%$ $(100\% = 2.25\ \mathrm{K\ km\ s^{-1}})$ in steps of $+4\%$; the yellow star marks the central extinction peak.

5.4.1 Non-Detections

Beside of $C^{17}O$ only $H^{13}CN$ was found to show no significant detections. The observation was treated as any other non-detection and the central 25 spectra covering the extinction peak were summarized and averaged to a single spectrum. Figure 5.36 displays the resulting spectrum showing no identifiable emission line.

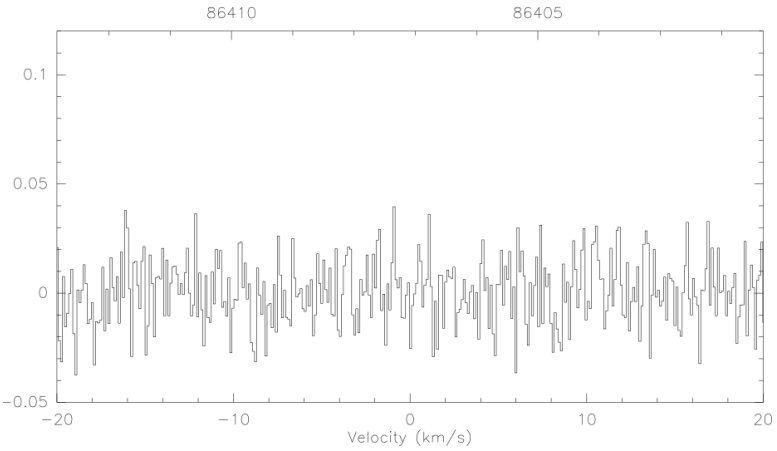

Figure 5.36: Averaged spectrum out of 25 observations in $H^{13}CN$ covering the extinction peak of B59; spectral noise $\sigma = 0.02910$ K

In the following again a short summary recaps the most important results of the present section.

5.4.2 Summary

The investigated high column density tracers span a range in critical density from 6.842×10^5 cm^{-3} (HCN) to 1.107×10^6 cm^{-3} (N_2H^+). Except of $H^{13}CN$ all observations possessed a high detection rate and could be investigated for their abundance distribution with extinction.

HCN emission was detected between $A_v \sim 10 - 80$ mag. The function is linear increasing representing a constant abundance in HCN throughout the core. At the central extinction peak maximum intensities of 0.9 K km s^{-1} are reached. HNC shows a very similar behavior but spanning a wider range in intensities reaching 1.2 K km s^{-1} at the extinction peak and showing less scatter. Like reported in the literature also B59 exhibits a stronger detection for HNC as for HCN although both should be formed to equal amounts and HNC being less stable (Graniner et al, 2014). With a ratio of $\frac{\mathrm{HNC}}{\mathrm{HCN}} = 1.4$ B59 lies at the lower range of values found for molecular clouds ($1 - 4.5$).

HCO^+ was observed at a detection threshold of $A_v \sim 5$ mag whereas $H^{13}CO^+$ was not detected below $A_v \sim 14$ mag. Both molecules were found to rise in intensity with increasing density but HCO^+ exhibits significantly large scatter whereas its rarer isotopologue shows a much clearer trend. The integrated intensity maps in section 4.1 show HCO^+ as being spatially more extended than $H^{13}CO^+$ which counts to the high observed scatter. Peak intensities at $A_v = 80$ mag were found to be 0.95 K km s^{-1} for HCO^+ and 0.70 K km s^{-1} for $H^{13}CO^+$.

N_2H^+ is not detected below $A_v = 26$ mag and showed the strongest emission of all high density tracers reaching values of 2.52 K km s^{-1} at the extinction peak. The function is linear rising toward greater visual depths but also scatter is increasing with extinction, spanning a range of more than 1 K km s^{-1}. Figure 4.6 in chapter 4 shows the integrated intensity map of N_2H^+ with the emission being very centrally concentrated within the innermost extinction contours. With a critical density of 1.107×10^6 cm^{-3} N_2H^+ traces the most densest regions and is therefore used to compare with the optically thin $C^{18}O$ of the low density regime. The two emission lines over-plotted show that N_2H^+ emission is arising at the same depth where $C^{18}O$ starts to decrease. Since $C^{18}O$ was proven to behave optically thin the decline in abundance can be interpreted as depletion of CO from the gas phase. With rising densities CO molecules start to freeze onto dust grains and high density tracers start to dominate gas phase chemistry. A contour plot of $C^{18}O$ and N_2H^+ overlaid on the extinction map shows $C^{18}O$ forming a shell-like structure around the extinction peak. N_2H^+ is found to peak inside the $C^{18}O$ depletion hole.

5.5 High Density Tracers in the Molecular Ring

Although the Molecular Ring shows some similarities to B59 in the comparison of investigated CO isotopologues, high density tracers are much less evolved. Except of HNC and N_2H^+ no significant detections were retrieved. Of the remaining species only HCN exhibits detectable emission at the extinction peak with maximum intensities of 0.20 K km s^{-1}. $H^{13}CN$, HCO^+ and $H^{13}CO^+$ stay below 0.10 K km s^{-1}. Anyway, HCN was treated like it was done in section 5.2 for the $C^{18}O$ component in Core 20 reducing the selection criteria to $\frac{S}{N} > 1.5$ but the results are not shown here. Although the retrieved signal strength reaches values of 0.20 K km s^{-1} the spectral noise produced a S/N ratio only slightly greater than one. Thus HCN was listed as non-detection and will be treated together with the other remaining species in section 5.5.1.

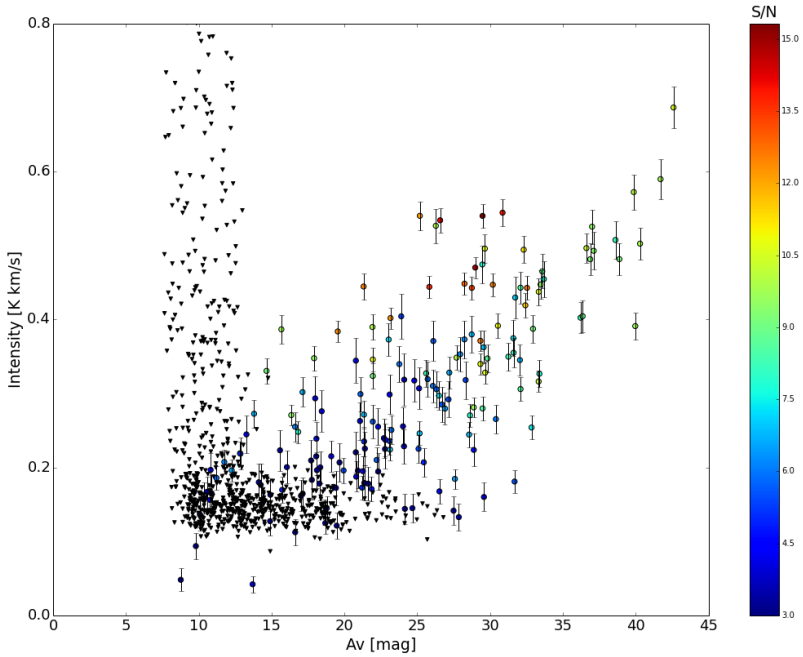

Figure 5.37: HNC emission in MR versus extinction; the color of the data points refers to their S/N value (color bar), the mean error of the fits is = 0.024 K km s^{-1}. Data points below the S/N selection criterion are presented as upper limits (black triangles).

Both HNC and N_2H^+ were found to reach maximum intensities of 0.7 K km s^{-1} at the extinction peak. Figure 5.37 shows the extinction correlated abundance profile of HNC. Following a selection criterion of $\left(\frac{S}{N} > 3\right)$ 170 spectra out of 971 observations were detected; the residual observations are shown as upper limits by three times their spectral noise. The appearance of non-detections up to extinction values of

$A_v \approx 27$ mag is due to the central constraint of the HNC emission (fig. 4.15). Spectra with $\left(\frac{S}{N} > 3\right)$ are found explicitly at the innermost extinction ranges (figure 5.38).

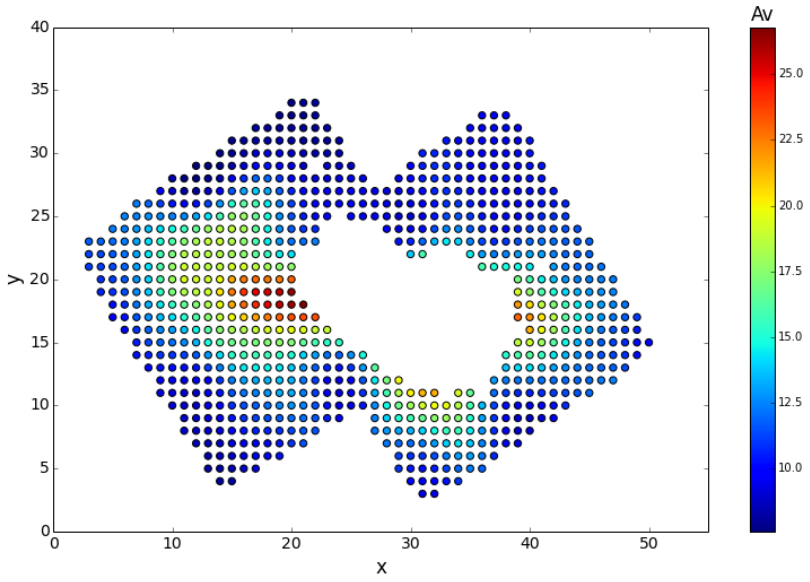

Figure 5.38: Physical image of the spatial distribution of HNC upper limits over the extinction core.

Like HNC the N_2H^+ component is found to follow a linear trend reaching maximum intensities of 0.72 K km s^{-1} at the extinction peak. Both show scatter spanning a range of 0.4 K km s^{-1}. Whereas HNC emission in B59 is comparable to that in the Molecular Ring being 0.86 K km s^{-1} at $A_v \sim 45$ mag, the difference for N_2H^+ is somewhat larger showing maximum intensities in B59 of 1.92 K km s^{-1} at $A_v \sim 45$ mag.

For N_2H^+ 841 detections were counted as upper limits. As it was the case for HNC the very central concentration of the N_2H^+ component causes upper limits appearing at higher extinction values of $A_v \approx 27$ mag.

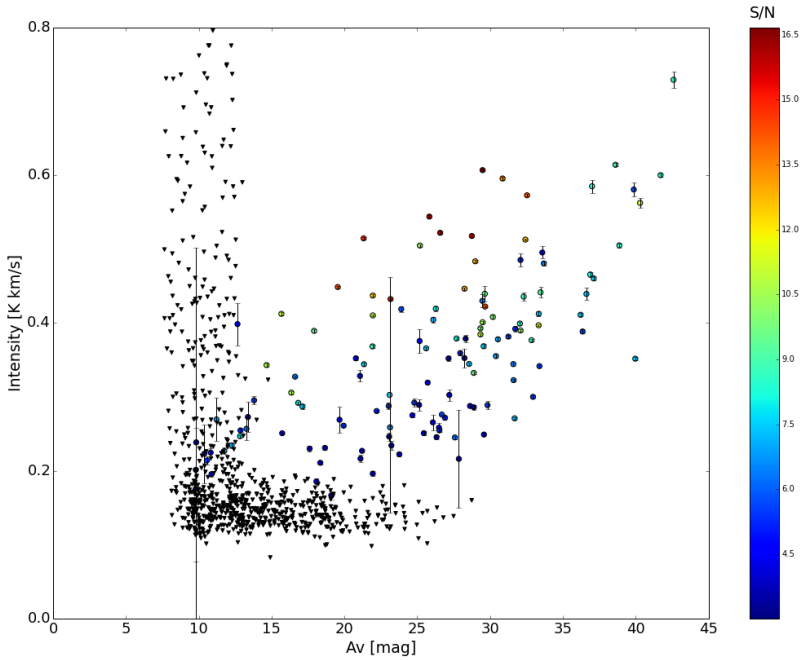

Figure 5.39: N_2H^+ emission in MR versus extinction; the color of the data points refers to their S/N value (color bar), the mean error of the fits is $= 0.0093$ K km s^{-1}. Data points below the S/N selection criterion are presented as upper limits (black triangles).

In a last test the optically thin $C^{18}O$ component is plotted together with N_2H^+ against extinction (fig. 5.40). The Molecular Ring is the only core of our sample which shows a steep rise in $C^{18}O$ abundance until $A_v \sim 20$ mag followed by a decline over 0.37 K km s^{-1} to the center. The strong scatter in the outer extinction ranges was proven to be due to temperature effects (see thereforee figure 5.24. which shows MR in physical x and y pixel coordinates color coded with excitation temperature T_{ex}). N_2H^+ is present already at $A_V \approx 10$ mag and is constantly rising toward the center. It is only in the innermost extinction ranges that N_2H^+ starts to dominate over $C^{18}O$. The difference in abundance at the peak extinction is not as great as in B59 but CO depletion may be already occurring.

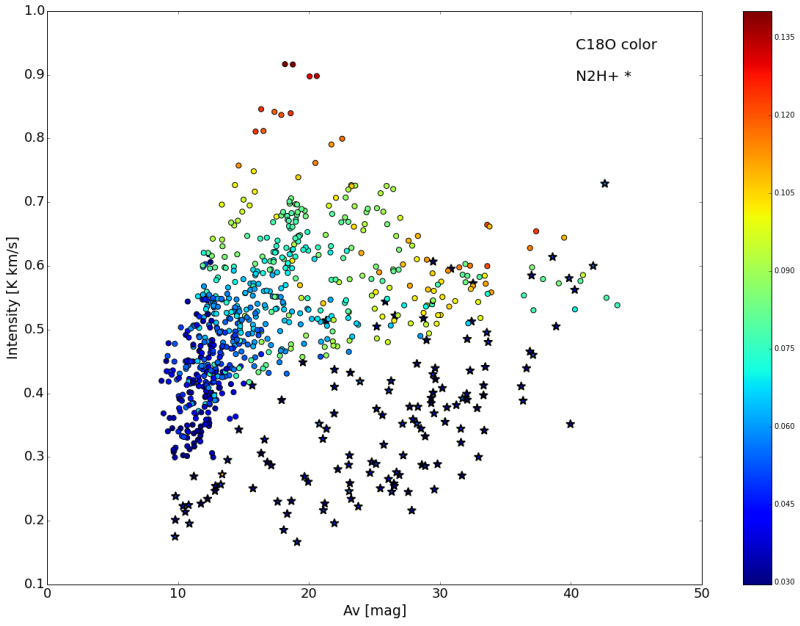

Figure 5.40: $C^{18}O$ (colored dots (T_{ex})) and N_2H^+ (black stars) in MR versus extinction

The extinction normalized plot in figure 5.41 gives an approximation of the relative abundances. We found $C^{18}O$ clearly declining in the innermost regions. Although data points in the outer cloud ranges possess large error bars it is noticeable that N_2H^+ is already present. Like in B59 the emission remains constant toward the center. If depletion effects are present in the Molekular Ring chemical differentiation is not very distinct yet and maybe just beginning.

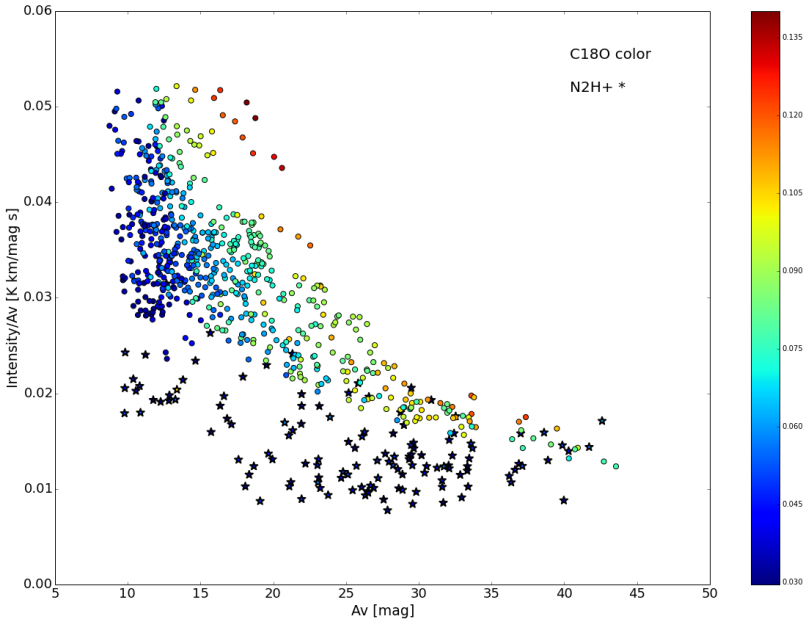

Figure 5.41: Intensity normalized with extinction; $C^{18}O$ (colored dots (T_{ex})) and N_2H^+ (black stars) in MR versus extinction

The contour map presented in figure 5.42 shows the extinction map of the Molecular Ring over-plotted with $C^{18}O$ (*black contours*) and N_2H^+ (*red contours*). $C^{18}O$ peaks afar from the extinction peak and is thinning out with greater extinctions whereas N_2H^+ emission peaks very close to the extinction core. However, there is no evolved depletion hole around the extinction center and chemical differentiation is maybe just about to develop in the innermost regions.

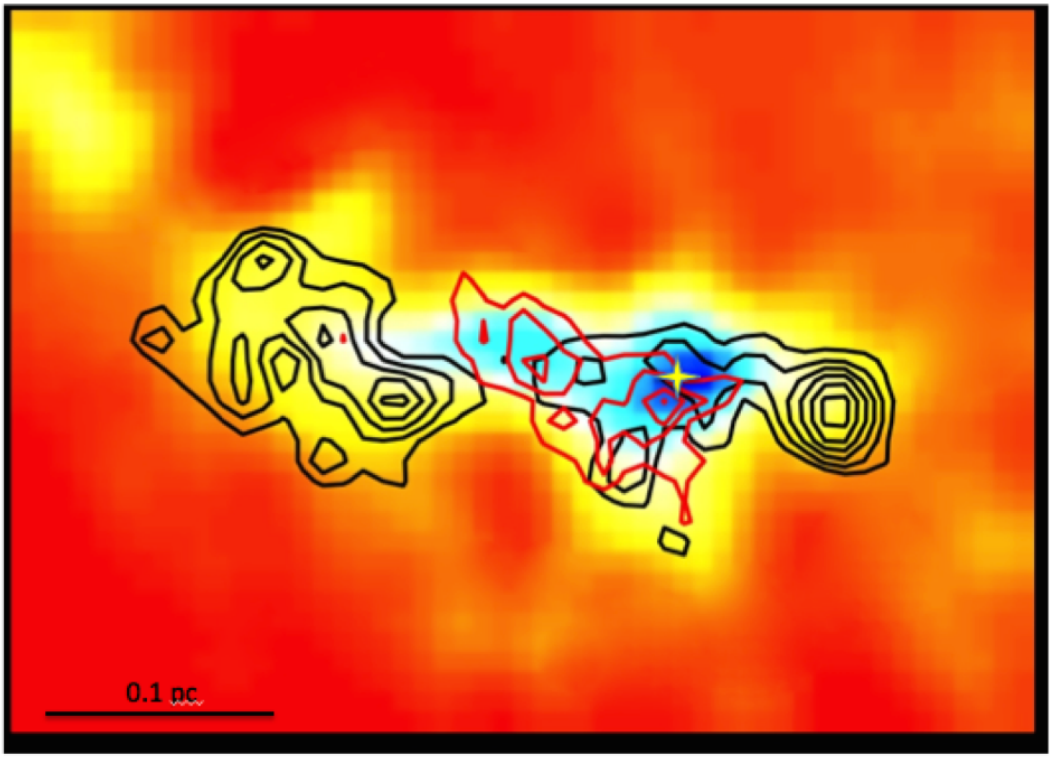

Figure 5.42: Extinction map of the B59 core over plotted with $C^{18}O$ contours (*black*) from $70-100\%$ $(100\% = 0.9\ \mathrm{K\ km\ s^{-1}})$ in steps of $+2\%$ and N_2H^+ contours (*red*) from $67-100\%$ $(100\% = 3.1\ \mathrm{K\ km\ s^{-1}})$ in steps of $+4\%$; the yellow star marks the central extinction peak.

5.5.1 Non-Detections

In the Molecular Ring four observations beside $C^{17}O$ were listed as non-detections namely HCN, $H^{13}CN$, HCO^+ and $H^{13}CO^+$. For all of them the spectra covering the extinction peak were selected and summarized to an averaged spectrum. The results are shown in figures 5.43 to 5.46. Like it was the case for the other non-detections (except of $C^{17}O$ in B59) no emission line showed up in the averaged and noise reduced spectra.

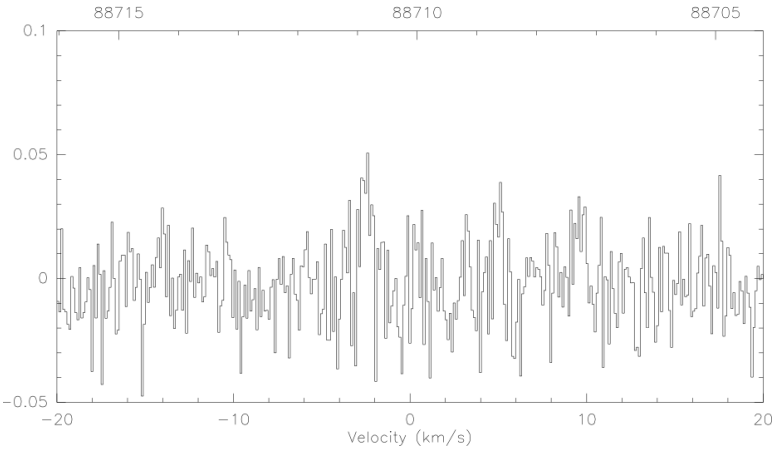

Figure 5.43: Averaged spectrum out of 15 observations in HCN covering the extinction peak of MR; spectral noise $\sigma = 0.05499$ K

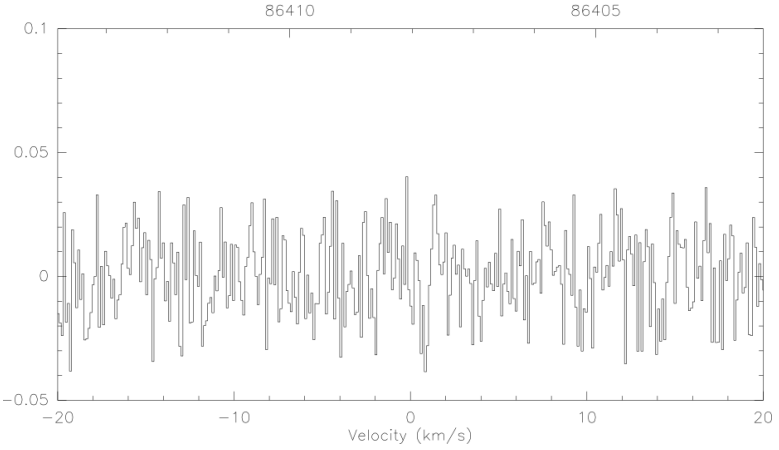

Figure 5.44: Averaged spectrum out of 15 observations in $H^{13}CN$ covering the extinction peak of MR; spectral noise $\sigma = 0.03024$ K

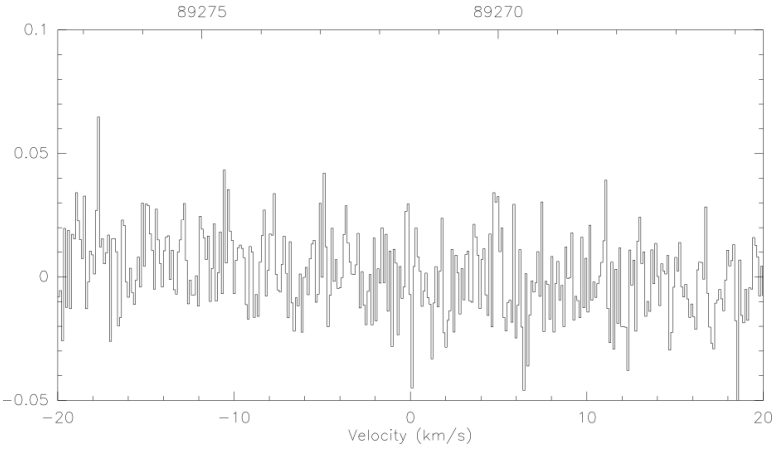

Figure 5.45: Averaged spectrum out of 15 observations in HCO^+ covering the extinction peak of MR; spectral noise $\sigma = 0.03332$ K

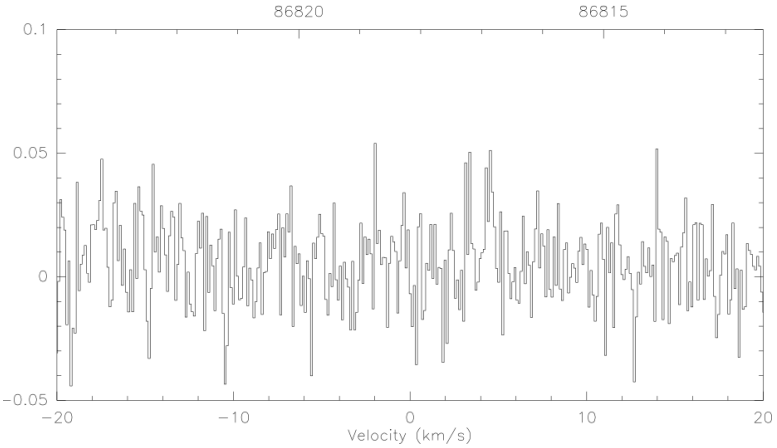

Figure 5.46: Averaged spectrum out of 15 observations in $H^{13}CO^+$ covering the extinction peak of MR; spectral noise $\sigma = 0.03827$ K

5.5.2 Summary

The Molecular Ring is found to show less diversity and chemical richness than B59. Only two out of six observed molecular transition lines in the high density regime were detected. These were HNC and N_2H^+ which display a relatively similar emission behavior. Both of them follow a linear trend reaching maximum intensities of 0.72 K km s^{-1} at the extinction peak. The difference to B59 at comparable extinction ranges is with 0.14 K km s^{-1} for HNC and 1.20 K km s^{-1} for N_2H^+ somewhat larger for N_2H^+. Furthermore both molecules possess more than 800 detections with $\left(\frac{S}{N} < 3\right)$. Due to the very central concentration of the highest S/N values upper limits also appeared at higher extinction ranges of about $A_v \approx 27$ mag. Of the remaining molecular species HCN shows the highest integrated intensities reaching 0.22 K km s^{-1} at the extinction peak. Unfortunately spectral noise was too large to allow a reasonable selection after S/N values. But nevertheless the abundance ratio of HNC and HCN was retrieved which amounts to $\frac{HNC}{HCN} = 3.5$. This was done by summarizing seven marginal detections of HCN at the extinction peak and using the peak emission of the add up spectrum. As HCN was only marginally detected the retrieved $\frac{HNC}{HCN}$ ratio should be taken as upper limit (compare to $C^{18}O$ component in Core 20, section 5.2). Therefore the Molecular Ring seems to possess a higher abundance ratio than B59 with $\frac{HNC}{HCN} = 1.4$. This could be related to the fact that B59 shows ongoing star formation. Like it is reported in Graniner et al. (2014) $\frac{HNC}{HCN}$ abundance ratios are found to decline in regions with ongoing star formation activity.

A direct comparison of N_2H^+ with $C^{18}O$ leads to the conclusion that the observed decline in $C^{18}O$ abundance is due to depletion from the gas phase. From both the extinction-correlated abundance profile and the contour maps of $C^{18}O$ and N_2H^+ it seems that depletion is not as far evolved as in B59. N_2H^+ emission is only slightly exceeding that of $C^{18}O$ and the contour map shows $C^{18}O$ is thinning out at central extinctions but not yet completely depleted.

6 Summary

In order to reveal the nature of dense extinction cores and to get possible hints on the star formation process and its conditions we investigated three molecular cores of the ~ 130 pc distant Pipe Nebula Molecular Cloud ($l = 0°$, $b = 5°$). With the 22-m radio telescope in the Australian Warrumbungle Mountains we obtained spectroscopic line measurements in the ($J = 1 \rightarrow 0$) transition of CO and its isotopologues ^{13}CO, C^{17}O, C^{18}O, as well as of the high density tracers HCN, H^{13}CN, HNC, HCO$^+$, H^{13}CO$^+$ and N_2H^+. As the homonuclear molecule H_2, of which molecular clouds mostly consist, possesses no permanent electric dipole moment, tracer molecules collisional excited by the numerous number of H_2 molecules are used to trace molecular core structure. The observed molecules differ in their critical densities such that a broad extinction range up to highest densities is covered.

Using the on-the-fly-mode of the Mopra telescope we obtained sky maps of three regions in the Pipe Nebula in each transition line. These regions were namely the star forming region B59 at the northwestern extension of the Pipe (0.18°×0.20°), a neighboring Core (C20) in the Pipe's main axes (0.16°×0.15°) and part of the Molecular Ring (0.14°×0.22°) lying in a big irregular gas accumulation at the southeastern end of the Pipe. The molecular emission maps were compared with extinction maps of the respective regions constructed by Lombardi et al. (2006) using 4.5 million background sources of the 2MASS catalogue. After adjustments concerning resolution and astrometry spectral line parameters were extracted using the standard IRAM data reduction package CLASS and compared to extinction data using the IPython programming environment.

For the three cores extinction ranges between $A_V = 2.27\ mag - 78.8$ mag (B59), $A_V = 0.2\ mag - 14.4$ mag (C20), and $A_V = 3.53\ mag - 44$ mag (Molecular Ring) were measured. Furthermore for Core 20 we obtained only measurements of CO and its isotopologues. The spectral position info was sorted into detections ($\frac{S}{N} > 3$) and non-detections ($\frac{S}{N} < 3$) and related to the extinction data. From this scatter plots were produced showing the behavior of molecular abundances with growing extinction depth. ^{12}CO and ^{13}CO in general tend to turn optically thick early and to decline toward the core's center. Only in Core 20 ^{13}CO was found to increase in intensity toward peak extinction values but was proven to be optically thick by comparing the ratios of relative line strengths to other isotopologues with the galactic values (Rohlfs & Wilson, 2004). Rarer isotopologues as C^{17}O and C^{18}O are expected to stay optically thin up to highest extinctions. If constant in abundance the emission behavior should be linear related to extinction as A_V is a measurement of dust column density. C^{17}O

was not detected in either of the cores above the $\frac{S}{N} > 3$ detection limit and listed as non-detected. However the $C^{18}O$ component has a good detection rate and it was possible to derive measurements of H_2 column density. Following Wilson et al. (2009) excitation temperatures T_{ex} were calculated using the optically thick ^{12}CO component and assumed to be the same for all CO isotopologues. From this $C^{18}O$ column density was calculated which was converted into H_2 column density by applying a correction factor of 1.7×10^{-7} corespondent to the galactic abundance ratio of H_2 and $C^{18}O$. It is possible to derive H_2 column density in an alternative way by using the measured dust extinction values and a correction factor taking the gas-to-dust ratio into account (2.0×10^{21} cm^{-2} per magnitude). Table 6.1 gives an overview of the calculated values. Deviations of the two column density measurements can be due to depletion effects which reduce CO in abundance toward the core's center whereat significant amounts of H_2 mass can be missed. Another possibility is a simple underestimation of CO column density using the method outlined in Wilson et al. (2009).

In B59 all high density tracers were detected above $\frac{S}{N} > 3$ whereas in the Molecular Ring only HNC and N_2H^+ were detected. From the remaining species spectra covering the extinction peak were summarized in order to find possible marginal detections. All high density tracers show a strong rise toward the extinction peak representative for an optically thin tracer. N_2H^+ and $C^{18}O$ were used in comparison to draw a more general picture of the core's structure connecting the low- and the high-density regime. In B59 we found evidence for the out-freezing of CO in the innermost regions accompanied by a strong rise of N_2H^+ abundance. The distribution function of $C^{18}O$ with extinction shows a linear increasing in the outer cloud ranges until a decline in abundance breaks from the linear relation between approximately $A_V \approx 20$ mag and approximately $A_V \approx 40$ mag where N_2H^+ starts to dominate. In a contour plot of $C^{18}O$ and N_2H^+ contours over plotted on the extinction map $C^{18}O$ is found to form a depletion hole around the center peaking approximately $0.5'$ apart from the extinction peak. N_2H^+ peaks inside the $C^{18}O$ depletion hole lying much closer to the extinction peak but not directly covering it.

In the Molecular Ring the effect is much less distinct and depletion seems to be just occurring. According to some authors (e.g. Alves et al., 2008) the Molecular Ring, lying in the irregular structured gas accumulation at the southwestern end of the Pipe called the *bowl*, is possibly in an earlier evolutionary stage than cores in the Pipe's main axes (*stem*) or B59, the only star forming region (SFE = 0.6%). However, Aguti et al. (2007) found strong signs of depletion in the core FeST 1-457 neighboring the part of the Molecular Ring investigated in the present study. In their paper they also made comparisons between $C^{18}O$ and N_2H^+ intensity distribution and found a strong

	B59	C20	mol. ring
$T_{ex(^{12}CO)}$	10.02 K	8.10 K	9.08 K
$N_{H_2(C^{18}O)}$	8.84×10^{21} cm^{-2}	2.78×10^{21} cm^{-2}	5.46×10^{21} cm^{-2}
$N(H_2(dust))$	3.312×10^{22} cm^{-2}	1.139×10^{22} cm^{-2}	2.865×10^{22} cm^{-2}

Table 6.1: Mean Values for derived excitation temperature and column density in B59, Core 20 and the Molecular Ring

decline in $C^{18}O$ abundance accompanied by a rise in N_2H^+ toward the center. Similar results were obtained by Bergin et al. (2002) for the dense cloud B68 which is part of the northern extensions of the Pipe (called *smoke*). Tafalla et al. (2002) studied dense cores in the Taurus Molecular Cloud (L1498, L1495, L1400K, L1517B, and L1544) and found strong evidence of CO depletion. It seems that depletion occurs very often in starless cores and may be characteristic for them. It may be a first precursor of star formation but is not indicative for it as a long stable configuration of the extinction core would naturally lead to chemical differentiation.

7 Acknowledgements

Special thanks go to Dr. Jan Forbrich who accompanied me with this master thesis and always found time for extended discussions. His kind and patient manner were the most motivating. My special thanks are also directed to Dr. Joao Alves and Dr. Alvaro Hacar who also always took their time for helpful discussions. I also thank Dr. Paula Teixera and my colleagues for their friendly help and support.

8 References

1. Aguti et al., 2007 *"The Dynamical State of the Starless Dense Core FeSt 1-457: A Pulsating Globule?"*, The Astrophysical Journal, Volume 665, Issue 1, pp. 457-465. DOI: 10.1086/519272; e-print: arXiv:0705.0330.

2. Aikawa et al., 2003 *"Molecular Evolution in Collapsing Prestellar Cores. II. The Effect of Grain-Surface Reactions"*, The Astrophysical Journal, Volume 593, Issue 2, pp. 906-924. DOI: 10.1086/376616; e-print: arXiv:astro-ph/0305054.

3. Aikawa et al., 2008 *"Molecular Evolution and Star Formation: From Prestellar Cores to Protostellar Cores"*; The Astrophysical Journal, Volume 674, Issue 2, pp. 984-996. DOI: 10.1086/524096; e-print: arXiv:0710.0712.

4. Alves et al., 2008 *"Optical polarimetry toward the Pipe nebula: revealing the importance of the magnetic field"*, Astronomy and Astrophysics, Volume 486, Issue 2, 2008, pp.L13-L16. DOI: 10.1051/0004-6361:200810091; e-print: arXiv:0806.1189.

5. Bergin et al., 2002 *"N_2H^+ and $C^{18}O$ depletion in a cold dark cloud"*, The Astrophysical Journal, Volume 570, Issue 2, pp. L101-L104. DOI: 10.1086/340950; e-print: arXiv:astro-ph/0204016.

6. Bergin & Tafalla, 2007 *"Cold Dark Clouds: The Initial Conditions for Star Formation"*, Annual Review of Astronomy & Astrophysics, vol. 45, Issue 1, pp.339-396. DOI: 10.1146/annurev.astro.45.071206.100404; e-print: arXiv:0705.3765.

7. Bolatto et al., 2013 *"The CO-to-H_2 Conversion Factor"*, Annual Review of Astronomy and Astrophysics, vol. 51, issue 1, pp. 207-268. DOI: 10.1146/annurev-astro-082812-140944; e-print: arXiv:1301.3498.

8. Caselli et al., 1999, *"CO Depletion in the Starless Cloud Core L1544"*, The Astrophysical Journal, Volume 523, Issue 2, pp. L165-L169. DOI: 10.1086/312280.

9. Cernicharo & Guelin , 1987, *"The physical and chemical state of HCL2"*, Astronomy and Astrophysics (ISSN 0004-6361), vol. 176, no. 2, April 1987, p. 299-316.

10. Downes D., 1989, *"Radio Astronomy Techniques"*, Evolution of Galaxies Astronomical Observations Lecture Notes in Physics Volume 333, 1989, pp 351-384; DOI: 10.1007/3-540-51315-9-8.

11. Dobbs, Bonnel, Pringle 2006 *"The formation of molecular clouds in spiral galaxies"*, Monthly Notices of the Royal Astronomical Society, Volume 371, Issue 4, pp. 1663-1674. DOI: 10.1111/j.1365-2966.2006.10794.x; e-print: arXiv:astro-ph/0602103.

12. Forbrich et al., 2009 *"A Spitzer Census of Star Formation Activity in the Pipe Nebula"*, The Astrophysical Journal, Volume 704, Issue 1, pp. 292-305. DOI: 10.1088/0004-637X/704/1/292; e-print:arXiv:0908.4086.

13. Frau et al. 2010 *"Young starless cores embedded in the magnetically dominated Pipe nebula"*, The Astrophysical Journal, Volume 723, Issue 2, pp. 1665-1677. DOI: 10.1088/0004-637X/723/2/1665; e-print: arXiv:1009.2082.

14. Frerking et al., 1982 *"The Relationship between Carbon Monoxide Abundance and Visual Extinction in Interstellar Clouds"*, Astrophysical Journal, Part 1, vol. 262, Nov. 15, 1982, p. 590-605. DOI: 10.1086/160451.

15. Goldsmith P. 2001 *"Molecular Depletion and Thermal Balance in Dark Cloud Cores"*, The Astrophysical Journal, Volume 557, Issue 2, pp. 736-746. DOI: 10.1086/322255.

16. Graniner et al, 2014 *"The HNC/HCN Ratio in Star-forming Regions"*, The Astrophysical Journal, Volume 787, Issue 1, article id. 74, 11. DOI: 10.1088/0004-637X/787/1/74; e-print: arXiv:1404.5338.

17. Hirota et al., 1998 *"Abundances of HCN and HNC in Dark Cloud Cores"*, The Astrophysical Journal 503: 717-728. DOI: 10.1086/306032.

18. Hotzel et al., 2002 *"$C^{18}O$ abundance in the nearby globule Barnard 68"*, Astronomy & Astrophysics 391, 275?285. DOI: 10.1051/0004-6361:20020786.

19. Onishi et al. in 1999 *"NANTEN Observations of the Pipe Nebula; A Filamentary Massive Dark Cloud with very low Star-Formation Activity"*, Publications of the Astronomical Society of Japan, v.51, p.871-881.. DOI: 10.1093/pasj/51.6.871.

20. Ostricker et. al, 2009 *"ISM Theory: Gas Phases, Turbulence, and Star Formation"*, Published online at http://ssc.spitzer.caltech.edu/mtgs/ismevol/"

21. Kontinen et al., 2000 *"Molecular line study of evolution in protostellar cloud cores"*, Astronomy and Astrophysics, v.361, p.704-718. e-print: arXiv:astro-ph/0008138.

22. Kutner & Ulich, 1981, *"Recommendations for calibration of millimeter-wavelength spectral line data"*, Astrophysical Journal, Part 1, vol. 250, Nov. 1, 1981, p. 341-348. DOI: 10.1086/159380.

23. Lada et al., 1987 *"Star Formation: From OB Association sot Protostars"*, Published in Star forming regions; Proceedings of the Symposium, Tokyo, Japan, Nov. 11-15, 1985 (A87-45601 20-90).

24. Lada et al., 1994 *"Dust extinction and molecular gas in the dark cloud IC 5146"*, The Astrophysical Journal, vol. 429, no. 2, pt. 1, p. 694-709. DOI: 10.1086/174354.

25. Ladd et al. 2005 *"Beam Size, Shape and Efficiencies for the ATNF Mopra Radio Telescope at 86?115 GHz"*, Publications of the Astronomical Society of Australia, 22: 62?72. DOI: 10.1071/AS04068.

26. Leiden atomic and molecular database *http://home.strw.leidenuniv.nl/ moldata/*

27. Loison et al., 2014 *"The interstellar gas-phase chemistry of HCN and HNC"*, Published online: eprint arXiv:1406.1696. e-print: arXiv:1406.1696

28. Lombardi et al., 2006 *"2MASS wide field extinction maps I. The Pipe Nebula"*, Astronomy & Astrophysics 454, 781?796. DOI: 10.1051/0004-6361:20042474; e-print: arXiv:astro-ph/0606670.

29. Low & Klessen, 2004 *"Control of star formation by supersonic turbulence"*, Reviews of Modern Physics, vol. 76, Issue 1, pp. 125-194. DOI: 10.1103/RevModPhys.76.125; e-print: arXiv:astro-ph/0301093.

30. Morata et al., 2003 *"Multitransitional observations of the CS core of L673"*, Astronomy and Astrophysics, v.397, p.181-189. DOI: 10.1051/0004-6361:20021103, e-print: arXiv:astro-ph/0210088.

31. Morata et al., 2005 *"Evidence for transient clumps and gas chemical evolution in the CS core of L673"*, Astronomy and Astrophysics, Volume 435, Issue 1, May III 2005, pp.113-124. DOI: 10.1051/0004-6361:20041829; e-print: arXiv:astro-ph/0412621.

32. Muench et al. 2007 *"The Nature of the Dense Core Population in the Pipe Nebula: Core and Cloud Kinematics from C18O Observations"*, The Astrophysical Journal, Volume 671, Issue 2, pp. 1820-1831. DOI: 10.1086/523265; e-print: arXiv:0709.0523

33. Rathborne et al., 2009 *"Dense Cores in The Pipe Nebula: An Improved Core Mass Function"*, The Astrophysical Journal, Volume 699, Issue 1, pp. 742-753. DOI: 10.1088/0004-637X/699/1/742; e-print: arXiv:0904.4169

34. Rohlfs et al., (2004), *"Tools of Radio Astronomy"*, Tools of radio astronomy, 4th rev. and enl. ed., by K. Rohlfs and T.L. Wilson. Berlin: Springer, 2004.

35. Ryter et al., 1996 *"Interstellar Extinction from Infrared to X-Rays: an Overview"*, Astrophysics and Space Science, Volume 236, Issue 2, pp.285-29.

36. Sarrasin et al., 2009 *"The rotational excitation of HCN and HNC by He: new insights on the HCN/HNC abundance ratio in molecular clouds"*, Monthly Notices of the Royal Astronomical Society, Volume 404, Issue 1, pp. 518-526.

37. Schilke et al., 1982 *"A study of HCN, HNC and their isotopomers in OMC-1. I - Abundances and chemistry"*, Astronomy and Astrophysics (ISSN 0004-6361), vol. 256, no. 2, p. 595-612.

38. Tafalla et al., 2002 *"Systematic Molecular Differentiation in Starless Cores"*, The Astrophysical Journal, Volume 569, Issue 2, pp. 815-835. DOI: 10.1086/339321; e-print: rXiv:astro-ph/0112487.

39. Tafalla et al., 2004 *"On the internal structure of starless cores. I. Physical conditions and the distribution of CO, CS, N2H+, and NH3 in L1498 and L1517B"*, Astronomy and Astrophysics, v.416, p.191-212. DOI: 10.1051/0004-6361:20031704

40. Vuong et al., 2003 *"Determination of the gas-to-dust ratio in nearby dense clouds using X-ray absorption measurements"*, Astronomy and Astrophysics, v.408, p.581-599. DOI: 10.1051/0004-6361:20030942; e-print: arXiv:astro-ph/0306447.

41. Wilson et al, 2009 *"Tools of Radio Astronomy"*, Tools of Radio Astronomy, by Thomas L. Wilson; Kristen Rohlfs and Susanne H¸ttemeister. ISBN 978-3-540-85121-9. Published by Springer-Verlag, Berlin, Germany, 2009. DOI: 10.1007/978-3-540-85122-6

42. Wilson & Rood, 1994 *"Abundances in the Interstellar Medium"*, Annual Review of Astronomy and Astrophysics, Volume 32, 1994, pp. 191-226. DOI: 10.1146/annurev.aa.32.090194.001203.

43. Wolfire et al. 2010 *"The Dark Molecular Gas"*, The Astrophysical Journal, Volume 716, Issue 2, pp. 1191-1207. DOI: 10.1146/annurev.aa.32.090194.001203.

9 Appendix

9.1 B59

9.1.1 karma/kvis

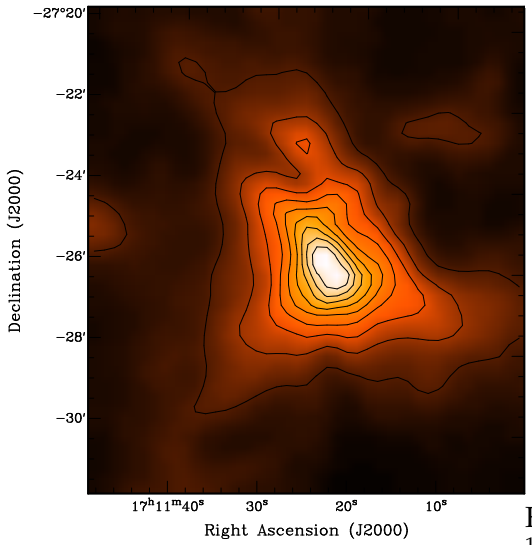

Figure 9.1: B59 extinction core; contour levels are $10-90$ % in steps of 10 % with 100 % $=80$ mag

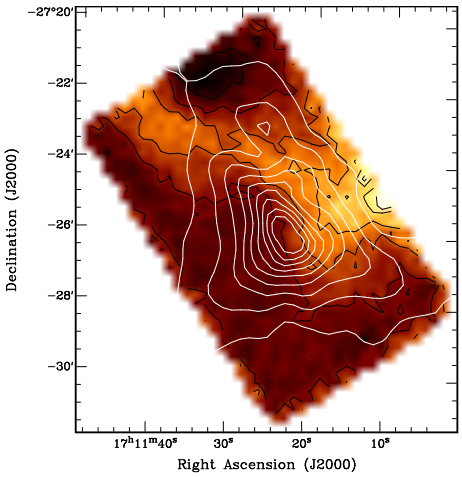

Figure 9.2: Integrated Intensity map of ^{12}CO in B59 (*black*) overlaid with extinction contours (*white*); ^{12}CO emission contours are from $10-90$ % in steps of 15 % with 100 % $=26.3$ K km s^{-1}

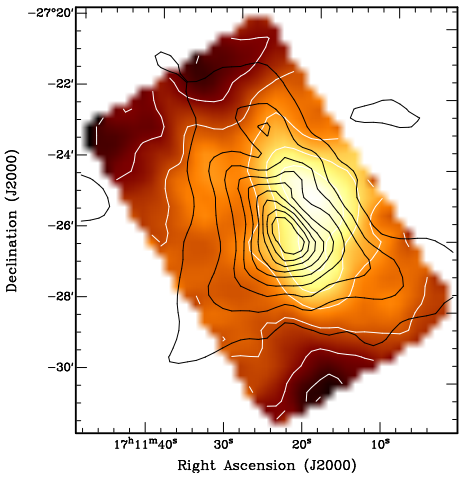

Figure 9.3: Integrated Intensity map of ^{13}CO in B59 (*whote*) overlaid with extinction contours (*black*); ^{13}CO emission contours are from $10 - 90$ % in steps of 15 % with 100 % $= 9.7$ K km s^{-1}

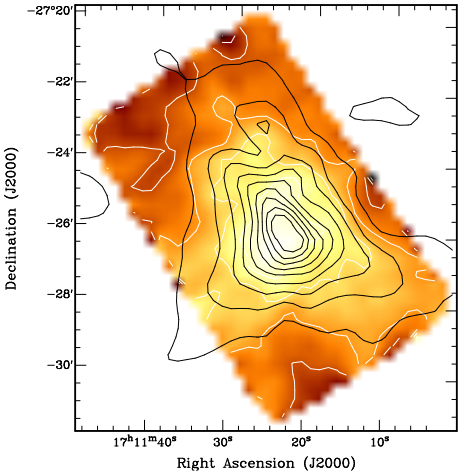

Figure 9.4: Integrated Intensity map of C^{18}O in B59 (*white*) overlaid with extinction contours (*black*); C^{18}O emission contours are from $10 - 90$ % in steps of 15 % with 100 % $= 3.25$ K km s^{-1}

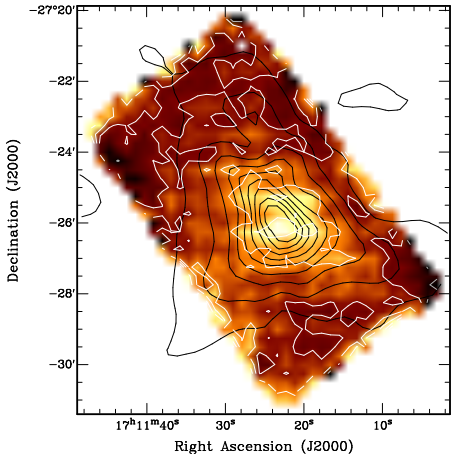

Figure 9.5: Integrated Intensity map of HCN (*white*) in B59 overlaid with extinction contours (*black*); HCN emission contours are from $10 - 90$ % in steps of 15 % with 100 % $= 2.5$ K km s^{-1}

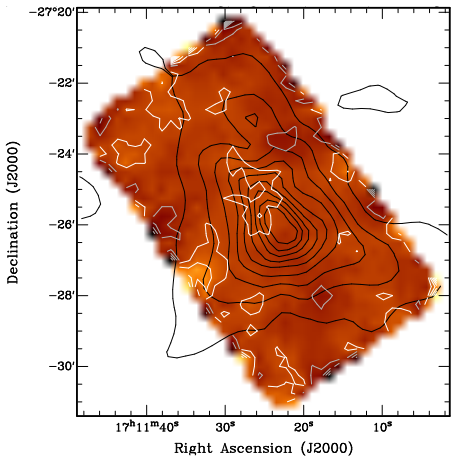

Figure 9.6: Integrated Intensity map of H^{13}CN in B59 (*white*) overlaid with extinction contours (*black*); H^{13}CN emission contours are from $10 - 90$ % in steps of 5 % with 100 % $= 3.13$ K km s^{-1}

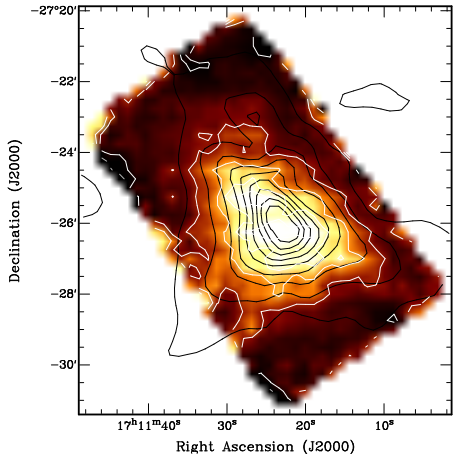

Figure 9.7: Integrated Intensity map of HNC in B59 (*white*) overlaid with extinction contours (*black*); HNC emission contours are from $10 - 90$ % in steps of 10 % with 100 % $= 1.72$ K km s^{-1}

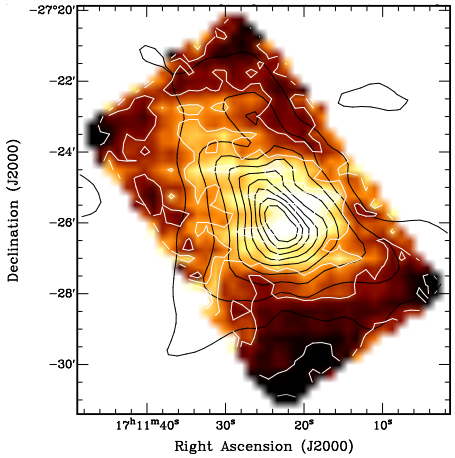

Figure 9.8: Integrated Intensity map of HCO^+ in B59 (*white*) overlaid with extinction contours (*black*); HCO^+ emission contours are from $10 - 90$ % in steps of 10 % with 100 % $= 1.19$ K km s^{-1}

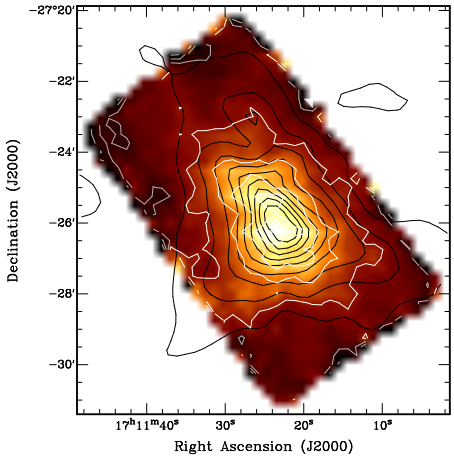

Figure 9.9: Integrated Intensity map of $H^{13}CO^+$ in B59 (*white*) overlaid with extinction contours (*black*); $H^{13}CO^+$ emission contours are from $10 - 90$ % in steps of 10 % with 100 % $= 3.13$ K km s^{-1}

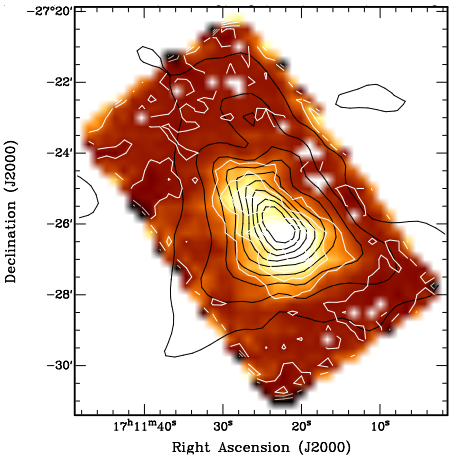

Figure 9.10: Integrated Intensity map of N_2H^+ in B59 (*white*) overlaid with extinction contours (*black*); N_2H^+ emission contours are from $10 - 90$ % in steps of 5 % with 100 % $= 2.52$ K km s^{-1}

9.2 Core 20

9.2.1 karma/kvis

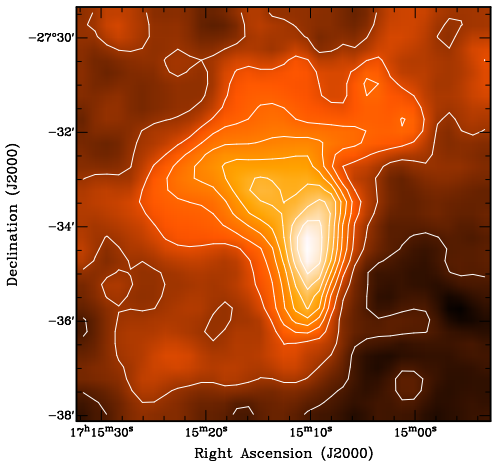

Figure 9.11: C20 extinction core; contour levels are $10 - 90$ % in steps of 10 % with 100 % = 45 mag

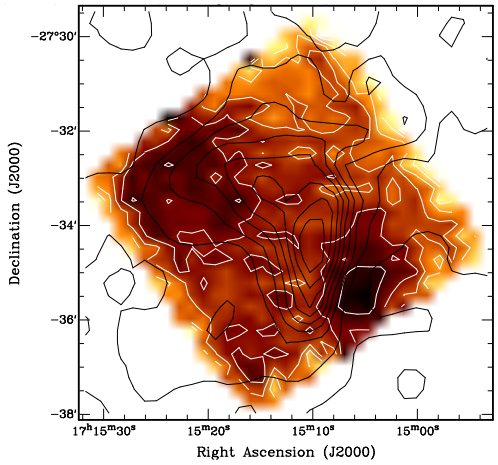

Figure 9.12: Integrated Intensity map of ^{12}CO in C20 (*white*) overlaid with extinction contours (*black*); ^{12}CO emission contours are from $10 - 90$ % in steps of 10 % with 100 % = 10.3 K km s^{-1}

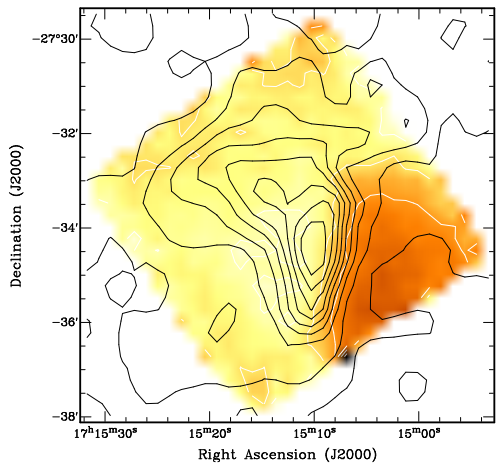

Figure 9.13: Integrated Intensity map of ^{13}CO in C20 (*white*) overlaid with extinction contours (*black*); ^{13}CO emission contours are from $10 - 90$ % in steps of 10 % with 100 % = 2.8 K km s^{-1}

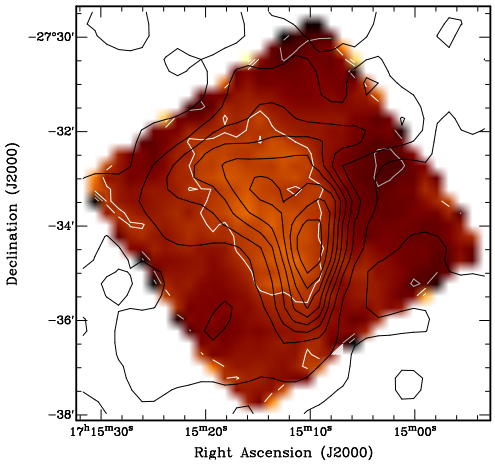

Figure 9.14: Integrated Intensity map of C^{18}O in C20 (*white*) overlaid with extinction contours (*black*); C^{18}O emission contours are from $10 - 90$ % in steps of 10 % with 100 % = 2 K km s^{-1}

9.3 Molecular Ring

9.3.1 karma/kvis

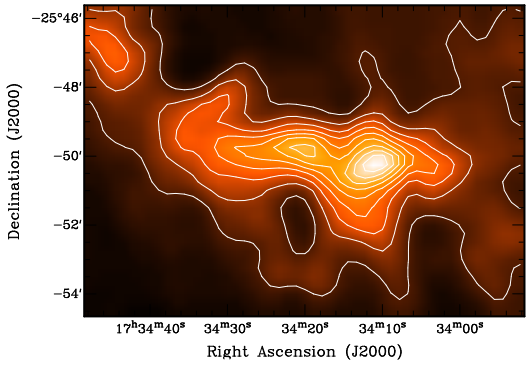

Figure 9.15: Molecular Ring extinction core; contour levels are $10 - 90$ % in steps of 10 % with $100\% = 16$ mag

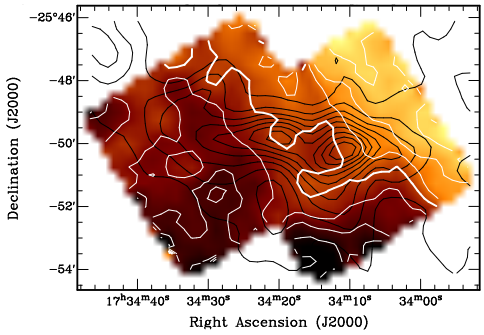

Figure 9.16: Integrated Intensity map of ^{12}CO in MR (*white*) overlaid with extinction contours (*black*); ^{12}CO emission contours are from $10 - 90$ % in steps of 10 % with $100\ \% = 25\ K$ km s

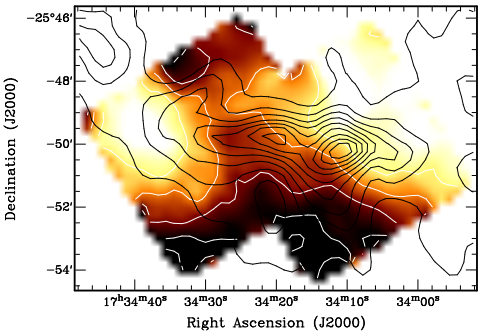

Figure 9.17: Integrated Intensity map of ^{13}CO in MR (*white*) overlaid with extinction contours (*black*); ^{13}CO emission contours are from $10 - 90$ % in steps of 15 % with 100 % $= 7.8$ K km s^{-1}

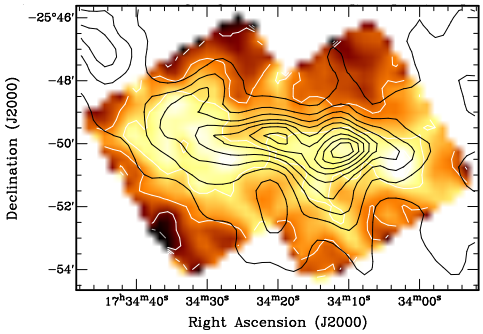

Figure 9.18: Integrated Intensity map of C^{18}O in MR (*white*) overlaid with extinction contours (*black*); C^{18}O emission contours are from $10 - 90$ % in steps of 15 % with 100 % $= 0.9$ K km s^{-1}

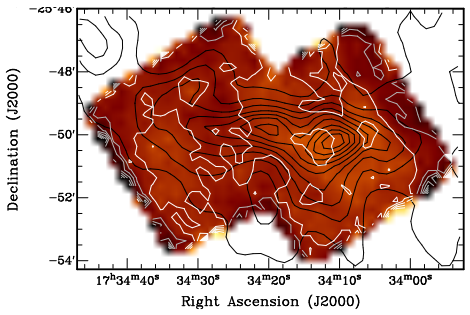

Figure 9.19: Integrated Intensity map of HCN (*white*) in MR overlaid with extinction contours (*black*); HCN emission contours are from $10 - 90$ % in steps of 15 % with 100 % $= 3.6$ K km s^{-1}

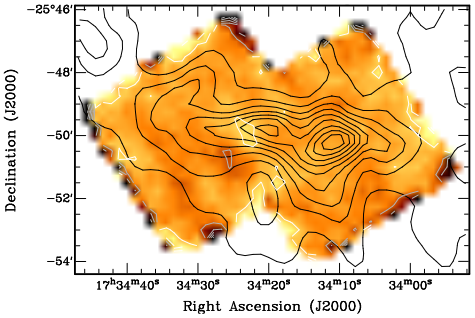

Figure 9.20: Integrated Intensity map of H^{13}CN in MR (*white*) overlaid with extinction contours (*black*); H^{13}CN emission contours are from $10 - 90$ % in steps of 10 % with 100 % $= 2.15$ K km s^{-1}

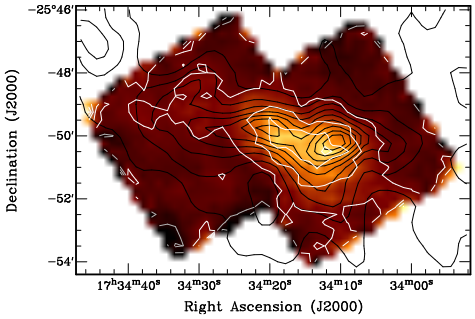

Figure 9.21: Integrated Intensity map of HNC in MR (*white*) overlaid with extinction contours (*black*); HNC emission contours are from $10 - 90$ % in steps of 10 % with 100 % $= 2.6$ K km s^{-1}

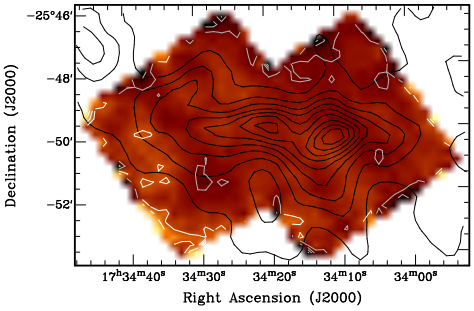

Figure 9.22: Integrated Intensity map of HCO^+ in MR (*white*) overlaid with extinction contours (*black*); HCO^+ emission contours are from $10 - 90$ % in steps of 5 % with 100 % $= 3$ K km s

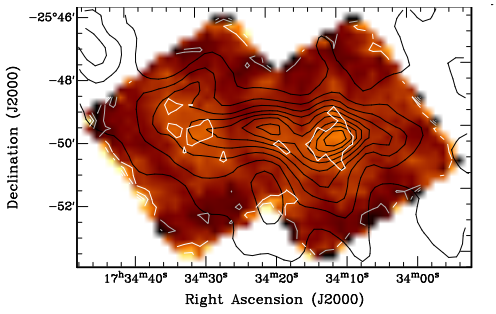

Figure 9.23: Integrated Intensity map of $H^{13}CO^+$ in MR (*white*) overlaid with extinction contours (*black*); $H^{13}CO^+$ emission contours are from $10 - 90$ % in steps of 10 % with 100 % $= 3.8$ K km s^{-1}

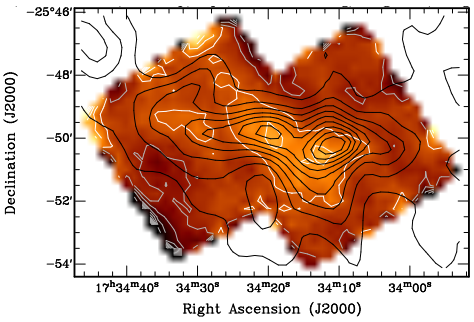

Figure 9.24: Integrated Intensity map of N_2H^+ in MR (*white*) overlaid with extinction contours (*black*); N_2H^+ emission contours are from $10 - 90$ % in steps of 5 % with 100 % $= 3.1$ K km s^{-1}

10 Abstract English

In order to investigate the physical conditions in dense molecular cores, we have studied dense cores in the Pipe Nebula in various molecular transition lines. Additionally, we have obtained near-infrared extinction maps in matching angular resolution. With its low star formation efficiency of only 0.06%, the nearby Pipe Nebula (d 130 pc) is an ideal laboratory to study the initial conditions of star formation. Here we investigate the utility of different molecular transition lines to study core structure as a function of column density, as traced by extinction mapping. For these purposes, we have used the 22-m Mopra radio telescope to map three cores (including Barnard 59) in CO(1-0) and its isotopologues ^{13}CO, C^{18}O, and C^{17}O, as well as in additional tracers with higher critical densities: HCN, H^{13}CN, HNC, HCO$^+$, H^{13}CO$^+$, and N_2H^+, all in their 1-0 transitions. We here present a detailed comparison of these transitions and the corresponding extinction maps. ^{12}CO and ^{13}CO were found to be optically thick in all cases whereas C^{18}O remains optically thin up to highest extinction values of ~ 80 mag. These lines were used to derive excitation temperatures and column densities for all three sample cores. A comparison of CO lines and high density tracers like N_2H^+ showed signs of ongoing depletion.

11 Abstract German

Der Pfeifenkopfnebel am südlichen Sternenhimmel in einer Entfernung von ~ 130 pc weist eine extrem geringe Sternentstehungseffizienz von nur 0.06% auf. Die vorliegende Studie macht sich diese Eigenschaft zunutze, um Einblick in physikalische und chemische Bedingungen vor dem Beginn der Sternentstehung zu erlangen. Zu diesem Zweck wurden Extinktionskarten unter Verwendung von 4.5 Millionen Hintergrundsternen aus 2MASS produziert, sowie spektroskopische Messungen molekularer Emissionslinien verwendet. Mit dem Mopra 22 m Radioteleskop der Australian National Telescope Facility (ANTF) wurden jeweils im ($J = 1 \rightarrow 0$) Übergang CO und seine Isotopologe ^{13}CO, C^{17}O und C^{18}O beobachtet sowie auch Moleküle höherer kritischer Dichte: HCN, H^{13}CN, HNC, HCO$^+$, H^{13}CO$^+$, N_2H^+. Die vorliegende Studie untersucht detailliert die molekularen Häufigkeitsverteilungen mit zunehmender Extinktion für drei ausgewählte Extinktionskerne. Dies waren im einzelnen das Sternentstehungsgebiet B59 an den nordöstlichen Ausläufen des Pfeifenkopfnebels sowie ein benachbarter Kern (hier deklariert als Core 20), situiert in der Hauptachse des Nebels (*stem*), und ein Teil des Molekularen Ringes, der sich in einem größeren Gebiet irregulärer Struktur am südöstlichen Ende des Nebels befindet (*bowl*). In allen Gebieten konnten wir die ^{12}CO und ^{13}CO Strahlungskomponenten als optisch dick nachweisen, während C^{18}O auch bis zu Extinktionen von ~ 78 mag optisch dünn bleibt. Diese Eigenschaften wurden zur Ermittlung von Anregungstemperatur und Säulendichte verwendet. Ein direkter Vergleich der optisch dünnen C^{18}O und N_2H^+ Komponenten mit Extinktion lässt Anzeichen für das Ausfrieren von CO auf Staubpartikel bei höheren Dichten (*depletion*) erkennen. Begleitet wird dieser Prozess von einer starken Zunahme des N_2H^+ Moleküls, das das Spektrum um den Extinktionspeak herum dominiert. Während in B59 die chemische Differenzierung deutlich ausgeprägt ist, scheinen im Molekularen Ring Depletion Effekte erst am Entstehen zu sein.

Curriculum Vitae

Elisabeth Künzl Bakk. rer. nat.

Date of Birth:	April 18^{th}, 1983
Place of Birth:	Vienna
Nationality:	Austria
E-Mail Address:	bettyk@live.at

Education and Studies

2012 - present	Academic study of Astronomy at the University of Vienna (Master of Science)
08.03.2012	Certificate of Bachelor of Science (Bakk. rer. nat.)
2008 - 2012	Academic study of Astronomy at the University of Vienna (Bakk. rer. nat.)
11.03.2008	Certificate of General University Maturity
2004 - 2008	Humboldt Matura Schule Lothringerstrasse 4, 1040 Vienna

Employment

01.03.14 - 31.07.14	Tutor at the University of Vienna

Conferences

21.05.12 - 22.05.12	Workshop on Extraterrestrial Life - Beyond our Expectations? - Workshop, hosted at the Institute of Astronomy, University of Vienna, Vienna, Austria
08.09.14 - 12.09.14	Referent at the 44th Young European Radio Astronomers Conference (YERAC) hosted by RadioNet EU, Torun, Poland

Vienna, October 21, 2014